

INFORMING DARK MATTER DETECTION
EXPERIMENTS USING COSMOLOGICAL
SIMULATIONS OF MILKY WAY-LIKE
GALAXIES

by

Robert Poole-McKenzie

A thesis submitted in partial fulfillment of the requirements of
Liverpool John Moores University
for the degree of
Doctor of Philosophy

December 2021

Declaration

The work presented in this thesis was carried out at the Astrophysics Research Institute, Liverpool John Moores University. Unless otherwise stated, it is the original work of the author.

While registered as a candidate for the degree of Doctor of Philosophy, for which submission is now made, the author has not been registered as a candidate for any other award. This thesis has not been submitted in whole, or in part, for any other degree.

Robert Poole-McKenzie
Astrophysics Research Institute
Liverpool John Moores University
ic2, Liverpool Science Park
146 Brownlow Hill
Liverpool
L3 5RF
UK

DECEMBER 2021

Abstract

Dark matter (DM) is one of the biggest mysteries in physics, a non-baryonic matter that accounts for $\sim 85\%$ of all matter in the Universe. It plays a vital role in the formation and evolution of large-scale and galactic structures, yet its nature still remains unknown. Many DM candidates have been theorised, most notably the WIMPs, however without a confirmed detection numerous questions remain. Definitive evidence for the existence of WIMPs, or of any other DM candidates, is actively sought via both direct and indirect detection experiments. This thesis explores the effect of baryons and the uncertainties associated with direct and indirect DM detection using ARTEMIS, a new suite of high-resolution cosmological hydrodynamic simulations of Milky Way-like galaxies, to aid identification of DM.

I begin by investigating the uncertainties associated with DM direct detection experiments, which aim to place constraints on the DM–nucleon scattering cross-section and the DM particle mass. These constraints depend sensitively on the assumed local DM density, the DM velocity distribution function, and several particle physics parameters. While astrophysical observations can measure the local DM density relatively accurately, the DM velocity distribution function is less well constrained. Using a sample of 42 Milky Way-mass halos from ARTEMIS, I explore the spatial and kinematical distributions of the DM in the simulated solar neighbourhoods, and study how these quantities are influenced by DM substructure, baryons, the presence of dark discs, as well as general halo-to-halo scatter (cosmic variance). I investigate also the accuracy of the Maxwellian approach for modelling velocity distribution functions in the standard halo model and find that this accuracy is hampered by significant halo-to-halo scatter in the (simulated) velocity functions. Allowing for this scatter in the computation of the

DM detection limits in the standard halo model methodology leads to a significant scatter about the exclusion limit that is typically quoted. The Maxwellian approximation works relatively well for our simulations that include the baryons, but it is less accurate for collisionless (DM-only) simulations. Given the significant halo-to-halo scatter in the quantities relevant for DM direct detection, it is recommended that this source of uncertainty is propagated through in order to derive conservative DM detection limits.

Using the ARTEMIS simulations, I then examine the prospects of indirect DM detection in the Milky Way with the upcoming Cherenkov Telescope Array (CTA) using the specific instrumental sensitivity of this facility. I investigate the baryonic effects in the γ -ray luminosities and fluxes resulted from the DM annihilation in both central halos and substructure. The unresolved substructure in the simulations is taken into account via the commonly used ‘boost’ factor. However, I find that the boost factor depends not only on the cut-off mass value but, importantly, also on the assumed c – M relation which is used to determine the concentration of the subhalos. The simulations show that the DM annihilation luminosities and fluxes of the host halos are higher for the halos containing baryons. This is due to the higher densities and concentrations of these halos as a result of adiabatic contraction in the presence of baryons, with the DM subhalos less affected. Using these results, I investigated whether a nominal 50-hour observation with CTA would be sensitive enough to detect an annihilation signal from the central Milky Way DM halo and nearby subhalos. I find that the signal from main halos via either $b\bar{b}$, $t\bar{t}$ or $\tau^+\tau^-$ channels would be detectable, at energies ~ 20 GeV – 1 TeV. For CTA to detect an annihilation signal from subhalos their individual contributions must be summed. In that case, a possible detection from substructure can be at energies $\sim 200 - 700$ GeV via the $\tau^+\tau^-$ annihilation channel. One of the largest sources of uncertainty in the differential γ -ray flux comes from the assumed c – M relation in calculating boost factors, which can lead to changes in fluxes by up to a factor of ~ 10 .

The results show that predictions for direct and indirect detection experiments need to carefully consider the associated astrophysical uncertainties. Also, the impact of baryonic physics on the DM in halos and subhalos is significant, emphasising the importance of using hydrodynamic simulations for making predictions for the detectability of DM.

Contents

Declaration	ii
Abstract	iii
List of Figures	vii
List of Tables	ix
Publications	x
Acknowledgements	xi
1 General introduction	1
1.1 The standard model of cosmology	2
1.1.1 Big Bang cosmology	2
1.1.2 Tests of Λ CDM	3
1.1.3 Dark matter	5
1.1.4 Galaxy formation	6
1.1.5 Small-scale problems	7
1.2 DM candidates and the WIMP	8
1.2.1 DM particle constraints	9
1.2.2 WIMPs	9
1.2.2.1 WIMP production	10
1.2.2.2 Supersymmetric candidates	11
1.2.3 Other candidates	11
1.2.3.1 Axions	12
1.2.3.2 Sterile neutrinos	12
1.2.3.3 MACHOs	13
1.3 Detecting dark matter	13
1.3.1 Direct detection	14
1.3.2 Indirect detection	16
1.3.3 Targets for DM detection	18
1.3.3.1 DM in the Galactic centre	18
1.3.3.2 DM in the Solar neighbourhood	19
1.3.3.3 DM in Milky Way satellite galaxies	19
1.4 Simulations	20

1.4.1	Cosmological hydrodynamic simulations	20
1.4.2	Zoom-in simulations	21
1.4.3	The ARTEMIS simulations	22
2	Informing dark matter direct detection limits with the ARTEMIS simulations	26
2.1	Introduction	26
2.2	Methods	30
2.2.1	The ARTEMIS simulations	30
2.2.1.1	Specifying simulated ‘solar neighbourhoods’	37
2.2.2	Standard Halo Model	38
2.3	Local dark matter distributions in ARTEMIS	42
2.3.1	Local density and velocity distributions	42
2.3.2	Impact of substructure	49
2.4	Larger scale changes to the DM structure	51
2.4.1	DM halo shapes	52
2.4.2	Probability of hosting a dark disc	53
2.5	Effects on DM direct detection limits	58
2.5.1	Exploring variations to the SHM	59
2.5.2	Direct detection limits using ARTEMIS	61
2.5.2.1	Experimental corrections to the calculated exclusion limits	62
2.5.2.2	Exclusion limits for the ARTEMIS halos	63
2.5.3	Empirical $f(v)$ model	66
2.6	Summary and conclusions	67
3	Modelling the prospects of detecting dark matter annihilation with CTA using the ARTEMIS simulations	70
3.1	Introduction	70
3.2	Simulations	75
3.2.1	Halo substructure	76
3.3	The γ -ray luminosity of DM annihilation	77
3.4	Annihilation fluxes and all-sky maps	84
3.5	Detectability of dark matter annihilation	91
3.6	Conclusions	98
3.7	Appendix	100
3.7.1	The γ -ray spectrum using DarkSUSY	100
4	Conclusions and future directions	102
4.1	Summary	102
4.1.1	Direct detection	103
4.1.2	Indirect detection	105
4.2	Future directions and implications	107
	Bibliography	109

List of Figures

1.1	Diagram showing DM interactions and their corresponding experimental detection techniques.	14
1.2	Composite surface brightness maps of the ARTEMIS halos at redshift $z = 0$	25
2.1	The projected density field of DM and stars in the ARTEMIS simulations for halos: G25, G28, G34 and G38	39
2.2	The local DM density, ρ_0 versus maximum circular velocity, $v_{\text{circ,max}}$, for the halos in the ARTEMIS simulations.	44
2.3	The local DM velocity distributions of the ARTEMIS simulations	45
2.4	The individual normalised local DM velocity distributions of the ARTEMIS simulations	46
2.5	The local distribution of DM velocities in cylindrical coordinates v_r , v_ϕ and v_z for halo G38	48
2.6	The local DM velocity distributions of halo G2	50
2.7	The local distribution of DM velocities in cylindrical coordinates v_r , v_ϕ and v_z for halo G2	52
2.8	Distribution of sphericity, S , of all Milky Way-mass halos in the ARTEMIS simulations, within 30 kpc of the galactic centre.	53
2.9	The azimuthal velocity DM distribution for halo G11 and all halos reduced chi-squared values for Gaussian fits	54
2.10	The local distribution of rotational velocities for the G38 halo and the projected DM density contours.	56
2.11	Histograms of the peak azimuthal velocity DM distribution for the ARTEMIS halos and the peak azimuthal velocity versus triaxiality within 30 kpc.	59
2.12	The 90% confidence level limits for a single halo with a Maxwellian distribution of local DM velocities, assuming SHM and varying ρ_0 , v_0 and v_{esc} independently.	60
2.13	The 90% confidence level limits for LZ and XENON1T parameters produced using our code.	62
2.14	The 90% confidence level limits using the ARTEMIS halos using XENON1T parameters using the SHM.	64
2.15	The 90% confidence level limits using the ARTEMIS halos using XENON1T parameters using our empirical model.	66
3.1	The median cumulative subhalo mass functions for the simulated subhalos	78
3.2	The annihilation luminosity boost factor due to substructure	81

3.3	Dark matter annihilation luminosity as a function of subhalo mass	84
3.4	All-sky maps for galaxy ‘G9’ of the annihilation flux per solid angle . . .	87
3.5	Dark matter annihilation flux as a function of subhalo mass	88
3.6	Subhalo mass as a function of distance to the observer, coloured by annihilation flux	89
3.7	Differential γ -ray flux sensitivity ($\times E^2$) for WIMPs of mass $m_\chi =$ 1 TeV, annihilating with $\langle\sigma v\rangle = 3 \times 10^{-26} \text{ cm}^3 \text{ s}^{-1}$ into various channels	95
3.8	Differential γ -ray flux sensitivity ($\times E^2$) for WIMPs of varying mass m_χ , annihilating with $\langle\sigma v\rangle = 3 \times 10^{-26} \text{ cm}^3 \text{ s}^{-1}$ into the $b\bar{b}$ channel . .	97
3.9	The γ -ray spectrum dN_γ/dE for varying WIMP masses and for differ- ent annihilation channels	101

List of Tables

2.1	The main properties of the Milky Way-analog halos in the ARTEMIS simulations	35
2.2	The goodness of fit values of the Maxwellian velocity distributions for the ARTEMIS halos.	46

Publications

In the course of completing the work presented in this thesis, the following papers have been submitted for publication in a refereed journal:

- *Informing dark matter direct detection limits with the ARTEMIS simulations.*
Robert Poole-McKenzie, Andreea S Font, Billy Boxer, Ian G McCarthy, Sergey Burdin, Sam G Stafford and Shaun T Brown, *Journal of Cosmology and Astroparticle Physics* 2020 (11), 2020, 016.
- *Modelling the prospects of detecting dark matter annihilation with CTA using the ARTEMIS simulations*
Robert Poole-McKenzie, Andreea S Font and Ian G McCarthy, *in prep.*
- *The ARTEMIS simulations: stellar haloes of Milky Way-mass galaxies.*
Andreea S Font, Ian G McCarthy, **Robert Poole-McKenzie**, Sam G Stafford, Shaun T Brown, Joop Schaye, Robert A Crain, Tom Theuns and Matthieu Schaller, *Monthly Notices of the Royal Astronomical Society* 498 (2), 2020, 1765-1785.
- *Exploring extensions to the standard cosmological model and the impact of baryons on small scales.*
Sam G Stafford, Shaun T Brown, Ian G McCarthy, Andreea S Font, Andrew Robertson and **Robert Poole-McKenzie**, *Monthly Notices of the Royal Astronomical Society* 497 (3), 2020, 3809-3829.

Acknowledgements

I would like to begin by thanking my supervisor, Andreea Font. I am truly grateful for the guidance, support and expertise you have provided over the last four years. In particular, I want to thank you for your patience; explaining and answering many of my questions and queries on various concepts. I must also thank my second supervisor, Ian McCarthy. Your scientific wisdom, constructive criticism, and ability to approach problems from a different viewpoint were invaluable to the completion of this work.

I am also thankful to everyone at the ARI, the staff, post-docs, and students, all of which make it a welcoming and enjoyable place to work. A thank you must be given to my fellow Ph.D. students, past and present, many of you I am proud to call my friends. A special thank you to Alex, Charlotte, Meghan, Joe, Mike, Sam, Shaun, Simon, and Alberto for making these last few years such an entertaining and amusing experience. I have endless fond memories of the regular tea breaks, football sessions, pay-day lunches, pub trips, and general office chatter, all of which have provided me with immense joy and laughter. I must also thank everyone involved with LIV.DAT CDT. The training and guidance provided have aided with this work, and the many skills I have gained will undoubtedly find use in my future career.

On a personal note, I must thank my family and friends, to whom I owe everything. Mum, thank you for your unconditional and constant support, even if you don't have clue what I do. Ed and Lisa, thank you for always being there when needed. Finally, Juliette. I would never have made it this far without you. You have made the seemingly impossible, possible. Your love, encouragement, and reassurance are immeasurable, I will forever be thankful.

“However difficult life may seem, there is always something you can do and succeed at.”

- Stephen Hawking

“Our planet, the Earth, is, as far as we know, unique in the universe. It contains life.”

- David Attenborough

Chapter 1

General introduction

One of the biggest mysteries in physics today is Dark Matter (DM), a non-baryonic matter that accounts for $\sim 85\%$ of all matter in our Universe. Understanding the origin, evolution and nature of DM is crucial for both particle physics and astrophysics alike. The discovery of a new type of particle could open the doors to a new era of physics and change our current understanding of the Standard Model (SM) or Supersymmetry. In addition, DM plays a dominant role in galaxy formation; pinning down the nature of this elusive component will improve our understanding of the formation and evolution of galaxies, in particular that of the Milky Way. Although DM has yet to be detected, there is a wealth of evidence pointing to the necessity of its existence, with a Nobel prize awaiting its discovery.

This chapter aims to provide the scientific background for the work presented in this thesis. Section 1.1 presents a brief outline of the standard model of cosmology. Section 1.2 outlines the constraints placed on DM particles and explores several plausible candidates, specifically focusing on the Weakly Interacting Massive Particles (WIMPs). Section 1.3 examines how DM could be detected, both directly and indirectly, and where best to search for the possible detections inside the Milky Way. Finally, Section 1.4 reviews the history and advancements of cosmological simulations, and introduces the ARTEMIS suite of simulations used in this work.

1.1 The standard model of cosmology

A combination of theoretical developments and precise observations over the last century has allowed cosmologists to extensively describe our Universe and its evolution on very large scales. Specifically, observations of the current large-scale structure distribution of our Universe support a well-defined cosmological model, known as "Lambda Cold Dark Matter" (Λ CDM). The Λ CDM model is a solution to general relativity for an isotropic, homogeneous Universe, accurately describing the formation and evolution of our Universe over the past 13.7 billion years, from the epoch of inflation to the present day (Hinshaw et al., 2013; Planck Collaboration et al., 2020). Although this model is incredibly successful, the nature of its two main components, the cold dark matter (CDM) and cosmological constant Λ , remain unknown.

1.1.1 Big Bang cosmology

The development of the Λ CDM model started in the 1930s, evidence from observations showed that galaxies appeared to be travelling away from us at velocities proportional to their distance. The recession of the galaxies can be explained by general relativity, using models from Friedmann-Lemaître-Robertson-Walker describing an expanding Universe given by a space-time metric of the form,

$$ds^2 = c^2 dt^2 - a(t)^2 \left(\frac{dr^2}{1 - kr^2} + r^2 d\Omega^2 \right), \quad (1.1)$$

the first term on the right-hand side represents the temporal evolution, where $a(t)$ is the time-dependent scale factor of the Universe (normalised to $a(t_0) = 1$ today). The second term represents the spatial evolution, where k is the curvature of the Universe (for a spatially flat Universe, $k = 0$). The constant of proportionality between the recession velocity and distance, at present ($t = 0$), is denoted using the Hubble constant,

$$H_0 \equiv H(t = 0) \equiv \frac{\dot{a}(t = 0)}{a(t = 0)}. \quad (1.2)$$

Recent measurements from cosmological data show that $H_0 \approx 70 \text{ km s}^{-1} \text{ Mpc}$ (Hinshaw et al., 2013; Planck Collaboration et al., 2020).

The expansion of the Universe leads to the conclusion that at very early times, it was denser and hotter than the present day. The very early Universe, when $a(t) < 1/1000$ of its current value, consisted of a plasma of protons, electrons and photons, continuously cooling as the Universe expanded. At a redshift $z \equiv 1/a(t) - 1 \approx 1100$, the Universe became transparent, with photons able to radiate through space carrying the signatures of this primitive state. The measurements of this radiation lead to the accidental discovery of the Cosmic Microwave Background (CMB) by Penzias & Wilson (1965), offering a window into the early Universe, and in effect, confirming the Big Bang theory as the foundation of the cosmological model.

In recent years cosmologists have been able to describe our Universe with greater precision. Using the Friedmann equations, the contents of the Universe can be related to scale factor,

$$\frac{H^2(t)}{H_0^2} = \Omega_r a(t)^{-4} + \Omega_m a(t)^{-3} + \Omega_k a(t)^{-3} + \Omega_\Lambda a(t) \quad (1.3)$$

where Ω_r , Ω_m , Ω_k and Ω_Λ are the present-day density of radiation, matter, curvature and cosmological constant respectively. The most dominant contribution Ω_Λ is a form of energy called dark energy.

1.1.2 Tests of Λ CDM

The "starting point for cosmology as a precision science" commenced with the Cosmic Background Explorer (COBE) satellite mission (Smoot et al., 1992), providing measurements of the large-scale temperature fluctuations of the CMB. These small, anisotropic temperature fluctuations resulted in the growth of structure due to gravitational instability. Valuable information about the very early Universe can be obtained by measuring the acoustic peaks of the angular power spectrum of the temperature fluctuations, which correspond to the oscillations in the matter-radiation fluid at the epoch

of recombination. Measurements of the position of the first peak (De Bernardis et al., 2000; Hanany et al., 2000; Hinshaw et al., 2013; Planck Collaboration et al., 2020) confirm that on large scales, the Universe is spatially flat ($k = 0$). The amplitude of the second acoustic peak, when compared to the first peak, constrains the baryonic density at recombination, and the following peaks provide information about the abundance of DM in the Universe. Overall, the results show that our Universe is comprised of $\sim 5\%$ baryonic matter (Ω_b); $\sim 27\%$ DM (Ω_{DM}); $\sim 68\%$ dark energy (Ω_Λ) (Riess et al., 1998; Perlmutter et al., 2002; Planck Collaboration et al., 2020).

Dark energy is the dominant component of the Λ CDM model with evidence supporting its existence first validated using low redshift measurements of Type Ia supernovae (SNe) as standard candles. SNe are ideal standard candles as their intrinsic luminosity is easily determined by measuring the evolution of their light curve. Measurements of Type Ia SNe revealed that our Universe is currently experiencing a state of accelerated expansion (Riess et al., 1998; Perlmutter et al., 2002), consolidating dark energy as a major component of Λ CDM.

An additional test of the Λ CDM model comes from the evolution of Baryonic Acoustic Oscillations (BAO) between the era of recombination and the present time. Predicted in the 1970's (Peebles & Yu, 1970; Sunyaev & Zeldovich, 1970), detected and measured in numerous galaxy surveys (Eisenstein et al., 2005; Cole et al., 2005; Padmanabhan et al., 2007; Percival et al., 2007; Ross et al., 2015; De Sainte Agathe et al., 2019), BAO support the theory of a matter-photon plasma filling the Universe before recombination, in addition to confirming the late time acceleration indicated from CMB and SNe data.

The Λ CDM paradigm continues to be tested on increasingly smaller scales by a large range of cosmological probes, such as cluster counts, strong and weak gravitational lensing, BAO, CMB and SNe (see Weinberg et al. 2013 for a review). These probes are independently improving the constraints on the Λ CDM model parameters, and hence it currently remains the accepted standard model of cosmology.

1.1.3 Dark matter

DM is the most dominant matter component in the Λ CDM model and is considered the most plausible explanation for various galactic and cosmological scale observations.

The first proposed claim of the existence of DM was made in the early 20th century, with observations of the Coma Cluster ([Zwicky, 1933](#)). The analysis of the gravitational orbits of the thousands of galaxies in the cluster led to the conclusion that the cluster should contain a large quantity of non-luminous matter. [Zwicky \(1933\)](#) referred to this missing mass as "dunkle Materie" (dark matter), assuming it was a non-shining form of ordinary matter.

The evidence for DM is strong, with the most compelling coming from the flattening of galaxy rotation curves. The flattening was first noticed by [Babcock \(1939\)](#), who discovered that the outer disc of M31 (Andromeda galaxy) was moving at surprisingly high velocities. Several decades later, spectroscopic ($H\alpha$) observations in HII regions of M31 confirmed these excess radial velocities ([Rubin & Ford, 1970](#); [Roberts & Whitehurst, 1975](#)). In contradiction with expectations of visible matter, these observations showed that the stellar velocities at the edge of the galactic disc remain constant as the distance from the centre of the galaxy increased. This evidence was later strengthened with observations of the 21 cm line in spiral galaxies ([Rubin et al., 1980](#)). Using a sample of 1100 optical and radio rotation curves from spiral galaxies [Persic et al. \(1996\)](#) confirmed that the distribution of luminous matter is significantly outweighed by DM, more so in low luminosity systems.

One of the most vital indicators of the existence of DM comes from the merging of galaxies or clusters of galaxies. The best example of such an event is the "Bullet cluster" (also known as 1E0657-558) ([Clowe et al., 2006](#)). The cluster's recent collisions have resulted in the spatial distribution of galaxies and stars to be separated from the majority of its baryonic mass, which is in the form of hot X-ray emitting gas. Comparisons of X-ray observations and weak lensing show that the mass in the Bullet cluster does not correspond with its baryonic distribution, proving that there must be another source of gravitational potential dominating the system, such as DM.

The presence of DM is also supported by evidence from gravitational lensing data. Gravitational lensing is the bending of light due to a strong gravitational field from a very dense or massive object, like the centre of a galaxy or a galaxy cluster. Strong lensing occurs when light rays deflect around an object, which leads to a distorted image of the light source. The shape and the size of these distortions can be used to measure the distribution of mass of the object and is compared against the objects visible mass.

Finally, studies of the CMB radiation play an essential role in determining the abundance of DM in the Universe, as discussed above in Section 1.1.2. The most recent values for DM density, $\Omega_{\text{DM}}h^2 = 0.1142$ and $\Omega_{\text{DM}}h^2 = 0.120$, come from the Wilkinson Microwave Anisotropy Probe (WMAP) (Hinshaw et al., 2013) and the Planck Collaboration (Planck Collaboration et al., 2020), respectively.

1.1.4 Galaxy formation

The Λ CDM paradigm is the main foundation that the theories of galaxy formation and evolution are built upon, of which the hierarchical model describes the bottom-up formation of galaxies. The galaxies we see in the Universe today are the products of small-scale fluctuations in the matter density of the very early Universe, seen as peaks in the random density field of DM. After a rapid period of inflation, these ‘seed’ fluctuations collapse under their own gravitational potential, creating over-dense DM regions, in comparison to the expanding under-dense background. The seminal work by Press & Schechter (1974) was able to describe the distribution of the DM halos masses in the early Universe, which was later improved upon by Tinker et al. (2008). As the density fluctuations continue to grow with infalling DM, the baryonic matter begins to cool and collapse into the over-densities, forming the filamentary structure known as the ‘cosmic web’ (Bond et al., 1996; Van de Weygaert & Bond, 2008). Eventually, gas collapses into the potential wells of the DM, forming galaxies, such as the Milky Way.

1.1.5 Small-scale problems

As discussed in Section 1.1, Λ CDM is an extremely successful cosmological model. However, there remains several weaknesses on small-scales (see [Bullock & Boylan-Kolchin 2017](#) for a review), of which many solutions have been theorised. Firstly, the "missing satellites problem" ([Kauffmann et al., 1993](#); [Klypin et al., 1999](#); [Moore et al., 1999](#)) comes from the discrepancy between the number of satellite galaxies predicted by N-body simulations and those observed around the Milky Way. We expect thousands of subhalos massive enough to host dwarf galaxies, however there are ~ 50 satellite galaxies within 300 kpc of the Milky Way ([Drlica-Wagner et al., 2015](#)). Secondly, the "too-big-to-fail problem" ([Boylan-Kolchin et al., 2011, 2012](#); [Garrison-Kimmel et al., 2014](#)) states that the local universe contains too few galaxies situated in intermediate-mass $\sim 10^{10}M_{\odot}$ halos. Halos of this mass are believed to have been too massive not to have formed stars, therefore it is hard to understand why they are missing. An additional challenge is the "core-cusp problem" ([McGaugh et al., 2001](#); [Gilmore et al., 2007](#); [Kuzio de Naray et al., 2008](#)), dealing with a discrepancy between the flat density profiles observed in many DM-dominated low-mass galaxies, and the cuspy density profiles predicted from Λ CDM cosmological N-body simulations, e.g. the Navarro-Frenk-White (NFW) profile ([Navarro et al., 1997](#)).

Many alternatives and extensions to Λ CDM have been proposed in order to address some of these small-scale issues, particularly changes to the nature of DM. For example, one can remove the condition that DM is collisionless and instead assume it can interact with itself. This proposed self-interacting dark matter (SIDM) has been modelled using cosmological simulations and has been shown it may solve the too-big-to-fail problem ([Zavala et al., 2013](#); [Elbert et al., 2015](#)) and the core-cusp problem ([Spergel & Steinhardt, 2000](#); [Yoshida et al., 2000](#); [Davé et al., 2001](#); [Colín et al., 2002](#); [Vogelsberger et al., 2012](#); [Rocha et al., 2013](#); [Elbert et al., 2015](#); [Kaplinghat et al., 2016](#)). One of the most favoured extensions to the Λ CDM model is warm dark matter (WDM), which is defined assuming collisionless DM with non-negligible free-streaming effects. WDM erases density perturbations on small-scales suppressing structures with masses close to the cut-off scale in the matter power spectrum, possibly resolving the missing satellite

problem (Colín et al., 2000; Bode et al., 2001; Polisensky & Ricotti, 2011; Lovell et al., 2012; Anderhalden et al., 2013; Bozek et al., 2016; Horiuchi et al., 2016; Bose et al., 2017). Additionally, WDM predicts that halos have later formation times than CDM, leading to lower central densities, which helps to alleviate the too-big-to-fail problem (Lovell et al., 2012; Horiuchi et al., 2016; Lovell et al., 2017). Studies have also shown that DM halos in a WDM scenario can have cored density profiles, however with current constraints on the mass of the DM particle, they are unable to solve the core-cusp problem (Villaescusa-Navarro & Dalal, 2011; Macciò et al., 2012; Shao et al., 2013).

In addition to changing the nature of DM, another promising way of solving some of the small-scale problems is to change some of the physical processes used in hydrodynamical simulations. Several of the most advanced hydrodynamic simulations have shown that it is possible for baryonic feedback to reduce or erase the central cusps in DM density profiles, producing core-like density profiles (Mashchenko et al., 2008; Pontzen & Governato, 2012; Madau et al., 2014; Oñorbe et al., 2015; Read et al., 2016), solving the core-cusp problem. Many hydrodynamic simulations have found that environmental influences are often invoked to help solve the too-big-to-fail problem. Interactions between the Milky Way-like galaxies and their satellites, via mechanisms such as ram pressure stripping, tidal stripping and disk shocking, can reduce the central mass of satellite galaxies by acting as additional forms of feedback (Zolotov et al., 2012; Arraki et al., 2014; Brooks & Zolotov, 2014; Brook & Di Cintio, 2015; Wetzel et al., 2016; Tomozeiu et al., 2016; Sawala et al., 2016; Dutton et al., 2016).

These small-scale problems encountered in the Λ CDM model can all be solved with plausible and well-understood solutions whilst retaining the fundamentals of the model. For these reasons Λ CDM remains the leading model for cosmology.

1.2 DM candidates and the WIMP

As we have seen in the previous section, the observational evidence for DM is overwhelming, leading to the question: what is DM made up of? This section will describe

the DM particle constraints and explore some of the DM candidates discussed in the literature.

1.2.1 DM particle constraints

For a DM particle to be considered as a plausible candidate it must first satisfy several astrophysical constraints:

- The observed abundance of CDM must match the appropriate DM relic abundance and density.
- The DM particles must be non-baryonic, in order to preserve big bang nucleosynthesis.
- The DM should be electromagnetically neutral, due to unsuccessful searches for stable charged particles ([McDermott et al., 2011](#); [Sánchez-Salcedo et al., 2010](#)), in addition to null direct detection results (see Section [1.3.1](#)).
- DM particles should have weak self-interactions due to the limits imposed from the cluster collisions, such as the Bullet Cluster.
- The DM particles should be dynamically cold to account for the small-scale density fluctuations, as seen in weak lensing observations.

No known particle satisfies all of these conditions. For a particle to meet these conditions requires an extension of the SM, of which many candidates have been theorised.

1.2.2 WIMPs

In general, the most favoured DM particle candidates that satisfy the above constraints are referred to as WIMPs (Weakly Interacting Massive Particles). Below we discuss how WIMPs satisfy several of these constraints and possible WIMP particle candidates (see [Arcadi et al. 2018](#) for a review).

1.2.2.1 WIMP production

The generation of the WIMP DM relic abundance is achieved by the freeze-out mechanism. Very early in the hot and dense Universe, DM and SM particles were in thermal equilibrium due to the DM particle production from annihilations. As the Universe evolved, expanding and cooling, the WIMPs and thermal plasma froze out of equilibrium. The decoupling of the WIMPs and thermal plasma occurred when the WIMP annihilation rate became approximately less than the Universe expansion rate $\Gamma_{\text{ann}} \lesssim H \sim T_f^2/\bar{M}_P$, where \bar{M}_P is the reduced Plank mass and T_f is the freeze-out temperature. The WIMP yield after freeze-out remained roughly constant, $Y_\chi = n_\chi/s$, where $s \sim T^3$ is the entropy density and n_χ is the number density of DM particles (χ denotes the generic WIMP).

Using the DM annihilation rate, $\Gamma_{\text{ann}} = n_\chi \langle \sigma_{\text{ann}} v \rangle$, the value for the relic abundance today in terms of the thermally averaged product of annihilation cross-section σ_{ann} and the Møller velocity, $v_{\text{Møl}} = \sqrt{(\vec{v}_1 - \vec{v}_2)^2 - (\vec{v}_1 \times \vec{v}_2)^2}$, at freeze-out is,

$$\Omega_\chi h^2 \simeq \frac{m_\chi n_\chi(T_0)}{\rho_c} h^2 = \frac{T_0^3}{\rho_c} \frac{x_f}{\bar{M}_P} \frac{1}{\langle \sigma_{\text{ann}} v_{\text{Møl}} \rangle_f} h^2 \quad (1.4)$$

where $\rho_c \approx 8 \times 10^{-47} \text{ h}^2 \text{ GeV}^4$ (Patrignani et al., 2016) is the critical energy density, $T_0 \approx 2.35 \times 10^{-13} \text{ GeV}$ (Patrignani et al., 2016) is the present temperature of the Universe, $x = m_\chi/T = 25$ (Nihei et al., 2001) and $\vec{v}_{1,2}$ are the annihilating DM particles velocities.

Finally, using $\Omega_\chi h^2 \approx 0.12$ and Eq.1.4,

$$\langle \sigma_{\text{ann}} v \rangle_f \approx 3 \times 10^{-26} \text{ cm}^3 \text{ s}^{-1} \quad (1.5)$$

for which the correct value of the WIMP DM relic density is obtained (for a more detailed derivation, see Steigman et al. (2012)). A DM particle with a typical velocity of $v \approx 0.1c$ corresponds to a cross-section of weak strength for WIMPs with electroweak scale masses. This coincidence is now known as the ‘‘WIMP miracle’’.

1.2.2.2 Supersymmetric candidates

One possible solution to identifying DM particles as WIMPs is an extension of the SM known as supersymmetry (SUSY). SUSY is the theoretical link between two different SM classes of particles; fermions and bosons. Fermions and bosons are classified based on a property called spin; bosons have integer spins and fermions half-integer spins. Many particle physics theories predict that the lightest SUSY particles should be stable and electrically neutral, interacting weakly with SM particles, making SUSY particles an ideal candidate for DM ([Goldberg, 1983](#); [Ellis et al., 1984](#); [Roszkowski, 2004](#)).

There are several SUSY particles that are suitable as DM candidates, including the neutralino (a collective term for the superpartners of the Z boson, the photon and the Higgs), sneutrino (the superpartner of the neutrino), and gravitino (the superpartner of the hypothetical graviton). All of these particles are weakly interacting and electrically neutral. However, the sneutrino does not reproduce the correct relic densities and annihilates too quickly in the early universe to be cosmologically significant ([Falk et al., 1994](#); [Hall et al., 1998](#)). The gravitino can also be ruled out as a DM candidate as they would act as hot DM ([Chun et al., 1994](#); [Borgani et al., 1996](#)), leaving the neutralino as the only viable SUSY DM WIMP candidate (see [Jungman et al. 1996](#) for a review), although recent results from the Large Hadron Collider (LHC) have placed strong restraints on the neutralino parameter space ([Bélanger et al., 2013](#)).

1.2.3 Other candidates

The increasing limits placed on the WIMP parameter space and a lack of a convincing signal in WIMP DM searches have led to many alternative DM candidates being suggested. Below we explore some of these alternatives, however for a comprehensive review see [Baer et al. \(2015\)](#).

1.2.3.1 Axions

An alternative candidate to WIMPs, axions are hypothetical elementary particles first introduced to solve the charge-parity (CP) violation in quantum chromodynamics (QCD) and are often considered to be a strong contender as a DM particle (Sikivie, 1983).

Interactions between SM particles and axions are expected to be very weak, implying that they were not in thermal equilibrium in the early universe; they are also predicted to have very low mass $\leq 0.01\text{eV}$ (Sikivie, 1983). There is still uncertainty in whether axions are able to reproduce the relic density, depending strongly on the production mechanisms. Even so, within a limited range, axions are capable of satisfying all conditions and are still considered as a plausible DM particle candidate (Rosenberg & van Bibber, 2000; Marsh, 2016).

1.2.3.2 Sterile neutrinos

Another non-WIMP DM particle candidate is the sterile neutrino, a hypothesised new flavour or type of neutrino (Abazajian et al., 2012). The lightest of the SM particles, neutrinos, are classified into three flavours (electron, muon, tau) and interact very rarely with baryonic matter via the weak nuclear force, whereas the sterile neutrino is predicted to interact only via gravitational potential. Neutrinos flavours are expected to exist in equal quantities. However, some experiments have observed an excess in the number of electron neutrinos and theorise that the sterile neutrino is a temporary state of an electron neutrino.

Sterile neutrinos alone are unlikely to contribute to the total abundance of DM in the Universe due to their insufficient mass and quantity. However, just like standard neutrinos, it is possible that sterile neutrinos exist in three flavours, with different masses, and facilitates the idea of other sterile particles.

1.2.3.3 MACHOs

Since we know DM must be ‘dark’ (i.e. non-luminous), several astrophysical objects were suggested as possible DM candidates, such as neutron stars, brown dwarfs, black holes and unassociated planets. These ‘dark’ objects are classified as MACHOs (MASSIVE Compact Halo Objects).

The search for MACHOs in the Milky Way halo via gravitational microlensing conducted by the MACHO Collaboration ([Alcock et al., 1992](#)) and the EROS-2 Survey, amongst others, have been relatively unsuccessful. The MACHO Collaboration only detected 13-17 possible lensing events from ~ 12 million stars ([Alcock et al., 2000](#)), and EROS-2 found even fewer with one lensing event from ~ 7 million stars ([Tisserand et al., 2007](#)). The percentage of non-luminous matter in our galaxy is too high to be solely accounted for by such a low number of MACHOs. An additional failure in the MACHOs hypothesis as a DM candidate is the requirement that DM must be non-baryonic to preserve big bang nucleosynthesis.

1.3 Detecting dark matter

In this section, we explore where in the Universe DM may be observable and examine several methods and techniques used with the aim of detecting DM.

The observationally confirmed presence of a DM halo in our Galaxy provides an interesting source of investigation for DM particle searches. There are several experimental methods used to detect DM interactions with SM particles, including collider searches, direct detection and indirect detection; these are shown in Fig. 1.1. Collider searches examine the resulting SM particles of proton-proton collisions, searching for missing energy, which can be associated with the production of WIMPs ($SM\ SM \rightarrow DM\ DM$). Below we focus on direct DM detection (Sec. 1.3.1), where DM elastically scatters off a SM particle ($SM\ DM \rightarrow SM\ DM$), and indirect DM detection (Sec. 1.3.2), where DM particles self-interact or annihilate to produce observable SM particles ($DM\ DM \rightarrow SM\ SM$).

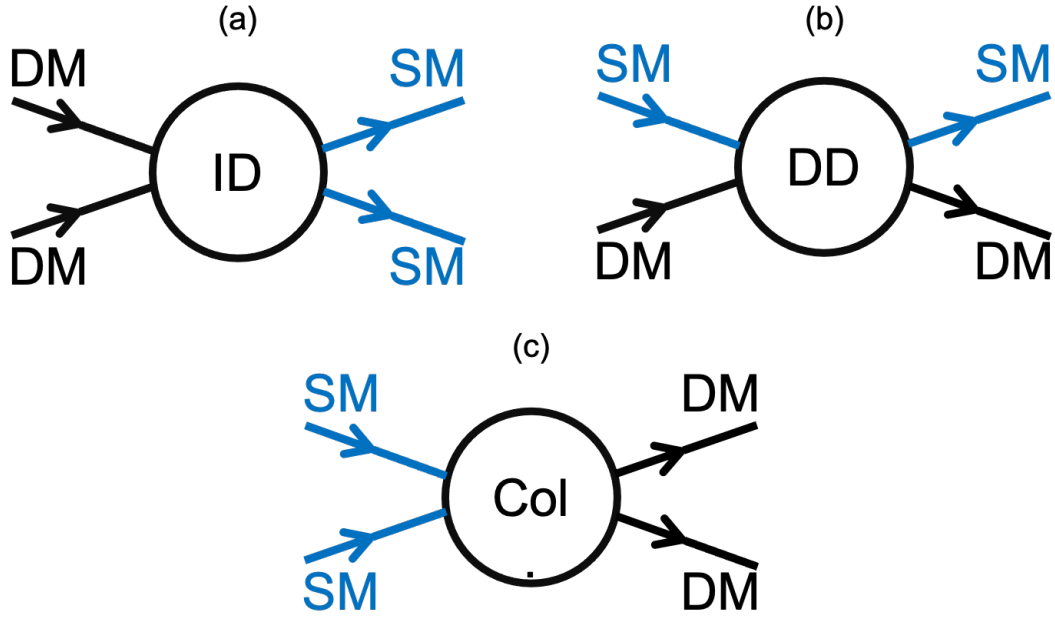


FIGURE 1.1: Diagram showing dark matter (DM) interactions and their corresponding experimental detection techniques. (a) shows DM annihilation into Standard Model (SM) particles via indirect detection (ID). (b) shows DM-SM particle scattering via direct detection (DD). (c) shows DM particle production from annihilation of SM particles in collider (Col) experiments.

1.3.1 Direct detection

The observational evidence of DM in the Milky Way strongly motivates the search for a DM particle scattering off of a nucleus. Numerous particle and nuclear physics experiments have played an important role in searching for evidence of this detection (Akerib et al., 2003; Akerib et al., 2013, 2017; CRESST collaboration et al., 2017; Aprile et al., 2017b, 2018; Akerib et al., 2020; The DarkSide Collaboration et al., 2018; Zhou et al., 2020).

Direct detection of DM aims to measure the nuclear recoil energy of a standard model particle induced by the scattering of a WIMP. The differential scattering rate of a WIMP-nuclei interaction can be written as,

$$\frac{dR}{dE}(E, t) = \frac{\rho_0}{m_{\text{DM}} m_N} \int_{v_{\text{min}}}^{v_{\text{esc}}} v f_E(\vec{v}) \frac{d\sigma}{dE}(v, E) d^3\vec{v}, \quad (1.6)$$

where ρ_0 is the local DM density, m_{DM} and m_N are the DM and nuclei particle masses (respectively), v_{min} is the minimum velocity the particle requires to produce a detection at the recoil energy E , \vec{v} is the velocity vector of the DM particle relative to the Earth, $f_E(\vec{v})$ is the corresponding velocity distribution function, and $d\sigma/dE$ is the energy differential DM-nucleus scattering cross-section. The minimum velocity depends on the threshold recoil energy in the form:

$$v_{\text{min}} = \sqrt{\frac{Em_N}{2\mu_{\text{DM},N}^2}}, \quad (1.7)$$

where $\mu_{\text{DM},N} \equiv (m_{\text{DM}}m_N)/(m_{\text{DM}} + m_N)$ is the DM-nucleus reduced mass.

In order to determine a limit on the WIMP-nucleon scattering cross-section from the measurement of the scattering rate (Eq. 1.6) several assumptions must be made. The particle physics assumptions include the nucleon form factor used and the type of WIMP-nucleon scattering. The astrophysical assumptions are typically rounded up into the Standard Halo Model (SHM). The SHM assumes that the velocity distribution of the DM is smooth and well described by a Maxwellian distribution, and the local DM density is a fixed value ($\rho_0 = 0.3 - 0.4 \text{ GeV}/\text{cm}^3$), however, the local DM density may suffer from large uncertainties. Additionally, the SHM assumes that the WIMP-nucleon scattering is elastic, conserving all energy. The SHM's assumptions and uncertainties are explored fully in Section 2.2.2.

The only hint of a possible direct DM detection was made by the discovery of an annual modulation signal by the DAMA/NaI (Bernabei et al., 2003) experiment, which was later confirmed by the same collaboration DAMA/LIBRA (Bernabei et al., 2008). The DAMA collaboration concluded that the annual modulation found in its data was consistent with the expected signal from DM particles in our Galactic halo (Drukier et al., 1986a; Freese et al., 1988). This detection is considered to be extremely controversial, with an additional positive signal from CDMS-II (CDMS Collaboration et al., 2013), however numerous null results have been reported from other direct detection experiments (e.g. CDMS (Akerib et al., 2003; Ahmed et al., 2009), CoGeNT (Aalseth et al.,

2008), COUPP (Behnke et al., 2008), TEXONO (TEXONO Collaboration: S. T. Lin, 2007) and XENON10 (Angle et al., 2008)).

Currently, the measurements of the WIMP-nucleon scattering rate has not lead to any confirmed DM signal and as a result, the limits on the WIMP-nucleon cross-section as a function of DM mass are continually being lowered. The strongest constraints on the WIMP-nucleon cross-section¹ come from null results of DM searches in the liquid-gas xenon detector XENON1T (Aprile et al., 2018), setting a limit of $4.1 \times 10^{-47} \text{cm}^2$ at $30 \text{ GeV}/c^2$ and 90% confidence level. A further improvement in the cross-section limits is expected to come from direct detection experiment, such as XENONnT (Aprile et al., 2020), LZ (Akerib et al., 2020) and DARWIN (Aalbers et al., 2016) experiments. These experiments will push the cross-section down to the neutrino scattering limit, at which point any signal from a WIMP-nucleon scattering would be indistinguishable from coherent neutrino scattering (Billard et al., 2013).

1.3.2 Indirect detection

An alternative to DM direct detection is indirect detection, a technique used to identify SM particles produced from DM annihilations or decays by observing the resultant γ -ray radiation. For the case that a DM particle annihilates into γ -rays, the γ -ray flux is given by:

$$\frac{d\phi_\gamma}{dE} = \frac{\langle\sigma v\rangle}{8\pi m_\chi^2} \frac{dN_\gamma}{dE} J(E), \quad (1.8)$$

where the particle physic terms are; the mass of the DM particle m_χ , the velocity-averaged DM annihilation cross-section $\langle\sigma v\rangle$ and the γ -ray spectrum generated from a single annihilation dN_γ/dE . The γ -ray spectrum varies depending on the annihilation channel and the mass of the WIMP, typically this is dominated by annihilation into $b\bar{b}$ pairs with $\tau^+\tau^-$ lepton pairs also contributing (other quarks and lepton pairs are also possible annihilation channels). If the annihilation has a large contribution of e^+e^- pairs

¹In this work we only consider a spin-independent cross-section

this would likely enhance the γ -ray signal via inverse Compton scattering (Baltz & Wai, 2004; Regis & Ullio, 2008).

The astrophysical term in equation 1.8, $J(E)$ (called the J-factor) is defined by:

$$J(E) = \int_{\Delta\Omega} \int_{los} \rho_\chi^2 ds d\Omega, \quad (1.9)$$

where ρ_χ is the density of DM, and the integral is along the line of sight and over solid angles. Given that both the astrophysical and particle physics terms are unknown, assumptions need to be made to one of these to constrain the other. The astrophysical uncertainties from both the DM density profiles and the astrophysical foreground are one of the significant challenges in the indirect detection of DM.

Using γ -rays to study DM annihilations has several unique benefits. Firstly, γ -rays do not get deflected by magnetic fields and therefore point back to the site at which they are created. This allows for γ -ray searches in both close and distant objects, such as the Milky Way and satellite galaxies. An additional advantage of the use of γ -rays, is that they are unaffected by attenuation, and therefore retain spectral information from their source when observed on Earth.

Indirect DM detection methods use space and ground-based telescopes to search for γ -rays produced from WIMP-WIMP annihilations that occur at galactic or extragalactic scales. Currently, the space-based Large Area Telescope (LAT) (GLAST Facility Science Team et al., 1999; Charles et al., 2016) on board the Fermi satellite and the ground-based instruments such as the High-Energy Stereoscopic System (H.E.S.S) (Hinton & HESS Collaboration, 2004), the Major Atmospheric Gamma-ray Imaging Cherenkov (MAGIC) (Lorenz & MAGIC Collaboration, 2004) and the Very Energetic Radiation Imaging Telescope Array (VERITAS) (Weekes et al., 2002), have all been searching for the signatures of DM annihilation. Although there has been no positive detection of γ -rays from DM using these instruments, important conclusions of the properties of DM particles can still be made. For example, results from Fermi-LAT have pushed the

annihilation interaction rate limits below the canonical thermal relic production cross-section of $3 \times 10^{-26} \text{ cm}^3 \text{ s}^{-1}$ for a WIMP of mass $\sim 10 \text{ GeV}$ (Ackermann et al., 2011; Geringer-Sameth & Koushiappas, 2011; Mazziotta et al., 2012).

Currently under construction, the Cherenkov Telescope Array (CTA) is the next generation of ground-based γ -ray observatories (CTA Consortium & Ong, 2019). CTA will push the limits on DM annihilation signals, sensitive to γ -rays with energies from a few tens of GeV to hundreds of TeV, improving the sensitivity by an order of magnitude (at 1 TeV) when compared to previous experiments. To achieve optimal sensitivity across this wide energy range, CTA will consist of over 100 separate telescopes of three different sizes across sites in the Northern and Southern hemispheres, becoming the first ground-based γ -ray observatory to survey almost the entire sky.

1.3.3 Targets for DM detection

For direct and indirect experiments, searches for DM particles are broadly constrained to three areas: the Galactic centre (GC), the Solar neighbourhood, and dwarf satellites.

1.3.3.1 DM in the Galactic centre

Due to its relative proximity and high density of DM, the GC of the Milky Way is an attractive location for DM indirect detection searches. However, searching for DM in the GC does have its disadvantages and challenges. Firstly, despite the density of DM being very high, the baryonic matter density increases even faster near the GC, meaning that DM is a subdominant component of the total mass density in the very inner region of the galaxy. Therefore, any gravitational models, for example, from stellar velocities near the GC, are unable to precisely constrain the density of DM in this region, resulting in significant uncertainties.

Another problem with DM searches in the GC relates to the dense astrophysical background. The GC is a very astrophysically active region, hosting high energy sources such as supernova remnants (Yusef-Zadeh et al., 1999), highly ionised gas (Wang et al.,

2002), massive O/B stars (Schödel et al., 2009), dense molecular clouds (Ferrière, 2012) and populations of pulsars (Wharton et al., 2012). Many of these objects and events produce very high energy γ -ray emission, which must be untangled to distinguish any underlying DM emission.

1.3.3.2 DM in the Solar neighbourhood

The density of DM in the region of our solar system is of great importance to the prospects for direct and indirect detection. The local DM density is calculated from the rotation curves of the Milky Way, with uncertainties arising due to our location within our galaxy. Rotation curves are able to measure the total mass within a system; therefore, the density distributions of the galactic bulge and disc are needed to accurately calculate the DM profile. Direct and indirect detection rates also require the velocity distribution of DM in the local region, again inferred from rotation curves.

From recent observational results from stellar kinematics, stellar density profiles, maser observations and gas velocities suggest that the local DM density is within a large range of values of $\rho_0 \sim 0.45 - 0.70 \text{ GeV cm}^{-3}$ (Smith et al., 2012; Bienaymé et al., 2014; Sivertsson et al., 2018; Hagen & Helmi, 2018; Piffi et al., 2014). Typically, the local DM density is taken to be $\rho_0 = 0.3 \text{ GeV cm}^{-3}$ (Green, 2017; Read, 2014).

The local DM density and velocity distribution are discussed further in Chapter 2.

1.3.3.3 DM in Milky Way satellite galaxies

Dwarf satellite galaxies have long been of interest to DM searches and are one of the smallest environments dominated by DM. Although these galaxies are far more distant than the GC, the observed emitting region is much larger. The first study into the kinematic properties of dwarf satellite galaxies measured the velocities of the constituent stars in Draco and Ursa Minor (Aaronson, 1983), discovering very high mass-to-light ratios, further studies found similarly high ratios. For example, the mass-to-light ratio of Draco is ~ 250 in Solar units, and Sagittarius is ~ 100 . These results suggest that

dwarf galaxies are amongst the most extreme DM dominated systems, and are ideal targets for detection experiments.

1.4 Simulations

This section gives a brief overview of the history and evolution of cosmological hydrodynamical simulations. We also discuss the importance and relevance of zoom-in simulations. Finally, we introduce the cosmological hydrodynamic simulations used in this work; the ARTEMIS simulations.

1.4.1 Cosmological hydrodynamic simulations

The highly complex nature of the mechanisms that determine galaxy formation, and therefore the growth and evolution of structure in the universe, requires sophisticated numerical techniques to model them accurately.

The current generation of state-of-the-art numerical simulations originates from much simpler models. The very first gravitational simulation was carried out in the 1940s and contained only 37 particles, represented as light bulbs, and the gravitational forces between them were interpreted from the flux (Holmberg, 1941). With the advancement of technology and digital computing, the calculations involved in numerical simulations became easier to solve. By the 1960's collisionless N-body gravitational simulations were possible, now consisting of ~ 100 particles (Von Hoerner, 1960, 1963; Aarseth, 1963). The size and complexity of simulations continued to increase, making it possible to study the growth of cosmological structure on large scales. Press & Schechter (1974) laid the foundations for these studies, using N-body simulations to model hierarchical structure formation, investigating the mass distribution of halos. Gravitational N-body simulations have been very successful in contributing to our knowledge of the nature of DM. For example, Navarro et al. (1996) studied the structure of DM halos and determined a universal DM halo density profile. The one billion DM particle Millennium simulation (Springel et al., 2005) has provided new insights into the formation, growth

and distribution of DM structures on extremely large scales. However, for the study of astrophysical objects on smaller scales, such as individual galaxies (Milky Way-like and dwarfs), applying gravitational forces alone is insufficient. The impact baryons have on the formation and evolution of structure becomes increasingly important. This has led to the development of hydrodynamical simulations, linking the gravitational and baryonic (gas and stars) prescriptions together, tracking the interactions between DM and baryons. Including baryonic physics furthers our understanding of the physics of DM, as the latter may be influenced by the kinematics of the baryons. Hydrodynamic simulations offer many advantages over gravitational-only simulations, reproducing observations on galactic scales with greater accuracy. However, hydrodynamic simulations suffer from decreased resolution (number of particles and/or size of particles) due to the increase in the numerical calculations required per particle.

The resolution limit of hydrodynamic simulations means that small-scale astrophysical processes cannot be fully modelled. To overcome this challenge, astrophysicists use analytical techniques or “subgrid models” to model phenomena too small to resolve. The physics used in these subgrid models vary depending on the objective of each simulation. However, the majority adopt models that describe radiative cooling, stellar formation, stellar evolution and chemodynamics, supernova and black holes. The parameters of these subgrid models are motivated by physical or observational theories, although in some parameters, this is not possible. That means that some subgrid physics has to be calibrated. One of the most common calibration methods is to choose a set of statistics, such as the stellar mass function, and tune the subgrid parameter until the simulations match those statistics. This method has been used in several successful simulations; Illustris ([Vogelsberger et al., 2013](#); [Torrey et al., 2014](#)), EAGLE ([Crain et al., 2015](#); [Schaye et al., 2015](#)), BAHAMAS ([McCarthy et al., 2017](#)) and IllustrisTNG ([Pillepich et al., 2018](#)).

1.4.2 Zoom-in simulations

Cosmological ‘zoom-in’ simulations have recently become the go-to solution for modelling cosmology on Milky Way scales, intending to alleviate the problem of limited

resolution. Zoom-in simulations are achieved by simulating a region of interest, such as a DM halo, to a very high resolution while the surrounding area remains much lower. The low-resolution area provides realistic effects (i.e. tidal fields) influencing particles in the high-resolution area. This technique allows for single halos to be studied in much greater detail without having to simulate non-cosmological isolated halos.

In recent years several groups have used cosmological zoom-in simulations to study galaxies with similar properties to the Milky Way. The Auriga project has studied the formation and evolution of Milky Way-like galaxies and their discs (Grand, 2016; Grand et al., 2017), the morphologies and kinematics of Milky Way-like galaxies are studied in the FIRE-2 simulations (Garrison-Kimmel et al., 2018), stellar discs of Milky Way-like galaxies have been investigated with the NIHAO-UHD suite of simulations (Buck et al., 2020) and the APOSTLE simulations study Local Group galaxies, including satellites of the Milky Way and Andromeda (Sawala et al., 2016).

As mentioned in Section 1.1.5, hydrodynamic simulation can help to solve the small-scale problems associated with Λ CDM. The higher resolution of zoom-in simulations allows for more accurate modelling of baryonic feedback and the resulting effects on galaxies and their environments, helping to better understand and resolve these issues. For example, the too-big-to-fail problem can be alleviated by combining stellar feedback, which lowers the DM density in the galaxy's centre and creates a shallower density profile, and tidal effects that change the mass distribution of both the dark matter and the baryons (Tomozeiu et al., 2016). Additionally, Sawala et al. (2014) have shown that they can solve several of the Λ CDM small-scale problems, determining that the problems are caused by inadequate inclusion of baryonic physics.

1.4.3 The ARTEMIS simulations

The ARTEMIS (Assembly of high-ResoluTion Eagle-simulations of MILky Way-type galaxieS) simulations are a new suite of high-resolution cosmological hydrodynamical simulations of Milky Way-mass halos that trace the evolution DM, gas, stars and black holes across redshifts from $z = 127$ to today $z = 0$ (Font et al., 2020). The ARTEMIS

simulations employ a comprehensive suite of baryon physics, including metal-dependent radiative cooling, star formation, stellar evolution and chemodynamics, black hole formation and growth through mergers and gas accretion, along with stellar feedback and feedback from active galactic nuclei (AGN). The work presented here focuses on the last snapshot at $z = 0$, which reflects the simulated state of today’s Universe.

The ARTEMIS simulations are run with the same hydrodynamical simulation code used for the EAGLE project (Schaye et al., 2015; Crain et al., 2015), but applied here at significantly improved spatial and mass resolution using the ‘zoom in’ technique (e.g. Bertschinger (2001)). This allows for the simulation of Milky Way-analog halos at high resolution and with hydrodynamics, within a larger box that is simulated at comparatively lower resolution and with collisionless dynamics only. The initial conditions (ICs) were generated using the MUSIC code² (Hahn & Abel, 2011). Halos were selected from a base periodic box is $25 \text{ Mpc } h^{-1}$ on a side with 256^3 particles. The initial conditions were generated at a redshift of $z = 127$ using a transfer function computed using the CAMB³ Boltzmann code (Lewis et al., 2000) for a flat Λ CDM WMAP9 (Hinshaw et al., 2013) cosmology ($\Omega_m = 0.2793$, $\Omega_b = 0.0463$, $h = 0.70$, $\sigma_8 = 0.8211$, $n_s = 0.972$).

The resolution of the ARTEMIS simulations are similar to that of the highest resolution simulations from other groups, such as the Auriga simulations (Grand et al., 2017), the APOSTLE simulations (Sawala et al., 2016), the FIRE-2 simulations of Milky Way-analog halos (Garrison-Kimmel et al., 2018). At this resolution, the DM particle mass is $1.17 \times 10^5 M_\odot/h$ and the initial baryon particle mass is $2.23 \times 10^4 M_\odot/h$. In general, the sample size of Milky Way-analog halos in ARTEMIS is larger than other studies, providing us with the opportunity to investigate the uncertainties due to cosmic variance.

The ARTEMIS Milky Way-analogs have been selected such that the total mass of the halo lies in the range $8 \times 10^{11} < M_{200,\text{crit}}/M_\odot < 2 \times 10^{12}$, where $M_{200,\text{crit}}$ is the mass enclosing a mean density of 200 times the critical density at $z = 0$. This approximately covers the range of inferred values for the Milky Way from a collection of different

²<https://www-n.oica.eu/ohahn/MUSIC/>

³<https://camb.info/>

observations (Guo et al., 2010; Deason et al., 2012; McMillan, 2017; Watkins et al., 2019). There are 63 halos in this mass range, of which dark matter-only simulations have been constructed. For the work presented here, in Chapter 2 we use 42 of the dark matter-only halos and their hydrodynamic counterparts, and in Chapter 3 we use 45 halos.

Fig. 1.2 shows composite SDSS-like surface brightness maps for 42 of the ARTEMIS Milky Way-analogues at redshift $z = 0$. Each of the 42 galaxies is shown in both a face-on and edge-on projection. Some of these galaxies are currently undergoing interactions with satellite galaxies, while others appear to be reasonably isolated. Due to the large sample size we have at our disposal, we are able to examine a range of diverse formation and merger histories, as the exact formation history of the Milky Way is still unknown.

The main objective of this thesis is to explore the effect of baryons and the uncertainties associated with direct (Chapter 2) and indirect (Chapter 3) DM detection using a new suite of high-resolution cosmological hydrodynamic simulations of Milky Way-like galaxies, to aid in the identification of DM. Using the Milky Way-like galaxies in the ARTEMIS suite of simulations provides several key advantages. One of them is that the sample is fairly large (45 galaxies) and therefore it includes a variety of formation histories, giving us the opportunity to study a wide range of Milky Way analogues. This allows us to take into account several factors when comparing the simulation results with observations, such as the stochastic properties of the present-day satellite galaxies, or the formation histories of the hosts. Additionally, with both DM-only Milky Way analogues and their hydrodynamic counterparts at our disposal, the effects of baryons on these galaxies, satellites and their surrounding environments can be studied. This thesis focuses on several areas of interest for DM searches, including predicted signals from the Galactic centre, the solar neighbourhood and Milky Way satellites, with the aim of understanding the uncertainties associated with DM detection techniques.

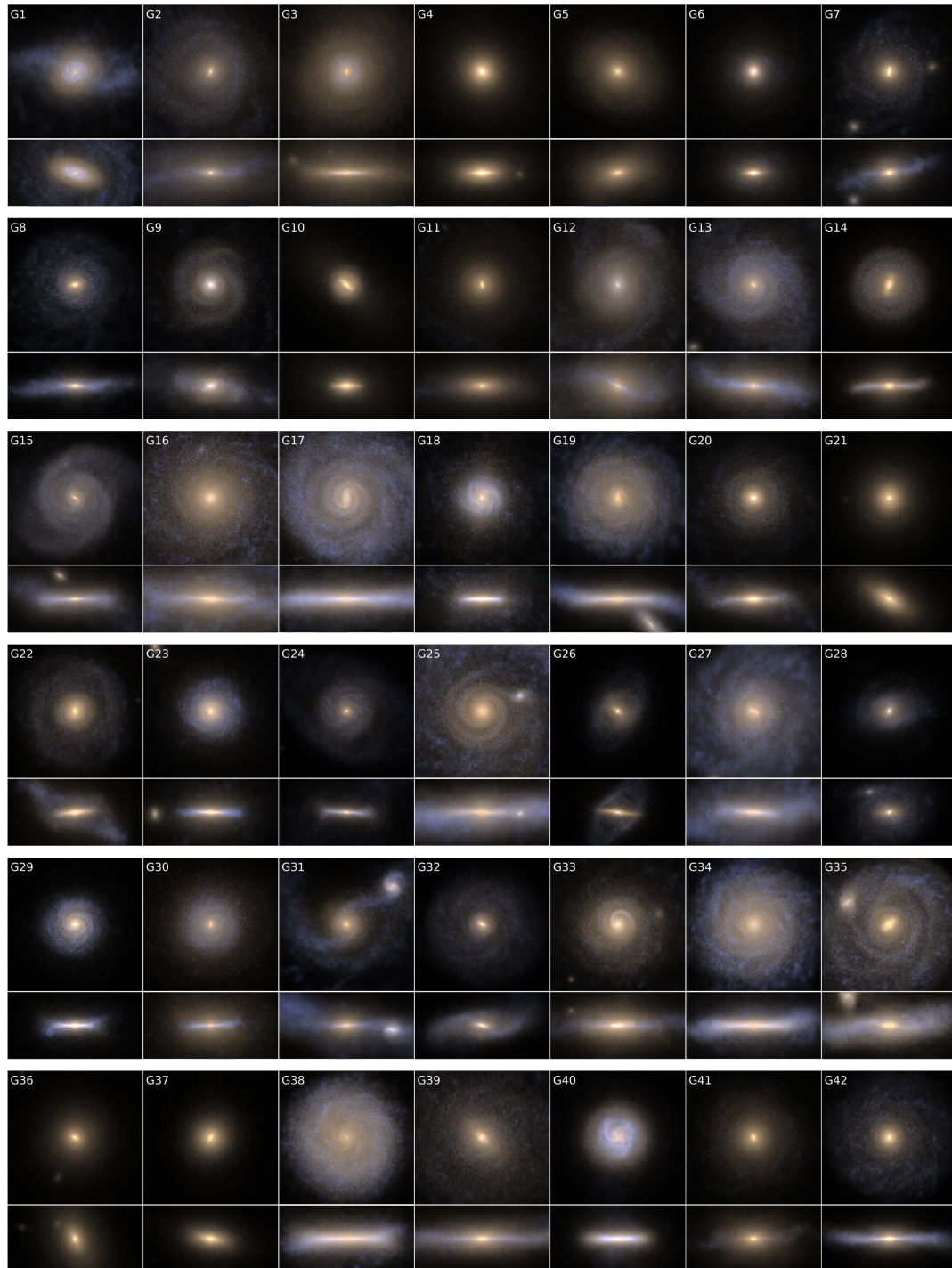


FIGURE 1.2: Composite surface brightness maps of the ARTEMIS halos at redshift $z = 0$. Colours show the SDSS luminosities; i-band (red), r-band (green) and g-band (blue). Galaxies are labelled G1-G42, with the upper and lower panels showing the face-on and edge-on projections, respectively. The maps have been created with Py-SPHViewer ([Benitez-Llambay, 2015](#)).

Chapter 2

Informing dark matter direct detection limits with the ARTEMIS simulations

The majority of the work presented in this chapter was published in a peer reviewed journal:

Poole-McKenzie, R., Font, A. S., Boxer, B., McCarthy, I. G., Burdin, S., Stafford, S. G., and Brown, S. T. (2020). Informing dark matter direct detection limits with the ARTEMIS simulations. *Journal of Cosmology and Astroparticle Physics*, 2020(11), 016.

2.1 Introduction

Dark matter (DM) is the most important contributor to the mass budget in the Universe and plays a vital role in the formation of large-scale and galactic structures. Numerous particle candidates beyond the Standard Model (SM) have been proposed for DM. Among them, the so-called Weakly Interacting Massive Particle (WIMP) ([Steigman & Turner, 1985](#); [Arcadi et al., 2018](#)) has been studied extensively. Definitive evidence for the existence of WIMPs, or of any other DM candidates, is actively sought via both direct and indirect detection experiments. In particular, direct detection experiments aim to detect WIMPs by measuring the nuclear recoil energy resulting from their elastic

scattering off of atomic nuclei (Goodman & Witten, 1985). Indirect detection experiments, on the other hand, make use of either space- or ground-based telescopes to search for SM particles produced from the decay of WIMPs or from WIMP-WIMP annihilations that could occur within the Galaxy and/or in extragalactic sources (for a review see Arcadi et al. (2018)). In this study we focus on the predictions for the direct detection limits, using cosmological simulations. We focus on the potential signal from the solar neighbourhood in our Galaxy, which is deemed to be an important site for direct detection of DM.

To date there is no conclusive evidence for direct detection of DM. While some positive signals have been reported from the DAMA/LIBRA (Bernabei et al., 2013) and CDMS-II (CDMS Collaboration et al., 2013), the evidence is not strong. At the same time, various null results have been reported from many other experiments, including the XENON1T (Aprile et al., 2017a), which is one of the most sensitive experiments to date.

The predictions for the direct detection signals often assume the validity of the Standard Halo Model (SHM) (Drukier et al., 1986b). As the differential event rate in WIMP elastic scattering depends on both the local density and velocity distribution of WIMPs, the SHM involves certain assumptions about these distributions. From the assumption of a smooth, spherically symmetric DM halo, the velocity distribution of DM particles follows a Maxwell-Boltzmann function. The SHM also relies on observational measurements of several local Galactic parameters, such as the local DM density (ρ_0), circular velocity (v_0) and escape speed (v_{esc}). Some of these measurements are still affected by systematic uncertainties (for example, ρ_0), and these measurements are inherently based on model assumptions for the Galaxy.

Cosmological simulations can provide useful insights into some of the uncertainties in the SHM assumptions and how these propagate into direct detection limits (Bozorgnia & Bertone, 2017). Both DM-only and hydrodynamical simulations have been used to study whether the DM velocities can deviate from a Maxwellian distribution. These deviations can occur, for example, when tidal streams cross the solar neighbourhood.

Deviations would result in the local velocity distribution being characterised by discrete peaks which, if ignored, could significantly bias the derived direct detection limits or measurements (e.g., [Stiff & Widrow \(2003\)](#)). Interactions with other galaxies can move the Galaxy away from dynamical equilibrium and give rise to deviations from a Maxwellian distribution.

In this respect, some simulations suggest that the local DM velocity distribution can be significantly non-Maxwellian ([Vogelsberger et al., 2009](#); [Kuhlen et al., 2010](#); [Ling et al., 2010](#); [Lisanti et al., 2011](#); [Mao et al., 2013](#); [Gilmore, 1997](#); [Sloane et al., 2016](#)). For example, [Vogelsberger et al. \(2009\)](#) analyse the Aquarius simulations ([Springel et al., 2008](#)) and find secondary peaks in the velocity distribution of DM halos at $v \geq 250 \text{ km s}^{-1}$, attributing these to the formation history of individual halos. Using a hydrodynamical simulation of a single Milky Way-sized halo, [Ling et al. \(2010\)](#) find that a Tsallis distribution ([Tsallis, 1988](#)) best fits the velocity distribution. Using a sample of 96 halos simulated with hydrodynamics, [Mao et al. \(2013\)](#) find that the stacked velocity distribution has a wider peak and a steeper tail than a simple Maxwellian and suggest that the largest uncertainty in the velocity distribution arises from the radial position in the Milky Way with respect to the scale radius of the DM halo. In contrast, several other studies using cosmological hydrodynamical simulations find that the Maxwellian adopted in the SHM is a suitable approximation for the local velocity distribution. This has been shown, for example, by [Kelso et al. \(2016\)](#) for two Milky Way-mass halos from the MaGICC simulations ([Stinson et al., 2013](#)), and by [Bozorgnia et al. \(2016\)](#) for galaxies in the EAGLE ([Schaye et al., 2015](#)) and APOSTLE ([Sawala et al., 2016](#)) simulations.

Note that the inclusion of baryons and associated physics in simulations may not only modify the local velocity distribution of the DM, but the baryons will also have a non-negligible impact on the spatial distribution of the DM, altering both its shape and its concentration (e.g., [Read et al. \(2008\)](#); [Duffy et al. \(2010\)](#); [Deason et al. \(2011\)](#); [Pontzen & Governato \(2012\)](#); [Schaller et al. \(2015\)](#)).

A dark disc can also potentially boost the DM signal in comparison with standard predictions using the SHM. Studies using hydrodynamical simulations have found that a

dark disc has a negligible contribution ($< 25\%$) to the local DM density and hence are not expected to contribute much to the DM direct detection signal (Purcell et al., 2009; Ling et al., 2010; Gilmore, 1997; Billard et al., 2013). However, Read et al. (2009) found a wider range for the contribution of dark discs, of $(0.25 - 1.5) \times$ the non-rotating DM halo density near the Sun. A significant dark disc can increase the WIMP detection rates, e.g., by a factor of ≈ 3 at recoil energies of $5 - 20$ keV (Bruch et al., 2009) and thus improve the constraints on the interaction cross-section.

In this study, we aim to re-evaluate the spatial and kinematical distribution of local DM and to examine the prevalence of dark discs and of local substructure using a new set of high-resolution hydrodynamical simulations, as well as to estimate how these structures can potentially impact the DM direct detection limits. The new suite of high resolution, zoomed-in simulations, called ARTEMIS, follows the growth of 42 Milky Way-mass galaxies in a Λ CDM cosmological model. Each halo in the suite has two realisations: a collisionless version (hereafter DMO) and a fully hydrodynamical version (hereafter ‘hydro’). ARTEMIS is the largest sample to date for this type of prediction at such high resolution (with baryon and dark matter simulation particle masses of $2.2 \times 10^4 M_{\odot} h^{-1}$ and $1.2 \times 10^5 M_{\odot} h^{-1}$, respectively). As we discuss below, and as previously shown in Font et al. (2020), the ARTEMIS simulations reproduce the observed stellar masses and disc sizes of Milky Way-mass galaxies remarkably well and should therefore realistically capture the gravitational impact of the baryons on the DM (and vice-versa).

This large suite of simulations allows us to investigate not only the impact of baryons in a realistic way, but also allows us to assess the impact of halo-to-halo scatter on the predictions. Furthermore, by using the local density and local velocity distributions of DM from these simulations and their scatter, we can inform the detection limits in direct detection experiments such as LUX-ZEPLIN (LZ) (Akerib et al., 2020) and XENON1T. In practice, this means that the existing detection limits actually turn into fuzzy bounds when one propagates the halo-to-halo scatter through, implying that the limits themselves have non-negligible uncertainties.

The paper is organised as follows. In Section 2.2, we introduce the set of high resolution, cosmological hydrodynamical simulations of Milky Way-mass galaxies that

will be used in our study. We also briefly discuss the formalism of the SHM and of predicting the direct detection signal. In Section 2.3 we determine the range of local DM densities in the simulated halos, the distribution function of DM velocities in their solar neighbourhoods and estimate the impact that substructure may have locally. In Section 2.4 we investigate other (non-local) changes in the structure of DM, including changes in the DM halo shapes, and we search for evidence of dark discs in these halos. In Section 2.5, we show how the variations in the local DM properties may affect the predicted exclusion limits of DM direct detection experiments, namely those for LZ and XENON1T. We also adopt an empirical model for the local velocity distribution based on our simulations and show how it compares to the SHM predictions. Finally, in Section 2.6, we summarise our findings and conclude.

2.2 Methods

2.2.1 The ARTEMIS simulations

We use the new ARTEMIS suite of high-resolution cosmological hydrodynamical simulations of Milky Way-mass halos (Font et al., 2020). Full details of the simulations are provided in Font et al. (2020), but we provide an overview of the simulations here.

The ARTEMIS simulations employ the ‘zoom in’ technique (e.g. Bertschinger (2001)) to simulate Milky Way-analog halos at high resolution and with hydrodynamics, within a larger box that is simulated at comparatively lower resolution and with collisionless dynamics only. The initial conditions were generated using the MUSIC code¹ (Hahn & Abel, 2011). Halos were selected from a base periodic box of 25 Mpc h^{-1} on a side with 256^3 particles. The initial conditions were generated at a redshift of $z = 127$ using a transfer function computed using the CAMB² Boltzmann code (Lewis et al., 2000) for a flat Λ CDM WMAP9 (Hinshaw et al., 2013) cosmology ($\Omega_m = 0.2793$, $\Omega_b = 0.0463$, $h = 0.70$, $\sigma_8 = 0.8211$, $n_s = 0.972$), which we adopt here. The initial conditions include second order Lagrangian perturbation theory (2LPT) corrections.

¹<https://www-n.oica.eu/ohahn/MUSIC/>

²<https://camb.info/>

The base periodic volume was run down to $z = 0$ using the Gadget-3 code (last described in [Springel \(2005\)](#)) with collisionless dynamics. Milky Way analogs were selected based on total halo mass; specifically, [Font et al. \(2020\)](#) selected a volume-limited sample of halos (i.e., all halos) whose total mass fell in the range $8 \times 10^{11} < M_{200,\text{crit}}/M_{\odot} < 2 \times 10^{12}$, where $M_{200,\text{crit}}$ is the mass enclosed inside a sphere with radius $R_{200,\text{crit}}$, when the mean density is 200 times the critical density at $z = 0$. This approximately spans the range of values inferred for the Milky Way from a variety of different observations, i.e, $M_{200} \approx 0.55 - 2.62 \times 10^{12} M_{\odot}$ ([Bland-Hawthorn & Gerhard, 2016](#)). There are 63 such halos in this mass range in the periodic volume. In the present study, we use a subset of 42 high-resolution collisionless simulations (DMO), together with their full hydrodynamical counterparts, presented in [Font et al. \(2020\)](#). We note that the subset of 42 halos was not explicitly selected based on any physical criterion. They are the subset of halos that managed to run to $z = 0$ in the allotted HPC time allocation. Because of the nature of the halo mass function and that higher-mass halos tend to be more computationally expensive at fixed resolution, the high-mass end of the initial range is not particularly well sampled in the completed subset of 42. The resulting median (mean) halo mass of the subset is $M_{200,\text{crit}} \approx 1.01 (1.11) \times 10^{12} M_{\odot}$. A consequence of this is that the peak circular velocities tend to be on the lower side of that observed for the Milky Way, though there is some overlap.

The zoomed ICs were generated by first selecting all particles within $2R_{200,\text{crit}}$ of the selected halos and tracing them back to the initial conditions of the periodic box, at $z = 127$, to define the region which would be re-simulated at higher resolution and (for the hydro simulations) with baryons. The outer radius for particle selection was chosen to ensure that we simulate, at high resolution, a region that at least encloses the splashback radius, which marks the physical boundary of the halo out to which particles pass on first apocenter ([Diemer & Kravtsov, 2014](#)).

The base periodic run has a MUSIC refinement level of 8, whereas the zoom region has a maximum refinement level of 11. With this level of refinement, the DM particle mass is $1.17 \times 10^5 M_{\odot} h^{-1}$ and the initial baryon particle mass is $2.23 \times 10^4 M_{\odot} h^{-1}$. Following the convergence criteria discussed in [Power et al. \(2003\)](#), a force resolution

(Plummer-equivalent softening) of $125 \text{ pc}/h^{-1}$ (which is in physical coordinates below $z = 3$ and comoving coordinates at earlier times) was adopted.

Note the resolution of ARTEMIS is similar to that of the highest resolution simulations from other groups for this mass scale. For example, ARTEMIS lies between resolution levels 3 and 4 (with 3 the highest) of the Auriga simulations (Grand et al., 2017) and levels 1 and 2 (1 being the highest) of the APOSTLE simulations (Sawala et al., 2016), which also uses the EAGLE code. It is also comparable in resolution to the FIRE-2 simulations of Milky Way-analog halos (Garrison-Kimmel et al., 2018). However, in general the ARTEMIS sample is larger, in terms of the number of Milky Way analogs simulated at this very high resolution, and provides us with the opportunity to explore the uncertainties due to cosmic variance (i.e., halo-to-halo scatter) in the predictions.

To carry out the hydrodynamical zoomed simulations, ARTEMIS uses the Gadget-3 code with an updated hydro solver and galaxy formation modelling (subgrid physics) developed for the EAGLE project (Schaye et al., 2015). The EAGLE model includes subgrid prescriptions for important processes that cannot be resolved directly in the simulations, including metal-dependent radiative cooling, star formation, stellar evolution and chemodynamics, black hole formation and growth through mergers and gas accretion, along with stellar feedback and feedback from active galactic nuclei (AGN) (see Schaye et al. (2015) and references therein).

An important consideration for galaxy formation modelling is the calibration of the feedback efficiencies. At the scale of Milky Way-mass galaxies, stellar feedback is expected to dominate over that of AGN. Font et al. (2020) adjusted the parameter values of the stellar feedback model in the EAGLE code to reproduce the amplitude of the observed galaxy stellar mass–halo mass relation at the Milky Way halo-mass scale. This means that, at a given halo mass, the simulations have realistic stellar masses compared to the global galaxy population, by construction. This is crucial for the current study, as the simulations should, as a result, realistically include the gravitational impact of baryons on the underlying DM distribution (and vice-versa). While the simulations were not calibrated on other aspects of the observed galaxy population, they nevertheless

reproduce a number of key observables, including the disc size–stellar mass and star formation rate–stellar mass relations.

As noted above, the halo masses (and circular velocities) of the subset of 42 haloes tend to be on lower side of the allowed halo mass range for the Milky Way. Consequently, the stellar masses are typically also somewhat low compared to that quoted for the Milky Way (see [Font et al. \(2020\)](#) for discussion). Nevertheless, there is still some overlap between the ARTEMIS subset of 42 and the observed stellar mass of the Milky Way. For example, [Bland-Hawthorn & Gerhard \(2016\)](#) estimate a total stellar mass for the Milky Way of $5 \pm 1 \times 10^{10} M_{\odot}$, while ARTEMIS ranges from $(1.75 - 5.45) \times 10^{10} M_{\odot}$, with a mean (median) stellar mass of 2.87 (2.96) $\times 10^{10} M_{\odot}$.

It is important to note that there is a non-negligible (≈ 0.2 dex; e.g., [Behroozi et al. \(2013\)](#)) intrinsic scatter in the empirical stellar mass–halo mass relation of galaxies. This implies that, even if the simulations were to recover the stellar mass of the Milky Way perfectly (although, as noted above there is still considerable uncertainty in the observed mass), this would not automatically imply that the simulations would have the correct halo mass and/or circular velocity for the Milky Way. Indeed, we find that there is considerable scatter in the circular velocities at fixed stellar mass.

Given these uncertainties, our approach is to concentrate on the scatter in the implied DM detection limits for a sample of approximately fixed halo mass, and to examine the relative effects of hydro simulations to DM only simulations. We acknowledge that an alternative way to proceed would be to select simulated galaxies of approximately fixed stellar mass (ideally one consistent with estimates of the Milky Way) and explore the scatter that results from the scatter in halo mass and circular velocities. Given the nature of the halo mass-selected ARTEMIS sample, though, we must leave this for future work.

Returning to the discussion of the sample, the DMO halos have been matched with halos from the hydro simulations by using the unique particle IDs of the DM particles. By uniquely matching halos from the collisionless DMO simulations to those in the hydro simulations, we can unambiguously determine the impact of baryons on the DM spatial and velocity distributions. The global properties, including the spherical overdensity

masses and radii, the maximum circular velocities, and the local DM densities, for the halos in both the DMO and hydro simulations can be found in [Table 2.1](#).

TABLE 2.1: The main properties of the Milky Way-analog halos in the ARTEMIS simulations for the DMO and hydro cases. The columns include: The ID name of the simulated galaxy, the virial mass ($M_{200}^{\text{DMO/hydro}}$), the total stellar mass (M_*^{hydro}), the virial radius ($R_{200}^{\text{DMO/hydro}}$), the maximum circular velocity ($v_{\text{circ,max}}^{\text{DMO/hydro}}$), the local dark matter density ($\rho_0^{\text{DMO/hydro}}$), the local peak velocity ($v_0^{\text{DMO/hydro}}$) and the hydro peak azimuthal velocities for DM and stars ($v_{\phi,\text{peak,DM}}^{\text{hydro}}$).

Halo	M_{200}^{DMO} ($10^{11} M_\odot$)	M_{200}^{hydro} ($10^{11} M_\odot$)	M_*^{hydro} ($10^{10} M_\odot$)	R_{200}^{DMO} (kpc)	R_{200}^{hydro} (kpc)	$v_{\text{circ,max}}^{\text{DMO}}$ (km s^{-1})	$v_{\text{circ,max}}^{\text{hydro}}$ (km s^{-1})	ρ_0^{DMO} (GeV cm^{-3})	ρ_0^{hydro} (GeV cm^{-3})	v_0^{DMO} (km s^{-1})	v_0^{hydro} (km s^{-1})	$v_{\phi,\text{peak,DM}}^{\text{hydro}}$ (km s^{-1})	$v_{\phi,\text{peak,stars}}^{\text{hydro}}$ (km s^{-1})
G1	12.50	11.90	3.64	222.24	218.59	178.84	199.44	0.28	0.45	174.34	204.88	95.00	193.00
G2	17.17	16.53	3.87	247.02	243.89	185.12	189.85	0.23	0.29	161.07	196.50	69.00	151.00
G3	19.17	17.01	3.92	256.26	246.25	194.29	204.20	0.21	0.24	180.02	211.46	33.00	195.00
G4	18.01	14.32	3.32	250.95	232.49	186.83	181.22	0.24	0.30	173.63	198.04	73.00	145.00
G5	18.87	16.42	3.25	254.89	243.36	171.98	186.22	0.10	0.15	133.23	165.21	11.00	147.00
G6	18.30	16.44	5.45	252.31	243.47	199.41	230.25	0.20	0.26	207.56	218.86	53.00	163.00
G7	10.62	9.97	2.26	210.45	206.05	156.00	177.20	0.17	0.24	157.81	170.98	3.00	169.00
G8	18.77	16.31	2.19	254.44	242.80	185.69	185.43	0.21	0.23	179.20	170.20	3.00	213.00
G9	11.48	11.09	3.73	216.02	213.53	165.72	187.36	0.26	0.29	149.82	189.77	107.00	167.00
G10	13.64	11.53	2.42	228.79	216.28	195.80	188.50	0.29	0.33	192.61	210.10	5.00	177.00
G11	13.86	11.69	4.13	229.99	217.28	176.79	179.60	0.21	0.31	161.80	181.72	77.00	143.00
G12	14.28	13.23	3.94	232.29	226.48	173.65	175.19	0.22	0.22	156.10	178.91	-19.00	161.00
G13	11.68	11.69	2.17	217.21	217.28	142.84	153.44	0.10	0.21	145.29	152.09	17.00	133.00
G14	14.98	12.15	3.53	236.02	220.14	206.92	225.66	0.30	0.38	220.32	231.47	27.00	211.00
G15	11.81	11.22	3.57	218.06	214.32	155.14	170.19	0.17	0.20	134.23	174.81	21.00	155.00
G16	12.22	12.69	2.94	220.56	223.31	175.39	175.54	0.30	0.33	160.41	169.31	61.00	171.00
G17	12.55	11.69	3.74	222.48	217.28	188.81	198.05	0.32	0.43	179.49	203.64	69.00	191.00
G18	13.12	9.68	2.78	225.82	204.03	175.11	183.74	0.31	0.40	170.40	198.38	-35.00	173.00
G19	10.77	9.62	2.57	211.43	203.67	176.59	176.88	0.26	0.35	176.16	191.02	17.00	175.00
G20	11.06	10.58	3.36	213.30	210.16	171.74	184.52	0.28	0.38	158.01	189.52	61.00	143.00

continued...

Halo	M_{200}^{DMO} ($10^{11} M_{\odot}$)	M_{200}^{hydro} ($10^{11} M_{\odot}$)	M_{*}^{hydro} ($10^{10} M_{\odot}$)	R_{200}^{DMO} (kpc)	R_{200}^{hydro} (kpc)	$v_{\text{circ,max}}^{\text{DMO}}$ (km s^{-1})	$v_{\text{circ,max}}^{\text{hydro}}$ (km s^{-1})	ρ_0^{DMO} (GeV cm^{-3})	ρ_0^{hydro} (GeV cm^{-3})	v_0^{DMO} (km s^{-1})	v_0^{hydro} (km s^{-1})	$v_{\phi,\text{peak,DM}}^{\text{hydro}}$ (km s^{-1})	$v_{\phi,\text{peak,stars}}^{\text{hydro}}$ (km s^{-1})
G21	12.17	10.11	1.75	220.23	207.06	169.32	160.90	0.27	0.27	165.48	175.84	-7.00	107.00
G22	11.81	10.08	2.87	218.03	206.84	177.64	178.89	0.19	0.29	180.56	204.54	65.00	171.00
G23	11.11	9.95	2.87	213.62	205.93	167.66	196.69	0.26	0.34	157.81	195.58	1.00	187.00
G24	11.15	10.29	3.63	213.90	208.28	165.04	185.29	0.17	0.31	167.51	199.75	-33.00	187.00
G25	9.25	9.12	2.58	200.97	200.02	166.99	171.76	0.34	0.34	148.95	170.49	57.00	169.00
G26	10.32	8.96	3.53	208.43	198.86	173.33	195.18	0.23	0.35	175.87	203.86	33.00	183.00
G27	8.48	7.96	2.57	195.27	191.18	149.06	159.55	0.18	0.30	150.74	169.26	9.00	153.00
G28	8.09	7.67	2.39	192.21	188.83	137.26	165.97	0.15	0.24	140.91	167.33	-3.00	157.00
G29	9.99	8.82	3.11	206.18	197.87	168.53	210.45	0.29	0.41	170.61	201.80	1.00	201.00
G30	9.29	8.08	2.69	201.26	192.16	168.58	171.58	0.27	0.33	167.90	193.31	37.00	163.00
G31	8.73	8.32	2.09	197.14	193.99	153.77	160.32	0.31	0.32	145.25	158.02	55.00	141.00
G32	7.93	7.88	2.51	190.94	190.51	150.29	155.27	0.18	0.23	141.24	162.24	7.00	151.00
G33	9.15	7.80	2.64	200.27	189.93	158.48	163.05	0.29	0.32	141.62	165.70	19.00	139.00
G34	8.76	7.89	2.85	197.34	190.65	170.13	183.40	0.32	0.45	162.64	181.81	-11.00	181.00
G35	7.99	6.82	1.91	191.42	181.57	160.06	164.13	0.27	0.35	163.69	178.41	15.00	155.00
G36	38.57	36.36	4.49	323.49	317.19	219.36	214.47	0.13	0.18	249.83	237.47	19.00	181.00
G37	8.44	6.66	1.76	194.95	180.11	161.56	162.61	0.32	0.36	155.79	167.95	-5.00	143.00
G38	8.17	7.14	2.97	192.86	184.35	157.22	175.70	0.25	0.48	150.58	173.85	61.00	171.00
G39	8.50	7.48	1.88	195.37	187.24	167.63	165.57	0.38	0.39	168.29	175.31	21.00	149.00
G40	8.03	7.57	2.02	191.75	187.99	132.99	154.89	0.17	0.26	116.82	160.30	13.00	147.00
G41	8.12	6.89	1.94	192.40	182.18	166.01	161.58	0.35	0.41	158.66	158.51	101.00	139.00
G42	8.22	7.18	2.31	193.26	184.68	164.77	174.25	0.34	0.39	157.90	186.80	51.00	171.00

Four examples of halos from the sample used in this study are shown in Fig. 2.1, displaying the present-day, projected DM density fields in the DMO halos and in the matched halos in the hydro simulations, alongside stellar density maps of the same systems as viewed edge-on to the disc components.

2.2.1.1 Specifying simulated ‘solar neighbourhoods’

When analysing the simulations, we adopt a ‘Galactic’ coordinate system. Velocities are expressed with respect to the centre of mass velocity of the halo, and the halo centre is chosen to be the centre of potential (i.e., the location of the most bound particle). For the hydro simulations, the stellar discs are identified with the kinematical method outlined in Font et al. (2020). For each Milky Way-mass galaxy, the z axis is chosen to lie along the direction of the total angular momentum of stellar particles in the inner 20 kpc region of each system. The x and y axes are therefore in the plane of the stellar disc. For consistency, we use the same system of reference for the DMO halos (which have no stellar discs) as determined in their matched hydro counterparts.

With a reference frame established, we select ‘solar neighbourhood’ regions for each simulation. Given that the simulated sample covers a range in virial masses and radii (with radii ranging from $R_{200,\text{crit}} \approx 180 - 250$ kpc, see Table 2.1), and because the stellar discs differ in terms of their scalelengths, we take ‘solar radius’ in each simulation to be a fixed fraction of $R_{200,\text{crit}}$, specifically $R_0 = 0.04 R_{200,\text{crit}}$ for each system. This compares well with the scaling of R_0/R_{200} for the Milky Way, which has an estimated virial radius, $R_{200,\text{crit}}$, between 168.7 – 283.4 kpc and an estimated solar Galactocentric radius, R_\odot , between 7.10 – 8.92 kpc (for both, see Bland-Hawthorn & Gerhard (2016) and references therein), the measurements for the latter showing considerable scatter around the ‘standard’ value of 8.5 kpc. Furthermore, we consider the solar neighbourhood to be a cylindrical shell with a radial distance of R_0 , a fixed width of 1 kpc and a fixed height of 1.5 kpc. (We have investigated that changing the width or height of the ‘solar neighbourhood’ region or adopting a fixed distance, e.g., $R_0 = 8.5$ kpc does not significantly change our results).

With these parameters, the cylindrical shells contain a substantial number of DM particles, ranging from $\approx 8,800 - 22,500$ for the hydro simulations and between $\approx 5,400 - 18,000$ in the DMO simulations. (The larger number of DM particles in the hydro simulation is due to adiabatic contraction of the DM due to the presence of the baryons, as we discuss later.)

2.2.2 Standard Halo Model

The SHM (Drukier et al., 1986b) is routinely used in the modelling of data from direct detection experiments, or in making predictions for such detections. The model assumes a simple spherically-symmetric DM profile (usually either an isothermal or a Navarro-Frenk-White profile (Navarro et al., 1997)) corresponding to a halo with a total mass equal to that of the Milky Way. This model leads to a Maxwell-Boltzmann distribution of velocities for DM particles in the Galactic frame, $f(\vec{v})$, which, in order to account for the finite size of the halo, is truncated at the escape velocity:

$$f(\vec{v}) = \frac{1}{(2\pi\sigma_v^2)^{3/2}N_{\text{esc}}} \exp\left(-\frac{|\vec{v}|^2}{2\sigma_v^2}\right) \Theta(v_{\text{esc}} - |\vec{v}|), \quad (2.1)$$

where σ_v is the velocity dispersion of the DM, which is related to the most probable DM velocity (taken to be the local circular velocity), v_0 , via $\sigma_v = v_0/\sqrt{2}$, and Θ is the Heaviside function that truncates the distribution. As the integral over the velocity dispersion needs to be unity for the calculation of the scattering rates (see below), the Maxwellian must be renormalised to account for the truncation via the parameter N_{esc} , defined as:

$$N_{\text{esc}} = \text{erf}(z) - 2z \exp(-z^2)/\pi^{1/2}, \quad (2.2)$$

where $\text{erf}()$ is the error function and $z = v_{\text{esc}}/v_0$.

In practice, we truncate the Maxwellian function based on certain conditions of the WIMP velocities (Lewin & Smith, 1996):

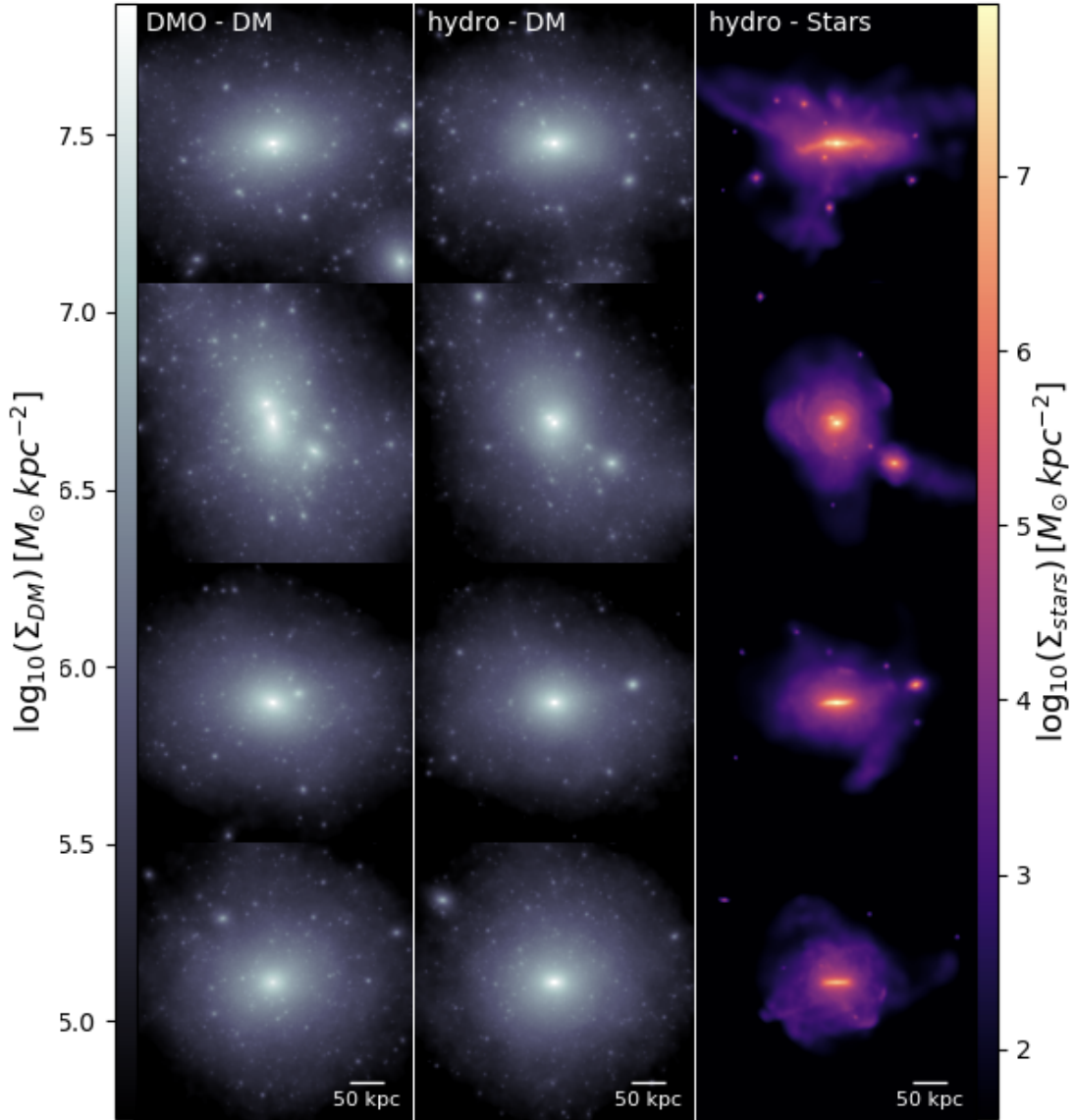


FIGURE 2.1: *Left column:* The projected density field of DM in the DMO simulations for Milky Way-mass halos: G25, G28, G34, G38 (top to bottom). Numerous subhalos can be observed in these distributions. *Middle column:* The projected density field of DM for the same halos in the hydro simulations. *Right column:* The edge-on projected density field of the star particles in the same four galaxies in the hydro simulations. A variety of stellar streams can be seen in addition to gravitationally bound satellite galaxies.

$$\int_{v_{\min}}^{v_{\max}} \frac{f(\vec{v})}{v} = \begin{cases} \frac{1}{v_0 y} & \text{if } z < y, x < |y - z| \\ \frac{1}{2N_{\text{esc}} v_0 y} \left[\text{erf}(x + y) - \text{erf}(x - y) - \frac{4}{\sqrt{\pi}} y e^{-z^2} \right] & \text{if } z > y, x < |y - z| \\ \frac{1}{2N_{\text{esc}} v_0 y} \left[\text{erf}(z) - \text{erf}(x - y) - \frac{2}{\sqrt{\pi}} (y + z - x) e^{-z^2} \right] & \text{if } |y - z| < x < y + z \end{cases} \quad (2.3)$$

where $x = v_{\min}/v_0$, $y = |V_E|/v_0$ (where $|V_E|$ is the velocity of the detector frame within the halo frame), and z is as defined above. Note that the first condition of the integral is not achievable in practice, as for this to be the case the Earth's velocity would have to be greater than the escape velocity. It is only included here for completeness.

To fully specify the truncated Maxwellian above, only two parameters are required: v_0 and v_{esc} . For v_0 it is standard practice to adopt the rotational speed of the Sun around the centre of the Milky Way (typically assumed to be 220 km s^{-1}), assuming it reflects the local circular velocity of the Galaxy. However, the observational values for the latter vary, and a more recently revised value is $238 \pm 15 \text{ km s}^{-1}$ (Bland-Hawthorn & Gerhard, 2016).

Estimates of the escape speed come from measurements of high-velocity stars in the solar neighborhood. Several experiments, including LZ and XENON1T (Akerib et al., 2020; Aprile et al., 2018), use a value of $v_{\text{esc}} = 544 \text{ km s}^{-1}$. As discussed by Evans et al. (2019), this value is based on an earlier measurement from the RAVE survey that used only 12 high velocity stars. Using a slightly larger sample of stars from the same survey, Piffi et al. (2013) obtain a value of $533_{-41}^{+54} \text{ km s}^{-1}$. More recently, this value has been revised using data from the *Gaia* survey. While, initially, this has led to a higher value, of $580 \pm 63 \text{ km s}^{-1}$ (Monari et al., 2018), a subsequent analysis has obtained $528_{-25}^{+24} \text{ km s}^{-1}$ (Deason et al., 2019).

In addition to a velocity distribution, the local DM density is required to compute the expected scattering rates. Estimates of the local WIMP density come from a range of sources, including the use of local dynamical estimates applied to stars in the solar neighbourhood, which must make assumptions about the geometry and state of equilibrium of the underlying DM component. Typically, the local DM density is taken to be

$\rho_0 = 0.3 \text{ GeV cm}^{-3}$ (Green, 2017; Read, 2014). However, recent observational results from stellar kinematics, stellar density profiles, maser observations and gas velocities suggest that a larger range of values of $\rho_0 \sim 0.45 - 0.70 \text{ GeV cm}^{-3}$ may be more appropriate (Smith et al., 2012; Bienaymé et al., 2014; Sivertsson et al., 2018; Hagen & Helmi, 2018; Piffil et al., 2014). Predictions for ρ_0 from cosmological simulations, as we produce here, will depend on the assumed mass of the Milky Way, for which measurements still have relatively large uncertainties (Bland-Hawthorn & Gerhard, 2016). This uncertainty is, to an extent, incorporated in our analysis, as we select halos whose masses span the range of quoted values for the Milky Way.

Direct DM detection aims to measure the nuclear recoil of a SM particle as it interacts with a WIMP. The differential scattering rate of a WIMP-nuclei interaction depends on the local DM density and the velocity distribution and can be written as:

$$\frac{dR}{dE}(E, t) = \frac{\rho_0}{m_{\text{DM}} m_N} \int_{v_{\text{min}}}^{v_{\text{esc}}} v f_E(\vec{v}) \frac{d\sigma}{dE}(v, E) d^3\vec{v}, \quad (2.4)$$

where ρ_0 is the local DM density, m_{DM} and m_N are the DM and nuclei particle masses (respectively), v_{min} is the minimum velocity the particle requires to produce a detection at the recoil energy E , \vec{v} is the velocity vector of the DM particle relative to the Earth, $f_E(\vec{v})$ is the corresponding velocity distribution function, and $d\sigma/dE$ is the energy differential DM-nucleus scattering cross-section. The minimum velocity depends to the threshold recoil energy in the form:

$$v_{\text{min}} = \sqrt{\frac{Em_N}{2\mu_{\text{DM},N}^2}}, \quad (2.5)$$

where $\mu_{\text{DM},N} \equiv (m_{\text{DM}}m_N)/(m_{\text{DM}} + m_N)$ is the DM-nucleus reduced mass.

For our analysis, we use a simplified version of equation 2.4, specifically:

$$\frac{dR}{dE} = \frac{\rho_0\sigma_0}{2m_{\text{DM}}\mu_{\text{DM},N}^2} F(q)^2 \int_{v_{\text{min}}}^{v_{\text{esc}}} \frac{f(\vec{v})}{v} d^3v, \quad (2.6)$$

where σ_0 is the zero momentum interaction cross-section, $F(q)^2$ is the nuclear form factor (which is a measure of the scattering amplitude of an incoming particle of a signal atom) and $q \equiv \sqrt{2m_N E}$.

The spin-independent form factor is taken to be [Engel \(1991\)](#):

$$F(q)^2 = \left(\frac{3j_1(qr_n)}{qr_n} \right) e^{-q^2 s^2}, \quad (2.7)$$

where j_1 is the Bessel function (for which we use only the first order version; i.e., j_1), r_n is the reduced nucleon radius and s is the nucleon skin depth (~ 1 fm).

As can be inferred from eqns. [2.4](#) and [2.6](#), the DM-nucleon scattering rate is highly dependent on the assumed velocity distribution function and density of the DM. Below, we examine these quantities in the ARTEMIS simulations and how they are influenced by substructures, baryons, the presence of dark discs, as well as general halo-to-halo scatter (cosmic variance).

2.3 Local dark matter distributions in ARTEMIS

2.3.1 Local density and velocity distributions

[Fig. 2.2](#) shows the distribution of the local DM densities (averaged over the cylindrical shell), ρ_0 , versus the maximum circular velocities, $v_{\text{circ,max}}$, for all 42 Milky Way-mass systems. Blue-filled circles represent the values in the hydro simulations and red-filled squares, those in the DMO simulations. We also plot observational measurements of the local DM density in the Milky Way, shown as black triangles and their respective error bars ([Holmberg & Flynn, 2004](#); [Soubiran et al., 2008](#); [Moni Bidin et al., 2012](#); [Bovy & Tremaine, 2012](#); [Garbari et al., 2011, 2012](#); [Smith et al., 2012](#); [Zhang et al., 2013](#); [Bovy & Rix, 2013](#); [Bienaymé et al., 2014](#); [Piffl et al., 2014](#); [Hagen & Helmi, 2018](#); [Sivertsson et al., 2018](#)). The grey band shows the range of other ρ_0 measurements (see [Green \(2017\)](#) and references therein). These indicate that there is a still significant

uncertainty in the value of ρ_0 , due to the variety of observational methods and implicit assumptions in the modelling (Pato et al., 2010; Read, 2014). The errors are known to be dominated by systematic effects, as indicated by the scatter in these values being larger than the errors of individual measurements.

Overall, the ρ_0 values obtained from our simulations (both DMO and hydro) agree reasonably well with many of the observational constraints, which is reassuring given the very different method we have employed to estimate the density. Specifically, the median ρ_0 in the hydro simulations is 0.32 GeV cm^{-3} , with a full range of $0.15 - 0.48 \text{ GeV cm}^{-3}$, while in the DMO simulations the median is 0.26 GeV cm^{-3} with a range of $0.10 - 0.38 \text{ GeV cm}^{-3}$. The median values agree well with the most quoted value of 0.3 GeV cm^{-3} . Our simulations clearly disfavour the higher values found in some observations (i.e., $\rho_0 > 0.6 \text{ GeV cm}^{-3}$), even after when baryonic effects are taken into account.

Interestingly, we find that there are marked differences between the local DM densities in the hydro halos and their respective DMO counterparts. For clarity, the inset panel in Fig. 2.2 shows a zoom into the ρ_0 and $v_{\text{circ,max}}$ values, with the arrows showing the direction of the changes between the DMO and hydro simulations. Generally, both ρ_0 and $v_{\text{circ,max}}$ increase for the same halo in the presence of baryons, which is due to the adiabatic contraction of the DM halo in response to the baryons (Blumenthal et al., 1986; Gnedin et al., 2004). This implies that the DMO simulations do not capture all the important physical processes necessary for predicting ρ_0 or $v_{\text{circ,max}}$, and that hydrodynamical simulations are better suited for this task (so long as the stellar mass distributions are realistic, as in ARTEMIS). We investigate the impact that these effects have on DM detection limits in Section 2.5.2.

Fig. 2.3 shows the local DM velocity distributions in our simulations (DMO in the left panel and hydro in the right). The solid black curves show the medians of the local DM $f(|v|)$ while the dark and light blue contours enclose 68% and 95% of the velocity distributions for all the halos. Owing to the high resolution of our simulations,

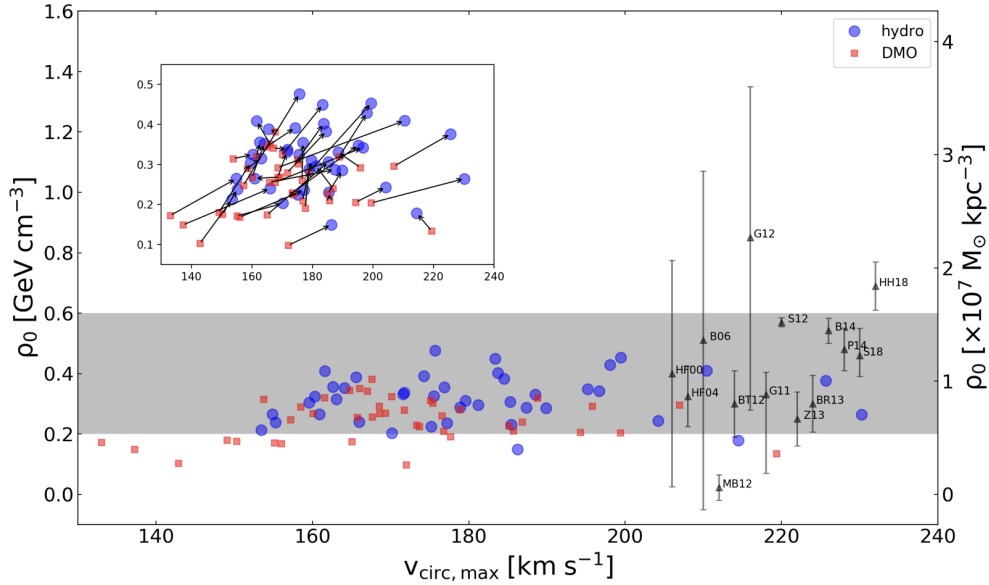


FIGURE 2.2: The local DM density, ρ_0 versus maximum circular velocity, $v_{\text{circ,max}}$, for the halos in the hydro (blue-filled circles) and DMO (red-filled squares) simulations. The black triangles represent local measurements of ρ_0 and associated errors (see text for details; points have been shifted in $v_{\text{circ,max}}$ around the 220 km s^{-1} value, for readability). The grey band represents the range of additional estimates of ρ_0 from [Green \(2017\)](#). *Inset panel:* A zoom-in on the ρ_0 versus $v_{\text{circ,max}}$ plot for the simulated systems. The arrows show the shift in the $(\rho_0, v_{\text{circ,max}})$ values from the DMO halos to their matched hydro counterparts.

the simulated solar neighbourhood regions contain a relatively large number of DM particles. This allows us to use small bins in velocity³, of 10 km s^{-1} .

To investigate how well the velocity distributions are fitted by a Maxwellian function, we fit all individual distributions with this function, by allowing the peak velocity, v_0 , to be a free parameter. The medians of the best fits for both simulation sets are shown in Fig. 2.3 with red solid curves and the peak of each best fit is indicated by a dashed line. For comparison, we also show the velocity distribution corresponding to the SHM model (green lines) with $v_0 = 220 \text{ km/s}$. The lower sub-panels show the residuals between the median local DM distribution from the simulations and the median best-fitting functions.

³We have experimented with various bin sizes and found that the overall shapes of the distribution functions do not change significantly. For significantly smaller bin widths, though, the data become noisier, while for much large values the occasional distinct features in the distribution can be washed out.

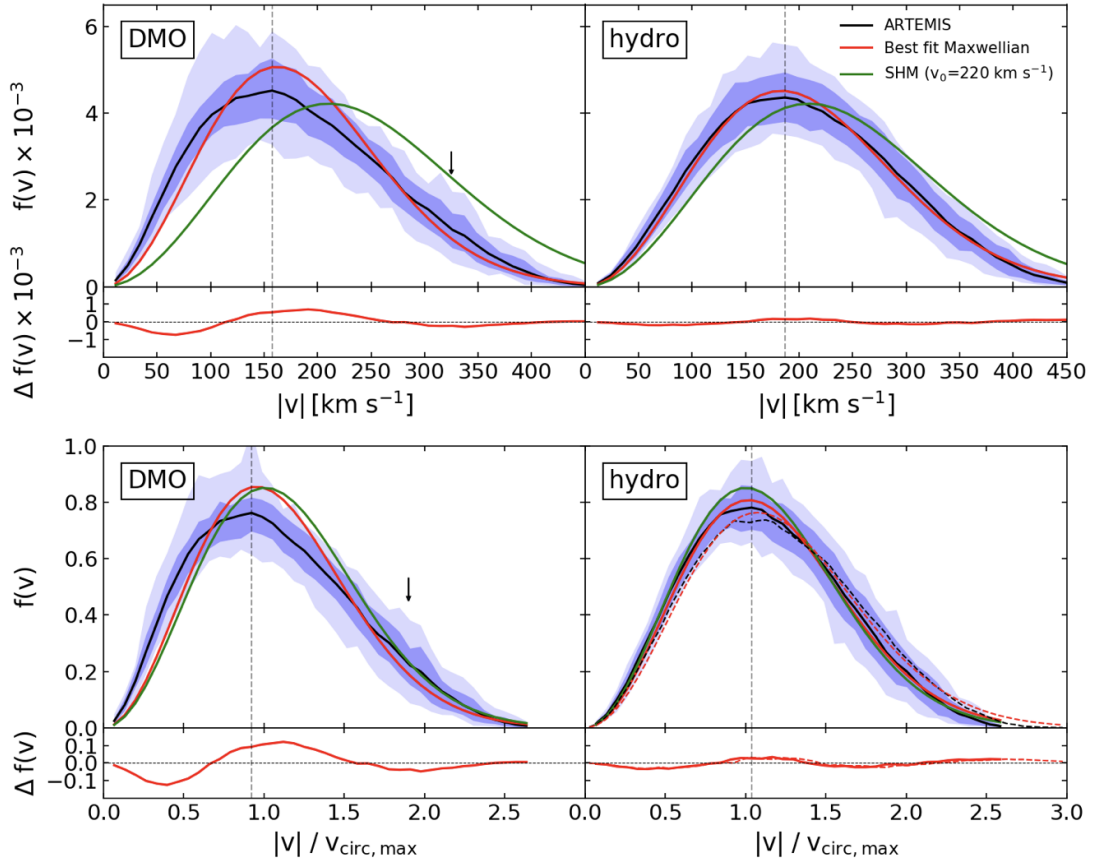


FIGURE 2.3: *Top*: DM velocity modulus distributions in the rest frame of the galaxy. The solid black curve represents the median of the velocity modulus distributions for the DMO (left) and hydro (right) simulations. The solid red curve represents the median of the best fitting Maxwellian distributions. The dark and light blue contours enclose 68% and 95% of the velocity distribution from all halos. The solid green line represents the velocity distribution determined by the Standard Halo Model with a peak velocity of $v_0 = 220 \text{ km s}^{-1}$. The lower panels show the residuals between the median distribution of the halos and the median Maxwellian fit. The black arrow points to the high-velocity feature discussed in Section 2.3.2. *Bottom*: Same as above, but for the DM velocity modulus distributions in the rest frame of each galaxy, normalised by their respective maximum rotational velocities, $v_{\text{circ,max}}$. The dashed black curve shows the median velocity modulus distribution for the hydro halos normalised by $v_{\text{circ,max}}$ of the matched DMO halos. The red dashed curve is the median of the best fitting Maxwellian distributions for the DMO normalised velocity distributions.

Fig. 2.4 shows the individual velocity distribution functions for the DMO (left panel) and hydro (right panel) cases. The error bars show the Poisson errors for a representative halo. The bottom panels show the difference of the best-fit Maxwellian with respect to the true velocity distribution function for that halo. Table 2.2 shows the reduced chi-squared values of the Maxwellian fit for all halos in the DMO and hydro cases. For an individual halo deviations from the best-fit Maxwellian can occasionally exceed tens of

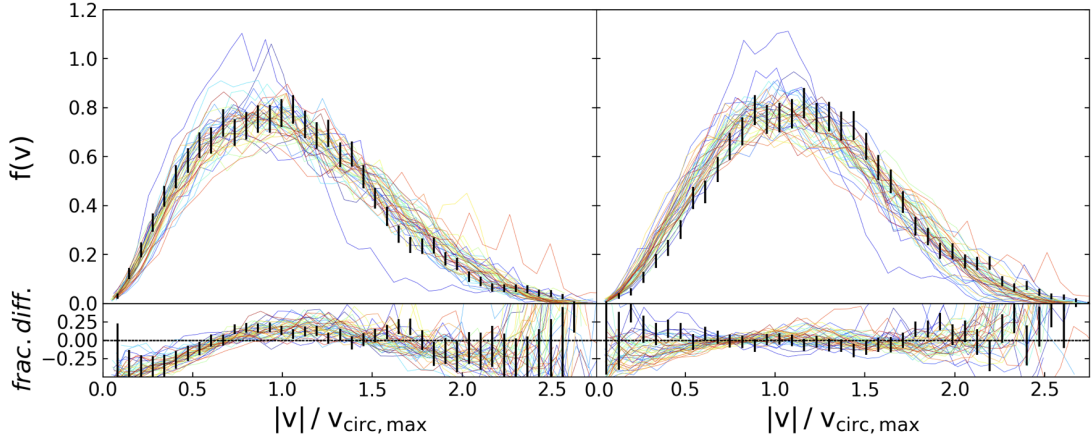


FIGURE 2.4: *Left*: Local DM velocity modulus distributions in the rest frame of the galaxy, normalised by their respective maximum circular velocity, $v_{\text{circ,max}}$. Coloured lines represent individual local velocity modulus distributions for all of the DMO halos. The black lines represent the 1σ Poisson error for a single halo. The lower panel shows the fractional difference between the individual distributions and their best fit Maxwellian. *Right*: Same as above but for the hydro halos.

TABLE 2.2: The goodness of fit values of the Maxwellian velocity distributions for all halos in the DMO and hydro cases ($\chi_v^2 \text{ DMO}$ and $\chi_v^2 \text{ hydro}$, respectively).

Halo	$\chi_v^2 \text{ DMO}$	$\chi_v^2 \text{ hydro}$	Halo	$\chi_v^2 \text{ DMO}$	$\chi_v^2 \text{ hydro}$
G1	7.07	1.07	G22	10.35	2.76
G2	4.76	1.63	G23	4.37	1.32
G3	5.44	1.95	G24	5.76	0.93
G4	4.17	0.75	G25	3.82	0.66
G5	36.51	5.44	G26	4.62	1.59
G6	7.30	0.92	G27	8.29	3.45
G7	1.83	3.07	G28	11.76	2.18
G8	4.59	2.72	G29	3.55	2.14
G9	3.47	3.40	G30	9.63	2.05
G10	4.74	2.18	G31	3.67	0.62
G11	3.62	0.71	G32	2.51	1.81
G12	4.64	1.43	G33	3.59	0.88
G13	1.71	1.50	G34	5.09	3.70
G14	1.89	1.78	G35	4.17	2.79
G15	10.37	1.75	G36	5.77	4.56
G16	2.61	0.46	G37	2.79	1.57
G17	3.33	0.71	G38	1.22	0.97
G18	3.50	1.23	G39	4.10	2.17
G19	2.13	1.94	G40	10.75	1.72
G20	5.88	1.08	G41	4.12	0.84
G21	3.98	0.70	G42	4.21	1.61

percent in a given velocity bin (greatly exceeding the random error).

Overall, we find that the local DM velocity distributions in the DMO simulations are poorly described by a Maxwellian, with significant differences from this function being seen across the whole velocity range. In contrast, the local distributions in the hydro simulations are relatively well described by a Maxwellian, although slight discrepancies are usually seen near the peaks. We will explore the impact of deviations from a Maxwellian distribution on DM direct detection limits in Section 2.5. The lower panels of Fig. 2.3 show the same velocity distribution as described above but now normalised by the maximum circular velocity of the halos, $v_{\text{circ,max}}$. Normalising by $v_{\text{circ,max}}$ removes the mass dependence on the halos velocity distribution, narrowing the overall distribution, although the same conclusions as above can still be made.

In both the DMO and hydro simulations, we observe considerable halo-to-halo variation, with the largest variation seen around the peaks of the distributions. Additionally, the velocity distributions contain stochastic components that are more prevalent at high velocities. These are seen in both sets of simulations, but they are more prominent in the DMO case due to the fact that substructures survive longer in the absence of a massive stellar disc (as discussed below). The averaged DMO velocity distribution also shows a noticeable ‘bump’ at the high-velocity tail, specifically at $v \sim 300 \text{ km s}^{-1}$. This feature will be explored further in Section 2.3.2, in the context of substructure.

The majority of our halos in both the hydro and DMO simulations have peak velocities less than the value assumed in SHM, i.e. $v_0 < v_{0,\text{SHM}} = 220 \text{ km s}^{-1}$. This is because, as discussed in Section 2.2.1, both the virial masses and the stellar masses of our simulated halos are somewhat on the lower mass ends of the accepted ranges for the Milky Way. (Also, the Milky Way has a higher stellar mass than typical galaxies in its halo mass range, suggesting that the impact of adiabatic contraction on the density and velocity may be somewhat larger in the Milky Way than typical for this halo mass.) Specifically, the median peak in the local velocity distribution for DMO simulations is 161.4 km s^{-1} , with a full range between $116.8 - 249.8 \text{ km s}^{-1}$, while for the hydro simulations the median peak is at 181.8 km s^{-1} , with a range between $152.1 - 237.5 \text{ km s}^{-1}$. The general trend of the increase in v_0 from DMO to hydro simulations can be understood

in terms of baryons deepening the potential wells of the halos, thus causing the particles to move at higher speeds.

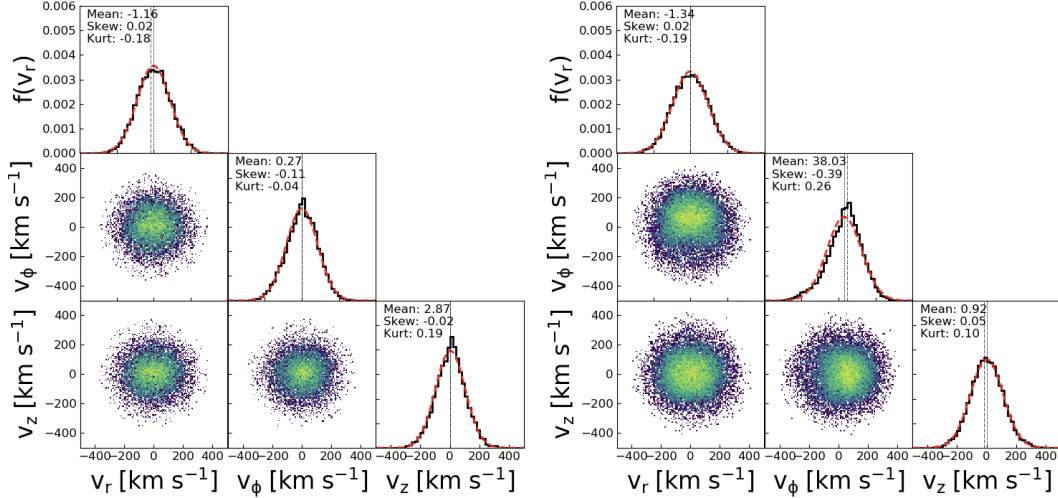


FIGURE 2.5: The distribution of velocities in the three components, (r, ϕ, z) for the solar neighbourhood of a typical halo (G38) in the DMO simulation. The black line histograms show the individual velocity components, $f(v_r)$, $f(v_\phi)$, and $f(v_z)$, and the red curves show the corresponding best-fit Gaussian functions. Alongside, we also plot the 2D velocity distributions (coloured by the density of the data points). The distribution statistics (mean, skewness and kurtosis) are shown in the upper-left of the plots. *Right*: Same as in the left panel, but now for the hydro simulation.

We also investigate the local distribution of DM velocities along the three cylindrical components, v_r , v_ϕ and v_z . Fig. 2.5 shows an example of the local velocity distribution components for one halo (G38), in both the DMO and hydro simulations. The local velocity distribution components are well fitted by Gaussian functions (red curves). Also, we find that the majority of DMO halos show similar distributions in their three velocity components. In the DMO simulations, the means of the v_r , v_ϕ and v_z components are all close to zero. However, in the hydro simulations, the means of the v_ϕ components show, occasionally, small positive values, indicating net rotation and the presence of ‘dark discs’. We will investigate this in more detail in Section 2.4.2.

Finally, we infer the escape velocities, v_{esc} , for the simulated local velocity distributions. Specifically, we calculate v_{esc} from the high-velocity tail of local halo star particles by following methods outlined by Piffi et al. (2013), and using:

$$f(v | v_{\text{esc}}, k) \propto (v_{\text{esc}} - v)^k, \quad (2.8)$$

for $v < v_{\text{esc}}$ and k a parameter constrained by Piffil et al. (2013) to be between $2.3 \leq k \leq 3.7$ from their set of cosmological simulations. Therefore, for our fits, we set $k = 3$ and allow v_{esc} to vary. The median v_{esc} for all our halos is 521.6 km s^{-1} and the full range is between $509.9 - 631.9 \text{ km s}^{-1}$. This is in good agreement with recent observational measurements from RAVE and, more recently, from *Gaia*.

In Section 2.5.1 we will investigate how the WIMP cross-sections calculated within the SHM formalism depend on various assumed values for ρ_0 , v_0 and v_{esc} , and in Section 2.5.2 we will incorporate in the calculations the full range of these values obtained in the simulations.

2.3.2 Impact of substructure

As mentioned in Section 2.3.1, the average DMO local velocity distribution (see Fig. 2.3) contains a peculiar feature at the high-velocity end. This feature can be seen in the 95% contour and can be attributed to at least two halos in our sample (G2 and G28). The velocity distributions of the solar neighbourhoods in these two systems are shown in Fig. 2.6. A prominent peak is seen in the high-velocity tail of each distribution (more so in G28), at $250 < |v| < 350 \text{ km s}^{-1}$, caused by the presence of DM substructure. Also, both distributions clearly deviate from a Maxwellian.

We investigate the velocity distributions for these two halos (again, in the DMO simulations) in more detail in Fig. 2.7, where we plot the distribution of the v_r , v_ϕ and v_z components in the respective solar neighbourhoods. This shows that the overlap of the secondary peaks in the $f(|v|)$ was only coincidental. The substructure in the G2 halo has a retrograde v_r , peaking at $v_r \approx -150 \text{ km s}^{-1}$, whereas in G28 it peaks at $v_r \approx 200 \text{ km s}^{-1}$. The density plots in velocity space show small clusters at $(v_r, v_\phi, v_z) \approx (-150, 0, -50) \text{ km s}^{-1}$ for G2 and at $(v_r, v_\phi, v_z) \approx (200, -150, -75) \text{ km s}^{-1}$ for G28. The 2D velocity plots indicate that local halos are anisotropic (see also the 2D plots in

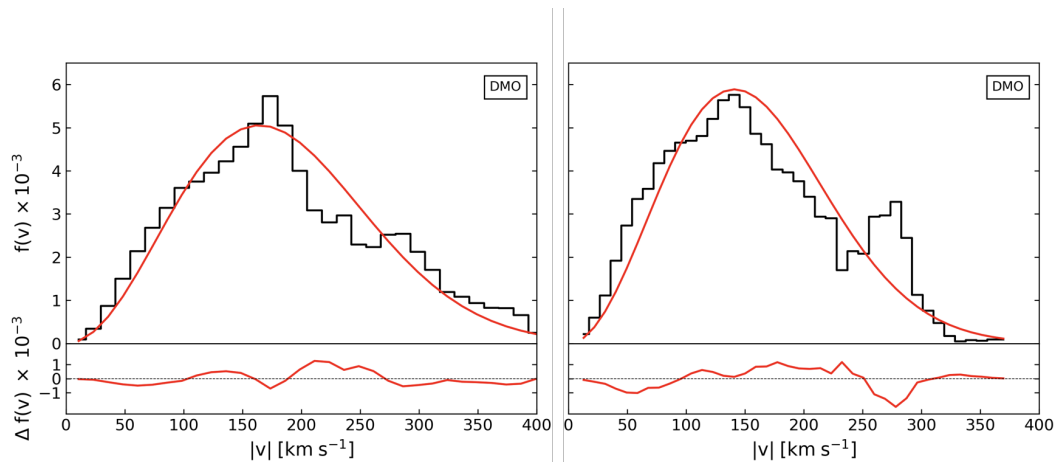


FIGURE 2.6: *Left panel:* DM $f(|v|)$ distribution in the rest frame of the G2 halo (with solid black histogram), which shows evidence of substructure in the solar neighbourhood (DMO simulations). The solid red curve represents the best fitting Maxwellian distribution. *Right panel:* shows the same distribution, now for halo G28. The lower panels show the residuals between $f(|v|)$ and the best fit Maxwellian function.

the Fig. 2.5). Deviations from gaussianity are seen in all the three components of the local velocity distributions for G28, near the location of the cluster. G2 shows a similar deviation at $v_r \approx -150 \text{ km s}^{-1}$.

Interestingly, we observe no separate velocity peaks in the hydro versions of the G2 and G28 systems, in their corresponding solar neighbourhoods. This suggests that some of the substructure seen in the DMO simulations may be erased in the presence of baryons. Previous hydrodynamical simulations have found that the number of DM subhalos in the inner regions can decrease by about 50% compared to DMO simulations, due to additional tidal disruption induced by the stellar galactic disc (e.g., [Sawala et al. \(2016\)](#); [Stafford et al. \(2020\)](#)). We find a similar result in our simulations (not shown here quantitatively, however the paucity of subhalos in the inner regions of galaxies is immediately apparent in comparing the left and middle columns of Fig. 2.1). This also suggests that using DMO simulations may occasionally overestimate the sensitivity to DM due to the relatively long-lived nature of substructure in DMO simulations compared to that in hydro simulations.

In principle, any DM substructure in the solar neighbourhood, either in the form of bound clumps or tidal streams, may lead to a boost in the DM signal, e.g. by inducing a step-like feature in the energy recoil spectrum ([Freese et al., 2005](#); [Green, 2001](#)), and

thus affect the direct DM detection limits. The strength of the signal depends not only on the mass in the DM substructure, but also on the direction of motion of the DM particles relative to the Earth (Kuhlen et al., 2010). Several tidal streams are known to pass through the solar neighbourhood. In addition to the Sagittarius stream, *Gaia* has revealed several other substructures (Gaia Collaboration et al., 2016, 2018). One of them is a tidal debris from a massive satellite galaxy that fell in ~ 10 Gyr ago, dubbed the *Gaia* sausage (Helmi et al., 2018). Other known streams include Nyx (Necib et al., 2020a,b) or the S1 and S2 streams (Myeong et al., 2018). The Sagittarius stream is likely to have a non-negligible contribution to the local DM distribution (Purcell et al., 2012), while *Gaia* sausage is expected to have a modest effect on the DM detection rates (Evans et al., 2019; Bozorgnia et al., 2020). The S1 stream can lead to an increase in the number of high energy nuclear recoils and a slight improvement of DM detection rates (O’Hare et al., 2018), particularly for directional experiments since this stream is retrograde. The S2 stream can also lead to multiple effects in the DM signal (O’Hare et al., 2020).

Although our simulations are not suited to model the observed streams in the Milky Way specifically, they do include the contribution of local DM substructures and so we can gauge, in a broader sense, the effect that this type of features may have on the direct detection limits (see Section 2.5.2). Generally, we find that substructures that are massive enough to increase the local DM detectability rates are not very common in our simulations, particularly in the hydro simulations where such features are efficiently erased by tidal forces.

2.4 Larger scale changes to the DM structure

We have seen that the inclusion of baryons generally results in an increase in both the local (solar neighbourhood) density and velocities of DM particles; a result of adiabatic contraction of the DM halos in response to the baryons. Here we explore further how this is achieved in practice, by examining the impact on the halo shape and the prevalence of dark discs.

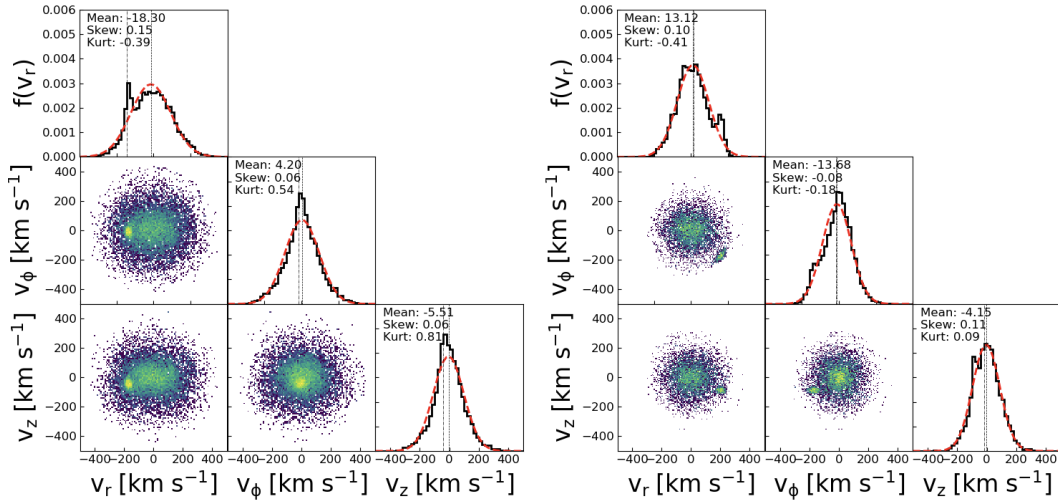


FIGURE 2.7: *Left*: The distribution of velocities in the three components, (r, ϕ, z) for the solar neighbourhood of the G2 halo in the DMO simulation. The black line histograms show the individual velocity components, $f(v_r)$, $f(v_\phi)$, and $f(v_z)$, and the red curves show the corresponding best-fit Gaussian functions. Alongside, we also plot the 2D velocity distributions (coloured by the density of the data points). The substructure in the local region is clearly seen as the peak in the v_r velocity distribution, as well as the 2D velocity plots. The distribution statistics (mean, skewness and kurtosis) are shown in the upper-left of the plots. *Right*: Same as in the left panel, but for the solar neighbourhood region of the G28 halo, in the DMO simulation. The substructure in the local region is clearly seen as peaks in the $f(v_r)$, $f(v_\phi)$ and $f(v_z)$ distributions, as well as high density regions in the 2D velocity plots.

2.4.1 DM halo shapes

Here we contrast the shapes of the simulated DM halos, between the DMO and hydro simulations. We determine the shapes of the simulated DM halos from the ratios of the principal axes, a (major), b (intermediate) and c (minor), which are calculated from the eigenvalues of the mass distribution tensor within an inner region of radius 30 kpc. The principal axes are used to calculate the DM halo sphericity, $S = c/a$ and DM halo triaxiality, $T = \frac{a^2 - b^2}{a^2 - c^2}$.

Fig. 2.8 shows the sphericity and triaxiality parameters for simulated halos used in this work for both the DMO and hydro cases. The hydro halos tend to be much more spherical ($S \rightarrow 1$) than the DMO halos, which is a well-known effect of the inclusion of baryons (Kazantzidis et al., 2004; Debattista et al., 2007; Tissera et al., 2010; Kazantzidis et al., 2010). This result is reassuring, as recent analysis of stellar halo

kinematics with *Gaia* DR2 suggests that the DM halo of the Milky Way is, at least in the inner region, nearly spherical (Wegg et al., 2019). The hydro halos also tend to be more oblate ($T \rightarrow 0$), in contrast to the prolate ($T \rightarrow 1$) distribution of the DMO halos. This is also expected, as the gas infall and the associated formation of a large-scale disc component can result in significant changes in the halo shapes (Gunn & Katz, 1991; Dubinski, 2002; Debattista et al., 2007).

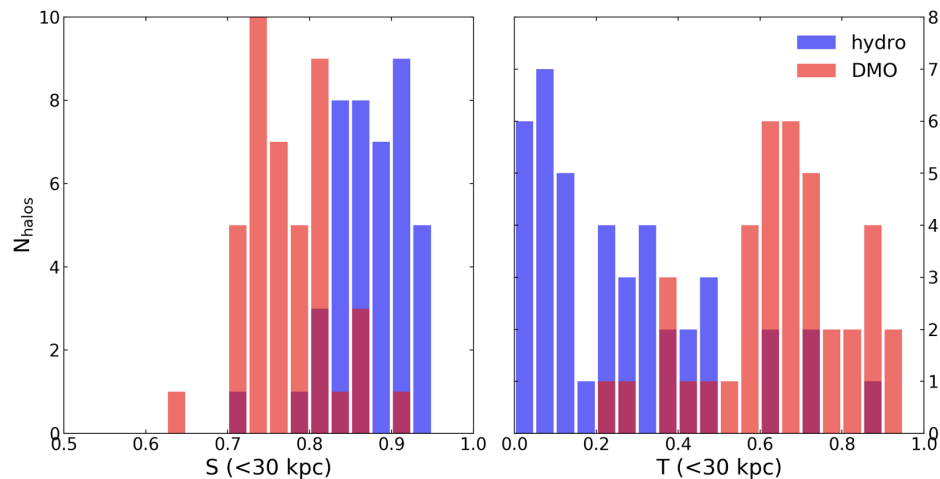


FIGURE 2.8: *Left*: Distribution of sphericity, S , of all Milky Way-mass halos in the hydro (blue) and DMO (red) cases, calculated for regions within 30 kpc of the galactic centre. *Right*: The distribution of the triaxiality, T , for all Milky Way-mass halos in the hydro and DMO cases, also calculated within 30 kpc. Baryonic processes lead to more spherical and less triaxial halos.

2.4.2 Probability of hosting a dark disc

One avenue for the formation of a dark disc is through the accretion of dwarf satellite galaxies and their subsequent tidal disruption in the Galaxy. The accreted dark disc is likely to be formed from tidal debris from satellites incoming on low-inclination orbits (Read et al., 2008). A stellar disc also drags the incoming satellites towards the disc plane where they are more easily torn apart by tides (Read et al., 2009). Alternatively (or in addition to), adiabatic contraction due to the stellar disc may also lead to the formation of a dark disc. The presence of a dark disc may have implications for direct detection of DM, as a low-velocity dark disc with respect to the Earth can increase the rate of detection at lower recoil energies (Bruch et al., 2009; Read et al., 2009).

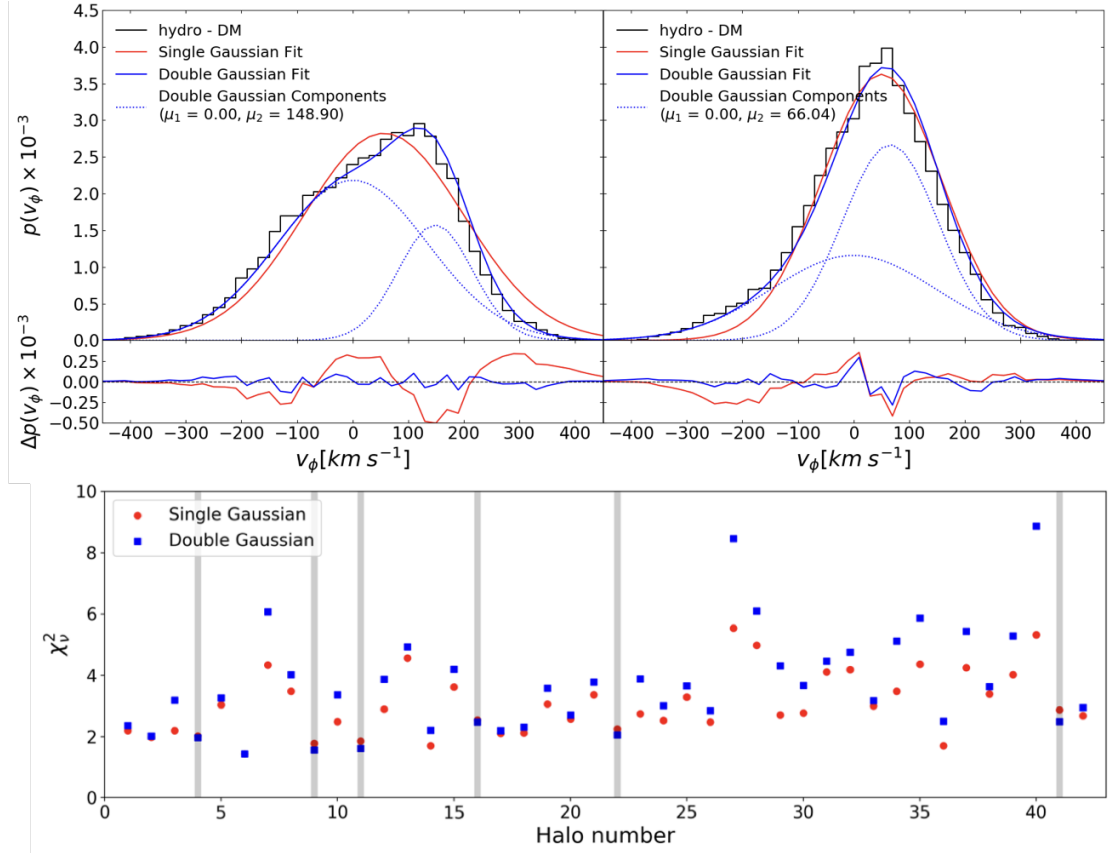


FIGURE 2.9: *Upper panels:* The azimuthal velocity DM distribution, v_ϕ for the G11 halo (left), which is the halo with the most prominent dark disc component in our sample, and for the G38 halo (right) in the hydro simulations. The black histogram shows the DM distribution from the simulations; the solid red curve shows the best-fitting Gaussian to the distribution; the solid blue curve shows the best-fitting double Gaussian, with the separate components shown as blue dashed curves. The difference between the fits is shown below the distributions. *Lower panel:* The reduced χ^2 values for all halos in the hydro simulations, comparing the goodness of fit between the single Gaussian fit and the v_ϕ DM distributions (red circles) and between double Gaussian fits and the v_ϕ DM distribution (blue squares), respectively. Most halos are better fitted by a single Gaussian. The six halos that are better fitted by a double Gaussian are highlighted with grey bands.

To quantify how often dark discs occur in the ARTEMIS simulations, we first use the methodology of Schaller et al. (2016b); Ling et al. (2010), which identifies a dark disc when a double Gaussian better fits the local DM v_ϕ distribution than by a single Gaussian. The upper panels of Fig. 2.9 illustrate the v_ϕ distribution of DM in the solar neighbourhoods of two halos, G11 and G38 (black lines), with the best fits for single and double Gaussians shown with the solid red and blue lines, respectively. The components of the double Gaussian are also shown (with blue dashed lines). For the fitting, one Gaussian component is fixed at $v_\phi = 0$ km s⁻¹ (corresponding to the assumption

of a non-rotating DM halo), while the second is allowed to vary freely. The difference between the two fits and the v_ϕ distribution is shown below.

Halo G11 provides the strongest evidence for the existence for a dark disc among all halos in our sample. Its second component of the double Gaussian exhibits a large v_ϕ value centred around 148.9 km s^{-1} , indicating a significant prograde motion. In contrast, halo G38 prefers a single Gaussian fit, with the second component centred around $v_\phi \approx 66.0 \text{ km s}^{-1}$. Not unexpectedly, we find that dark discs are more prevalent in systems in which $f(|v|)$ deviates more strongly from a single Gaussian (or Maxwellian). Interestingly, all dark disc components are found to be co-rotating with the stellar disc.

The lower panel of Fig. 2.9 shows the prevalence of dark discs in the entire sample. The reduced χ^2 values for the single Gaussians are shown with red circles and those for double Gaussians with blue squares. For clarity, the grey columns highlight the halos that are better fitted by a double Gaussian. We find that in the majority of our halos, the v_ϕ distribution is better fitted by a single Gaussian. By a conservative estimate, this method retrieves that $\approx 14\%$ of halos (6 out of the 42 in our sample) contain a dark disc. Previous work investigating the existence of dark discs in Milky Way analogues in EAGLE found, with the same method, that only 1 out of 24 halos has a detectable dark disc (Schaller et al., 2016b). One possible explanation for why we find more dark discs in ARTEMIS than found in EAGLE is due to the higher stellar mass fractions in ARTEMIS, which are in better agreement with observations (Font et al., 2020) and which lead to enhanced adiabatic contraction (Stafford et al., 2020).

Fig. 2.9 also shows that, in some cases where the double Gaussian fit is preferred, the difference in χ^2 from a simple Gaussian is not sufficiently large to be conclusive. Nevertheless, these (and other) halos clearly exhibit non-Maxwellian velocity distributions and display significant net rotation. This suggests that the above method may not capture the existence of dark discs accurately enough.

Fig. 2.10 exemplifies this point with the G38 halo, which is better fitted by a simple Gaussian, yet it exhibits other indications that it contains a dark disc, for example in its DM halo shape and rotation characteristics. The top left panel shows the azimuthal velocity v_ϕ distribution of DM in the solar neighbourhood of this system, both in the

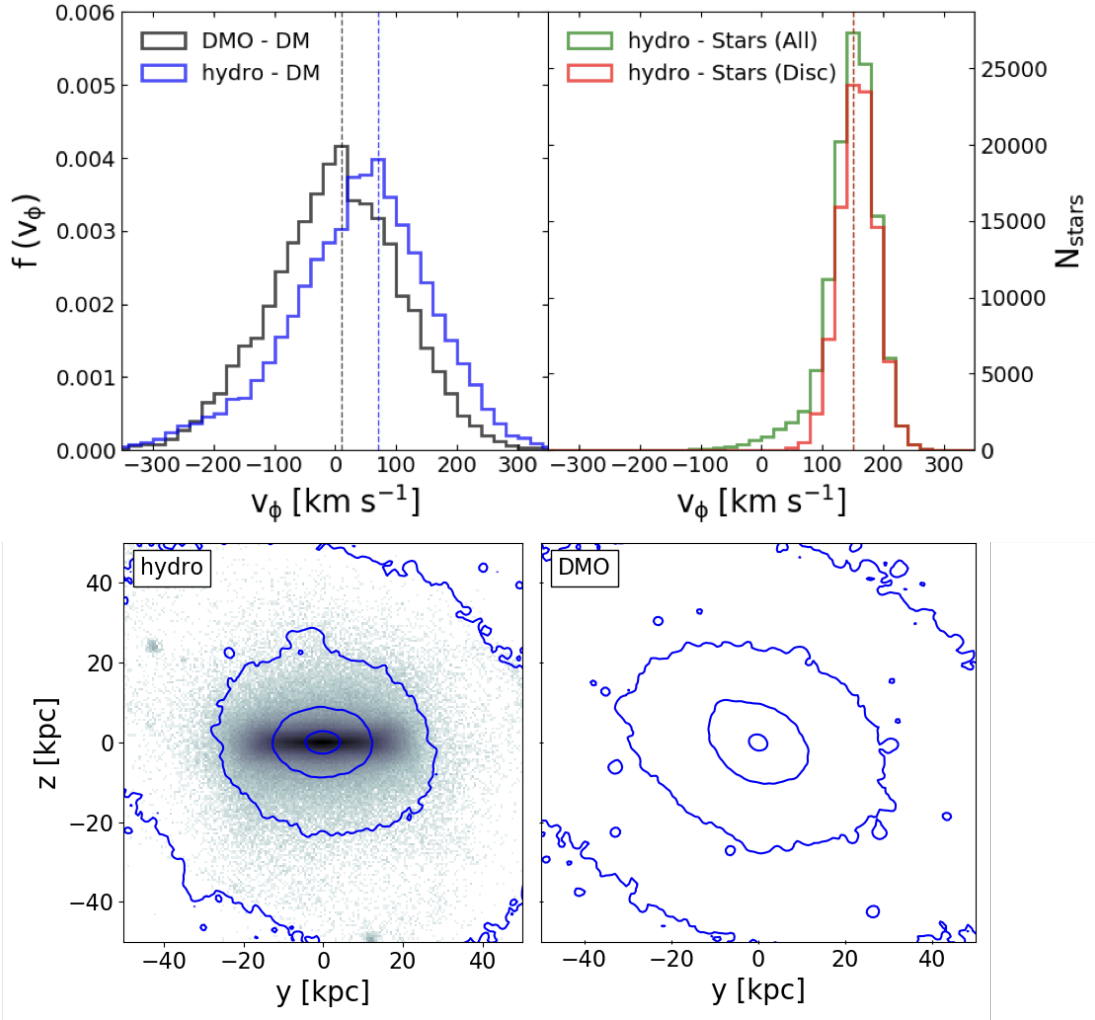


FIGURE 2.10: *Top row*: The local distribution of rotational velocities for the G38 halo. *Left*: The DM distributions for the DMO and hydro simulations are shown in black and blue, respectively. The dashed lines in their respective colours show the peaks of the distributions. *Right*: The stellar distributions for all stars and disc stars are shown in green and red, respectively. The dashed lines represent the peak velocity in the distributions. *Bottom row. Left*: The projected DM density contours for G38 in the hydro simulation. The underlying points show the distribution of the stellar component, with the disc clearly visible at the centre. *Right*: The projected DM density contours in the G38 system in the DMO simulation.

DMO and the hydro simulations. In the hydro case, the peak of the DM distribution is skewed towards that of the stars. The local stellar v_ϕ distributions are shown in the top right panel, for both all stars (green) and the disc (red). The local DM component co-rotates with the stellar disc, with a peak $v_\phi \approx 75 \text{ km s}^{-1}$, which is roughly half of that of the stellar disc in this galaxy. The bottom row in Fig. 2.10 shows, with contour lines, the DM distribution in this galaxy in the presence and absence of baryonic effects. The introduction of baryons into the simulations causes the central region of the DM halo to become oblate and aligned with the stellar disc, the latter being shown as a background stellar particle density (for a similar result, see also Read (2014)). Taken together, the oblate shape of the DM component and its prograde rotation suggest that this system contains a dark disc. Note however that the evidence indicates that the local DM rotates as a whole (which is also supported by the fact that the $f(|v|)$ prefers a single Gaussian rather than two). This suggests that, in this case, the DM halo has acquired its rotation due to the presence of baryons. These can cool and form a rotationally-supported disc, thus causing a shift in the velocity distribution of DM.

In order to identify other systems which are best fitted by single Gaussians, yet display dark disc characteristics, we further investigate the distribution of the peak azimuthal velocities in all halos. This is shown in the left panel of Fig. 2.11, for both the hydro and DMO simulations. In the hydro simulations, there is a distinctive category of halos (15 in total) with significant prograde rotation of their local DM component ($v_\phi > 50 \text{ km s}^{-1}$; the peak v_ϕ for DM and stars for all halos are shown in Table 2.1). All 6 halos found previously to contain dark discs via the double Gaussian fitting method are in this category. Note that, if one defines a dark disc as a separate rotating component with an overall non-rotating halo, then the other 10 halos would not, strictly speaking, qualify as dark discs. If, however, one also includes rotating, flattened DM halos (i.e., the whole inner halo is rotating, rather than two separate components) that are aligned with the stellar disc, then our work suggests that the fraction of Milky Way-mass galaxies with dark discs can be as high as $\approx 36\%$.

There is a marked difference in the rotation pattern of local DM components in the hydro versus DMO simulations in the sense that net prograde motions are conspicuously missing in the DMO simulations. Clearly, the baryonic effects (namely the adiabatic

contraction referred to earlier) play a role in the emergence of dark discs. The right panel of the same figure shows a (mild) anti-correlation between the triaxiality parameter T of galaxy systems in the hydro simulations and their peak v_ϕ . This suggests that systems that have the fastest prograde motion of their local DM components also tend to be more oblate.

As an additional test to quantify the importance of dark discs, we focus on the density enhancement that results. Specifically, we compute the following two metrics: i) the ratio of our fiducial cylindrical DM density estimate to one where the DM density is estimated using a spherical shell of the same radius and width as the cylinder, both from the hydro simulations; and ii) the ratio of the fiducial cylindrical DM density from the hydro simulations to a spherical shell-based estimate from the corresponding DMO halo. Note that the first metric will somewhat underestimate the importance of a dark disc, since the dark disc will also contribute to the spherical shell estimate. On the other hand, the second metric will somewhat overestimate the importance of a dark disc, since the DM density in the hydro simulation would be increased by normal (spherical) adiabatic contraction.

For the first metric we compute a mean ratio of 1.27 with a standard deviation (intrinsic scatter) of ± 0.20 . For the second metric we compute a mean ratio of 1.69 with a standard deviation of ± 0.34 . Thus, the presence of a dark disc increases the solar neighbourhood DM density by tens of percent, constituting a significance enhancement with respect to systems that do not possess such a structure.

2.5 Effects on DM direct detection limits

In the preceding sections, we have shown that there is significant halo-to-halo scatter in the solar neighbourhood DM density and velocity distributions and that baryons also play an important role in setting these quantities. Here we explore the impacts of the scatter and baryons on the DM direct detection limits using the simplified model outlined in Section [2.2.2](#).

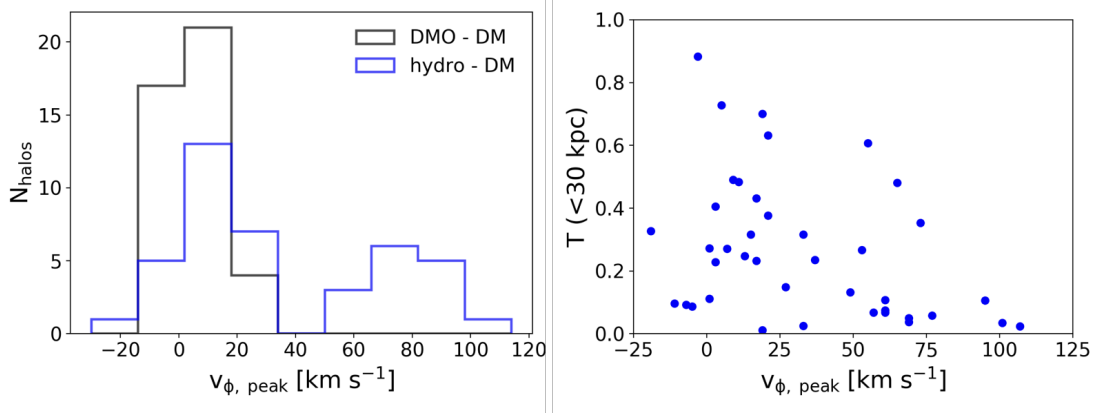


FIGURE 2.11: *Left:* Histograms of the peak azimuthal velocity DM distribution v_{ϕ} for the hydro (blue) and DMO (black) ARTEMIS halos. *Right:* The peak azimuthal velocity, v_{ϕ} versus triaxiality T within 30 kpc of the galactic centre for the hydro halos.

Specifically, we show the effects of incorporating the halo-to-halo scatter in the density and velocity distributions from ARTEMIS on the exclusion limits for the XENON1T and LZ experiments, in the spin-independent WIMP-nucleon cross-section–mass plane. Before doing so, however, we show the impact of systematically varying each of the SHM parameters on the detection limits, to build some intuition for the simulation-based results.

2.5.1 Exploring variations to the SHM

Direct detection experiments have set increasingly strong constraints on the cross-section of a WIMP-nucleon interaction under the assumption of the SHM, adopting fixed values for ρ_0 , v_0 and v_{esc} . However, as discussed in Section 2.2.2, there are significant variations in the measured values for these parameters. Also, as shown in Section 2.3.1, the simulations also show variations in these values. Here we show the effects of varying the astrophysical parameters on the determination of the WIMP-nucleon cross-section limits. For these calculations, we assume a generic Xenon detector with a 1000 kg per year exposure, zero observed events and 100% efficiency across recoil energies from 5 to 40 keV_{nr} .

The three panels in Fig. 2.12 show the results of varying the local DM density (upper), local DM peak velocity (middle) and escape velocity (lower), respectively, whilst

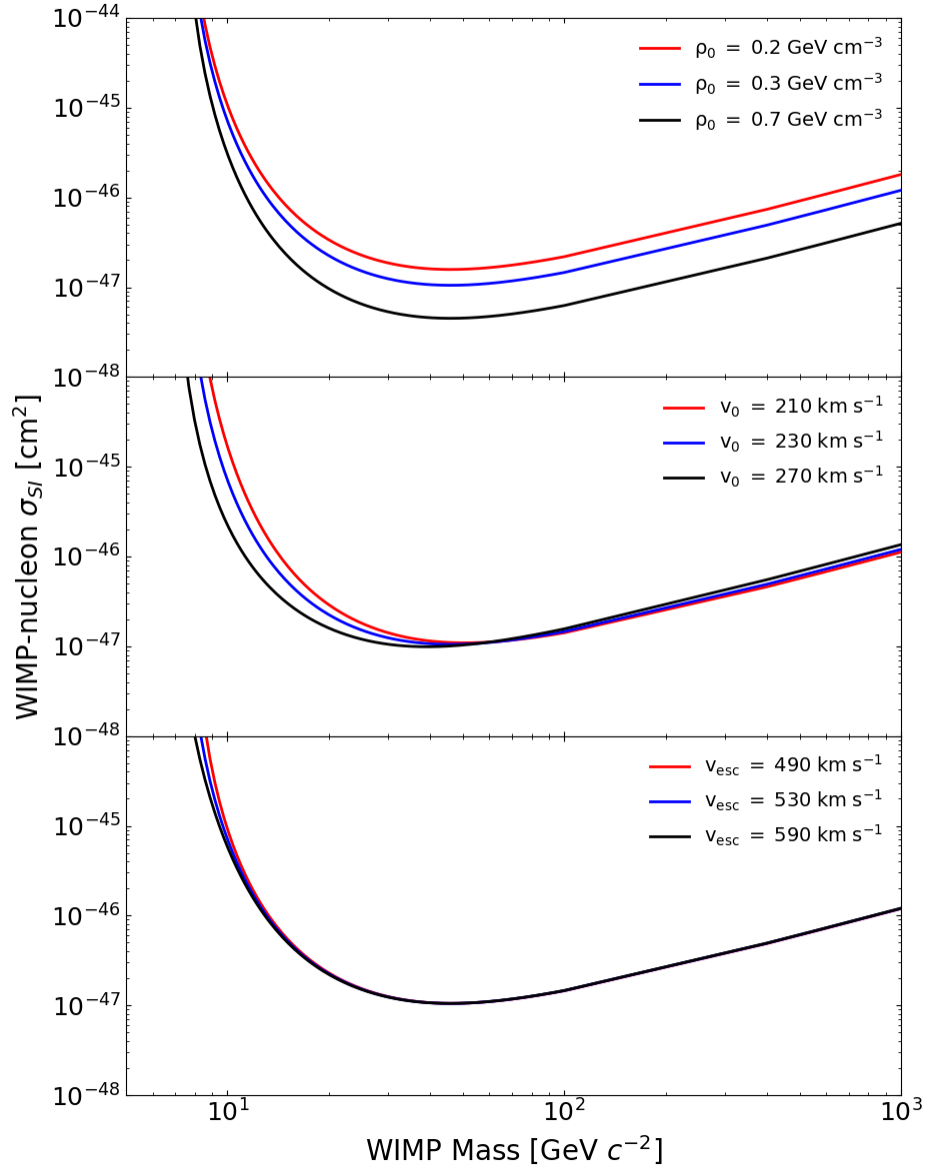


FIGURE 2.12: The 90% confidence level limits for a single halo with a Maxwellian distribution of local DM velocities, assuming SHM and varying ρ_0 , v_0 and v_{esc} independently (i.e. varying one parameter at a time, while keeping the other two fixed). The *upper* panel shows the variations in ρ_0 : 0.2, 0.3 and 0.7 GeV cm^{-3} , respectively; the *middle* panel shows the v_0 variations: 210, 230 and 270 km s^{-1} ; and the *lower* panel shows the variations in v_{esc} : 490, 530 and 590 km s^{-1} . In each panel, the blue lines represent (approximately) the typical values used in SHM models, while the red and black lines represent (approximately) the minimum and maximum ranges found in observations and/or simulations.

keeping the other parameters fixed. The range in which each parameter is chosen to cover (roughly) the current uncertainties in the observational measurements (see Section 2.2.2). The areas above the curves indicate the regions that direct detection experiments are sensitive to.

As can be seen from equation 2.6, the interaction rate and hence cross-section, directly scales with the local density of DM, in that a larger density gives rise to more scattering events and a stronger limit. Our model shows that the WIMP-nucleon cross-section can vary by half an order of magnitude when considering the plausible range of values for ρ_0 .

The combination of equations 2.5 and 2.6 reveals the dependence on the velocity model parameters v_0 and v_{esc} . This dependence is strongest at low DM masses where $m_{\text{DM}} \ll m_{\text{N}}$, and the minimum DM velocity required to produce detectable recoil energy is inversely proportional to the DM mass (see equation 2.5). When v_{min} is comparable to v_0 ($m_{\text{DM}} < \sim 40$ GeV), the changes in v_0 strongly affect the velocity integral in equation 2.6 and, as a result, the expected rate. When v_{min} is close to v_{esc} ($m_{\text{DM}} < \sim 10$ GeV) then the velocity integral becomes very constrained, and the changes in v_{esc} also strongly affect the expected rate of DM interactions with Xe nuclei.

2.5.2 Direct detection limits using ARTEMIS

In the following, we incorporate the local DM densities, local peak velocities (determined from the best-fitting Maxwellian distributions) and escape velocities measured directly from the simulations into the direct detection limits methodology. For this, we use experimental parameters of LZ and XENON1T experiments to better compare with the experimental results. We show results for both the DMO and hydro simulations with the aim of comparing the two and therefore to determine the importance of including baryonic physics in the predicted direct detection limits.

We note that our method does not incorporate a background model. However, this is unimportant for our purposes, as we are mostly interested in the *relative* effects of varying the velocity distribution function and DM density, as guided by the simulations.

When reproducing the expected limit of a specific detector, we consider the convolved detection and selection efficiencies. The efficiencies related to the recoil energy are included by interpolating the experimental nuclear recoil efficiencies (Akerib et al., 2020; Aprile et al., 2018). To further ease the comparison, the variations between the experimental and simplified models are accounted for by scaling the calculated limit to the $100 \text{ GeV } c^{-2}$ experimental result.

2.5.2.1 Experimental corrections to the calculated exclusion limits

Data analysis and limit setting procedures used by the direct detection experiments involve many steps and detector knowledge which can not be fully replicated outside of the experiments. To make a comparison of the calculated and experimental limits meaningful, especially at low masses where the effect of the velocity model is strongest, we included the recoil energy-dependent efficiency published by the experiments into the calculation. This efficiency affects the shape of the exclusion limit curve through the dependence of the recoil energy on the mass of dark matter particle.

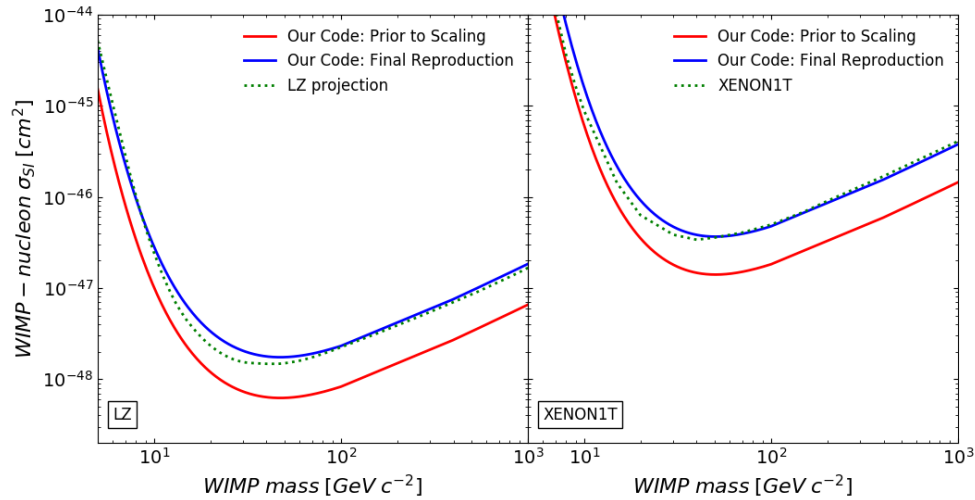


FIGURE 2.13: *Left*: The 90% confidence level limits for LZ parameters (Akerib et al., 2020). The median upper-limits are shown as red solid and blue solid lines for before and post scaling to $100 \text{ GeV } c^{-2}$ respectively. The green dotted line shows the published experimental projections for LZ. All three lines assuming the SHM. *Right*: Same as left, but now using the XENON1T experimental parameters to calculate the 90% confidence level limits.

Fig. 2.13 shows the 90% confidence limit on the SI WIMP-nucleon cross-section as taken from the relevant published article and the produced value of the code before and post scaling for both LZ (*left*) and XENON1T (*right*). When reproducing the limit, the SHM has been used with velocities as stated by the relevant detectors publication.

As can be seen in Fig. 2.13, the calculated and experimental limits do not agree. Additional signal region selection efficiencies, as well as event reconstruction efficiencies, should be included. These efficiencies are determined by experiments using full detector simulations. Their dependence on the DM particle mass is not strong, and they could be taken into account as simple scale factors at high masses (we take 100 GeV c^{-2} mass point). The resulting limits agree with the experimental ones much better. The remaining discrepancies could be due to non-perfect matching of efficiency curves extracted from the publications and possible mass dependence of signal region selection and event reconstruction efficiencies. Given we are interested in relative effects due to velocity models, this agreement is good enough for our purposes. One disadvantage of scaling is that it is no longer possible to see the impact of the local density differences between the calculated and experimental limits.

2.5.2.2 Exclusion limits for the ARTEMIS halos

As discussed in Section 2.2.2, the limits placed on the WIMP-nucleon cross-section depend not only on several local DM properties, but also on various experimental parameters such as the sensitive material and mass, energy-dependent detection and selection efficiencies, background events, and the number of days the experiment runs for (i.e. live-days). The XENON1T direct detection experiment (Aprile et al., 2017b, 2018) provides constraints on value on the WIMP-nucleon cross-section, with an upper limit on the WIMP-nucleon spin-independent cross-section of $4.1 \times 10^{-47} \text{ cm}^2$ at a WIMP mass of $30 \text{ GeV } c^{-2}$. This experiment has been carried out over 278.8 live-days with a 1.3-tonne detector, equivalent to 1.0 tonne over a year. The most sensitive projections from the LZ experiment were carried out with a 5700 kg Xenon detector over 1000 live-days (Akerib et al., 2020). This places an upper limit on the WIMP-nucleon spin-independent cross-section of $1.4 \times 10^{-48} \text{ cm}^2$ at a WIMP mass of $40 \text{ GeV } c^{-2}$. For our

calculations, we use the full recoil energy of 1 - 60 keV_{nr} covered by both detectors and apply the energy-dependent efficiencies extracted from the publications.

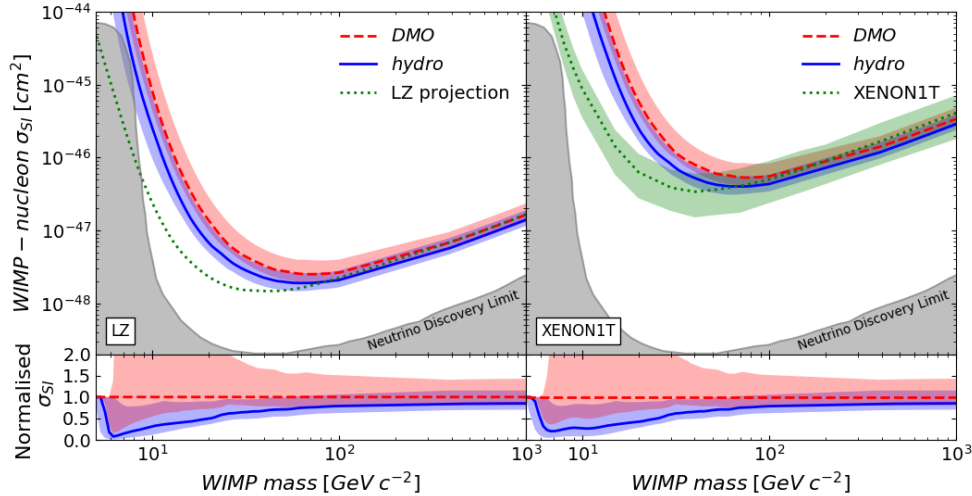


FIGURE 2.14: *Left*: The 90% confidence level limits for the ARTEMIS halos using the LZ parameters (Akerib et al., 2020). The median upper-limits are shown as red dashed and blue solid lines for the DMO and hydro case, respectively. The contours enclose 68% of all the individual exclusion limits for all of the halos. The green dotted line shows the published experimental projections for LZ assuming the SHM and the green shaded region corresponds to the 1σ experimental uncertainties on the limits. *Right*: Same as left, but now using the XENON1T experimental parameters to calculate the 90% confidence level limits. The lower panels show the uncertainties on the WIMP cross-sections normalised by their respective 90% confidence level limits.

The exclusion limits based on the simulated Milky Way-mass halos, which use the best fitting Maxwellian velocities, and the LZ direct detection experiments can be seen in the left panel Fig. 2.14 (with red for DMO and with blue for hydro). The coloured regions enclose 68% of all the individual exclusion limits for the 42 halos, while the solid and dashed lines show the median values for all the halos. The right panel of Fig. 2.14 shows the same result but using the XENON1T experimental parameters. The green dotted lines in the left and right panels indicate the 90% confidence level limits from LZ and XENON1T collaborations, respectively. These exclusion limits were calculated using the SHM with a peak speed of 220 km s^{-1} , a local DM density of 0.3 GeV cm^{-3} and an escape velocity of 544 km s^{-1} , which are the assumed values for both XENON1T and LZ experiments. The green shaded regions correspond to the published 1σ experimental uncertainties (projections in the case of LZ) on the published limits. The lower panels in Fig. 2.14 show the uncertainties on the WIMP-nucleon cross-section exclusion

limits when normalised by the median 90% confidence level limits corresponding to the individual cases, in order to more clearly demonstrate how the halo-to-halo variation in the limits compares with the typical experimental uncertainty.

The exclusion limits for the simulations (DMO and hydro) are higher in amplitude at low WIMP masses ($< 50 \text{ GeV } c^{-2}$) compared to the published limits for XENON1T and LZ. This is just due to the fact that the latter use the SHM with $v_0 = 220 \text{ km/s}$, whereas the median v_0 for the ARTEMIS halos is closer to 180 km/s (see Fig. 2.3). However, our focus is primarily on relative effects, namely the relative effect of including baryons and the halo-to-halo scatter.

Our results show that the hydro halos place lower upper limits on the cross-section compared to their matched DMO counterparts. We also observe a large halo-to-halo variation in the WIMP cross-sections for both hydro and DMO halos. Typically, the 1σ scatter in the exclusion limits is a factor of ≈ 1.5 but increases to a factor of several at low WIMP masses. Both of these results can, in part, be explained by considering the local DM densities; the WIMP-nucleon cross-section is inversely proportional to the local DM density, and the densities are higher in the solar neighbourhood in the hydro simulations. In addition, the enhanced peak velocities in the hydro simulations lower the cross-section constraints at the low mass end. The halo-to-halo variation in the DM density and peak velocities propagates through to the spread seen in the exclusion limits.

It is important to note that the halo-to-halo variation in the exclusion limits is smaller than the current experimental uncertainties for XENON1T but not by large amounts (compare the width of the green shaded region with the widths of the red and blue shaded regions). In fact, at low WIMP masses of $< 20 \text{ GeV } c^{-2}$, the simulated scatter is larger than the experimental uncertainties for XENON1T. The (projected) experimental uncertainties in the LZ experiment are slightly larger than that of XENON1T, however these are still comparable at low WIMP masses, as the modelling uncertainty becomes increasingly important. Given that this is the case, it suggests that the modelling uncertainties (i.e., in $\rho_0, v_0, v_{\text{esc}}, f(v)$) should be included in the overall error budget in order to derive a conservative estimate of the cross-section limits.

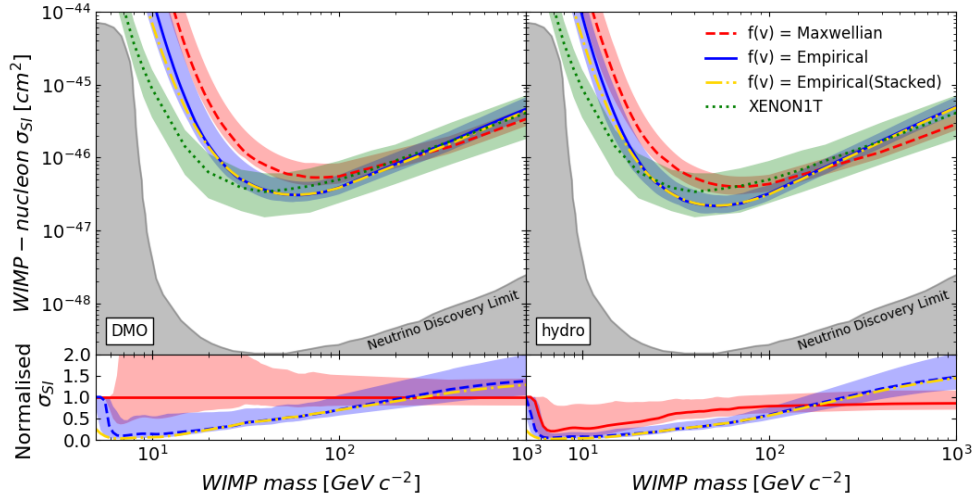


FIGURE 2.15: *Left*: The 90% confidence level limits using the ARTEMIS DMO halos using XENON1T parameters. The median upper-limits are shown as red dashed, and solid blue lines for a Maxwellian $f(v)$ and empirical $f(v)$, respectively. The yellow dot dashed lines show the results from stacking all of the halos VDFs in our sample. The contours enclose 68% of all the individual exclusion limits for all of the halos. The green dotted line shows the experimental limit from XENON1T along with the 1σ error (green contour), which uses the Standard Halo Model. *Right*: Same as left, but for the hydro halos. The lower panels show the uncertainties on the WIMP cross-sections normalised by their respective 90% confidence level limits.

2.5.3 Empirical $f(v)$ model

We have shown that the Maxwellian function does not describe the DMO simulations well and, even though this issue is significantly reduced for the hydro simulations, it still does not represent a perfect description of the velocity distribution in those simulations either. We therefore explore the impact of using the exact (empirical) form for $f(|v|)$ from the simulations to calculate the detection limits, via equation 2.6. We calculate the detection limits for each halo, interpolating $f(|v|)$ where necessary between the v_{\min} and v_{\max} limits.

The results of using the empirical DM velocity distributions in both DMO and hydro simulations can be seen in the left and right panels of Fig. 2.15, respectively. The red dashed curve represents the median exclusion limits where $f(|v|)$ is assumed to be a Maxwellian distribution (as used in the SHM), and the blue solid line shows the median result when using the empirical $f(|v|)$ determined directly from the simulations. The yellow dot dashed line shows the limits placed on the WIMP cross-section using an

empirical model derived from stacking all of the halos in our sample. Stacking the halos better populates the tails of the velocity distribution function, leading to a higher integrated rate and, therefore, lower WIMP masses to be excluded. (This is similar to increasing the value of v_{esc} .)

This comparison shows that the empirical method results in a significant reduction in the upper limits placed on the cross section for masses less than $\approx 100 \text{ GeV } c^{-2}$. This difference is present for both the DMO and hydro cases but is larger for the DMO case due to its more significant deviation from the a Maxwellian distribution (particularly at high velocities). The halo-to-halo variation still persists in the empirical case and remains comparable to both the Maxwellian model and experimental results, reinforcing the importance $\rho_0, v_0, v_{\text{esc}}$ when determining the exclusion limits.

2.6 Summary and conclusions

Direct detection experiments require estimates of the local DM density and velocity distributions in order to place constraints on the DM particle mass and cross-section. We have used the new ARTEMIS suite of high-resolution cosmological simulations of Milky Way-mass galaxies to determine the local densities and velocity distributions of DM in the presence or absence of baryons and across a variety of galaxy accretion histories. We have investigated the range in $\rho_0, v_0, v_{\text{esc}}$ in the simulations in order to inform the standard halo model implemented in direct detection pipelines. We have also investigated the degree to which the Maxwellian assumption for DM particle velocities is valid and have explored the impact of using a more realistic empirical function $f(v)$ from the simulations. Using these results, we have estimated the uncertainties in the WIMP cross-section limits for the LZ and XENON1T direct detection experiments, under the assumption of a WIMP-nucleon spin-independent elastic scattering.

Our main conclusions are as follows:

1. The simulations predict local parameters ($\rho_0, v_0, v_{\text{esc}}$) which are generally in good agreement with observations, within the observational uncertainties. The local

DM density in the solar neighbourhood ranges between $0.15 - 0.48 \text{ GeV cm}^{-3}$ in the hydro simulations and between $0.10 - 0.38 \text{ GeV cm}^{-3}$ in the DMO simulations (Fig. 2.2). The increased values of ρ_0 in the hydro simulations relative the DMO simulations are likely to be caused by the adiabatic contraction in the presence of baryons. Even taking this effect into account, our simulations disfavour the larger values of $> 0.6 \text{ GeV cm}^{-3}$ obtained in some recent measurements.

2. The median local DM velocity distribution is relatively well (but not perfectly) described by a Maxwellian distribution for the hydro halos, but less so for the DMO halos (Fig. 2.3). Relatively large halo-to-halo variations are observed in both hydro and DMO simulations (Fig. 2.4). The addition of baryons and associated cooling and adiabatic contraction of the DM cause an increase in the peak velocities, typically by about 30 km s^{-1} .
3. Substructure (subhalos, streams) can pass inside the solar neighbourhood (Fig. 2.6), however this does not often occur in the cosmological context for relatively high-mass substructures that could significantly influence the DM detectability rates. Dark discs, however, are found in a relatively large proportion of the hydro halos. By a conservative estimate, $\approx 15\%$ of our sample have dark discs, but the fraction can be as high as $\approx 36\%$ (Fig. 2.11) depending on how one defines a dark disc. The presence of dark discs increases the local DM density and can also lead to significant deviations from Maxwellian velocity distribution.
4. The enhanced DM densities and peak velocities in hydro simulations relative to DMO simulations lead to higher differential scattering rates in the former, and therefore to lower exclusion limits on the WIMP-nucleon cross-section (Fig. 2.14). In addition, the halo-to-halo scatter in the implied exclusion limits (due to scatter in the density and velocity distributions) is relatively large; typically a factor ≈ 1.5 and increasing towards lower WIMP masses. This is only slightly smaller than the experimental uncertainties on the published XENON1T and LZ (projected) limits. In fact, at low WIMP masses ($< 20 \text{ GeV } c^{-2}$) the simulation-based scatter typically exceeds the experimental uncertainty. We therefore conclude that the astrophysical systematic uncertainties should in general be included as

part of the overall error budget. This is important both for deriving a conservative estimate on the cross-section limits and for when comparisons are made to constraints on DM properties derived from indirect and collider searches.

5. An empirical form for $f(\vec{v})$ slightly lowers the exclusion limits, with the most significant difference seen when at WIMP mass $< 100 \text{ GeV } c^{-2}$ (Fig. 2.15). This suggests that use of a Maxwellian form in the SHM generally puts a conservative limit on the exclusion limits compared with a more realistic model for the velocity distribution at masses of $< 100 \text{ GeV } c^{-2}$ (at higher masses, the opposite is true).

Chapter 3

Modelling the prospects of detecting dark matter annihilation with CTA using the ARTEMIS simulations

The majority of the work presented in this chapter is currently under preparation for submission to a peer reviewed journal.

3.1 Introduction

Dark matter (DM) is the dominant form of matter in the Universe ([Planck Collaboration et al., 2020](#)), but its nature remains unknown. Although many candidates for the DM particle have been proposed theoretically, primarily through extensions of the Standard Model of particle physics ([Feng, 2010](#)), the confirmation of the nature of this elusive component will ultimately come from its detection.

To date many searches have focused on detecting the Weakly Interactive Massive Particles (WIMPs), who are attractive DM candidates on several grounds, one of them being that they are predicted by Supersymmetry. The WIMP mass is predicted to be in the range of $\approx 2 \text{ GeV} - 100 \text{ TeV}$, depending on the type of particle (e.g., see [Roszkowski](#)

et al. (2018)). This energy range has been explored intensely via both direct and indirect DM detection experiments. Some part of this energy range remains to be explored, such as for example, the higher energy end which can be probed through indirect DM detection.

If WIMP particles self-annihilate, their particle masses can be inferred from the energy spectrum of γ -rays that may result from this process. Despite years of intense searching, no detection of DM annihilation has been made so far, including observations done by the Fermi Gamma-ray Space Telescope (FGST) (GLAST Facility Science Team et al., 1999; Charles et al., 2016) and the ground-based Imaging Atmospheric Cherenkov Telescopes (IACTs) such as H.E.S.S. (Hinton & HESS Collaboration, 2004), MAGIC (Lorenz & MAGIC Collaboration, 2004) and VERITAS (Weekes et al., 2002). However, the WIMPs remain an interesting target for future DM indirect detection facilities, which can probe the higher end of the above energy regime, in particular for the Cherenkov Telescope Array (CTA).

The CTA is the next generation of ground-based γ -ray observatory (CTA Consortium & Ong, 2019) that will survey a much larger region of the sky, at energies of ≈ 20 GeV – 300 TeV and with increased sensitivity. The main sites for potentially detecting the DM annihilation in the Milky Way are the Galactic Centre (GC) and the centres of nearby dwarf galaxies. Both of these are key science projects of the CTA (e.g., Acharyya et al. 2021). Due to the high DM density and its relative closeness, the GC is expected to be a brighter source of γ -rays than local dwarf galaxies (e.g., Bertone et al. 2005; Strigari 2013). However, the GC suffers from strong γ -ray contamination from astrophysical sources such as the supermassive black hole at the centre, the millisecond pulsars, and supernovae, all of which need to be modeled carefully in order to disentangle the potential DM signal (e.g., Dodelson et al., 2008; Silverwood et al., 2015). Dwarf galaxies are supposed to be sources that are less contaminated by foreground radiation since many of them are far away from the Galactic plane where most of the astrophysical sources reside. In addition, these systems have low fractions of obscuring gas and dust (Ackermann et al., 2014) and are DM-dominated, making them easier to model.

Several predictions for the expected signal of γ -ray radiation in indirect detections have already been made, using either analytical models or numerical simulations. However, some uncertainties in these types of estimates still remain. For example, analytical modeling requires an assumption of the density profile of the DM halo, as the annihilation rate relies on the square of the DM density. Observationally, the density profile of the Milky Way's DM halo can be inferred from measurements of the rotation curve in the disc. Apart from the known degeneracies in the modeling, the rotation curve is poorly constrained within a few kpc of the GC, due to a combination of less accurate data and the large uncertainties associated with the distribution of baryons (Pato & Iocco, 2015; Iocco et al., 2015). Another parameter needed in the analytical modeling is the total mass of the Galactic DM halo, which until recently has been known only within a factor of 2. However, thanks to data from the Gaia satellite the total MW mass is now much better constrained (Callingham et al., 2019; Posti & Helmi, 2019; Deason et al., 2019; Vasiliev, 2019). For satellite dwarf galaxies, the masses can be inferred from the stellar velocity dispersions and their half-light radii (Walker et al., 2009), which in turn, are model-dependent. Furthermore, the modeling requires some information that is not directly measurable, e.g., the internal velocity distribution of DM halos or subhalos.

Cosmological simulations can provide more accurate predictions since the growth of DM structure is modeled self-consistently (as are some of the baryonic physics processes, in the case of hydrodynamical simulations). This allows a more realistic treatment of dynamical friction and various tidal interactions that affect the abundance of satellite galaxies, their spatial distribution, and their internal structure.

Numerically, the DM annihilation limits in Milky Way-type systems, including their dwarf satellite galaxies, have been investigated first with DM-only simulations (Calcáñez-Roldán & Moore, 2000; Stoehr et al., 2003; Diemand et al., 2006, 2007; Kuhlen et al., 2008; Springel et al., 2008). These simulations were able to resolve the internal structure of DM halos down to very small scales (for example, subhalos of $\approx 10^4 M_{\odot}$ in the case of the Aquarius simulations; see Springel et al. 2008). Cosmological simulations, however, are unable to resolve subhalos below some level dictated by their numerical resolution, which implies that a whole range of subhalos that can contribute to the overall annihilation signal are not resolved (in a Λ CDM model, the minimum subhalo mass

that can contribute to the DM annihilation signal is several orders of magnitude below the level that can be currently resolved). These unresolved halos must be accounted for analytically (see e.g., [Strigari et al. 2007](#)), which means that one needs to resort to additional assumptions about the internal structure of unresolved DM subhalos, thus introducing more uncertainties in the predictions.

Another important factor that needs to be taken into account is the presence of baryons. These can have significant effects on the structure of DM halos and consequently on the predictions for DM annihilation. However, there is a complex interplay between different baryonic processes that is currently not well understood. For example, baryons can lead to the adiabatic contraction of the Galactic DM halo (e.g., [Blumenthal et al., 1986](#); [Ryden & Gunn, 1987](#)) and therefore to an enhancement in the DM annihilation at the GC, but to a weaker signal from the DM substructure, due to the more efficient tidal disruption of subhalos that orbit near the GC by the denser part of the host halo. On the other hand, supernovae feedback can flatten cuspy DM profiles, turning them into cored ones (e.g., [Pontzen & Governato, 2012](#); [Di Cintio et al., 2014](#); [Benítez-Llambay et al., 2019](#)). Cored dwarf galaxies are tidally disrupted more easily, whereas a cored Galactic DM halo can lead to a substantially reduced annihilation signal from the GC (e.g., [Evans et al., 2004](#)). Moreover, the presence of a Galactic stellar disc contributes to the tidal destruction of the substructure (e.g., [Berezinsky et al., 2006](#); [D’Onghia et al., 2010](#); [Garrison-Kimmel et al., 2017](#)), further reducing the number of potential γ -ray sources from the DM substructure. Therefore DM-only simulations, which by construction cannot capture these effects, may not provide sufficiently accurate estimates for the annihilation signal.

To follow the baryonic effects, and to determine quantitatively how they affect the resulting DM annihilation limits, it is therefore necessary to use cosmological hydrodynamical simulations. Several studies have already used this type of simulations, although they have been more limited in scope. For example, [Calore et al. \(2015\)](#) and [Schaller et al. \(2016a\)](#) have used the EAGLE ([Schaye et al., 2015](#); [Crain et al., 2015](#)) and APOSTLE ([Sawala et al., 2016](#)) simulations in order to explain the puzzling 2 GeV γ -ray emission excess measured near the GC by the Fermi satellite ([Ackermann et al., 2017](#)). However, the results were inconclusive. With a sample of 4 MW-like halos

Schaller et al. (2016a) found that the predicted DM annihilation signal approximately agrees with the Fermi observational excess. In contrast, using a slightly larger sample size of 12 Milky Way-mass halos from EAGLE and another 2 from APOSTLE, Calore et al. (2015) found that their DM annihilation signal predictions are unable to account for the excess.

Although the aforementioned possible detection has not been confirmed, nor any other ones that have been since suggested (e.g., Cui et al., 2017), the situation may stand to change with the advent of CTA. The increased sensitivity and extended sky coverage of the CTA allows a more in-depth exploration of the mechanism of DM annihilation. However, the observations need to be accompanied by more accurate predictions of the DM annihilation signals, for example of ones that take into account the full extent of baryonic physics.

In this study we use the ARTEMIS suite of cosmological hydrodynamical simulations (Font et al., 2020) in order to estimate the DM annihilation signals from the GCs of MW-like systems and from their present-day population of DM subhalos, taking into account the expected instrumental sensitivity of the CTA. The simulated sample comprises 45 MW-mass systems, which allows a statistical study of the indirect DM detection limits, as well as of the variations from system-to-system. The diverse range of merger histories of these galaxies enables us to account for the uncertainties in the formation of the Milky Way. In addition, we have constructed a corresponding set of 45 DM-only simulations of the same systems, which we use to compare to the hydrodynamical set and quantify the role of baryons on the limits of DM detection. We also test the sensitivity of the CTA for detecting the predicted DM annihilation signal from the GC and from the (stacked) satellite dwarf galaxies. We also investigate the limits of detection under various assumptions for the annihilation channels and different DM particle masses.

The paper is organised as follows. Section 3.2 describes the simulations and the main properties of host MW-mass galaxies and their substructure. Section 3.3 presents the methodology for computing the DM annihilation luminosity of individual DM subhalos, including the boost factors. Section 3.4 discusses the fluxes associated with the annihilation signal and includes examples of synthetic all-sky flux maps. Section 3.5

discusses the potential detectability of the annihilation signal from the GCs and DM subhalos with CTA. Finally, section 3.6 summarises our main findings.

3.2 Simulations

The ARTEMIS suite comprises 45 Λ CDM cosmological simulations of Milky Way-mass halos, 42 of which were introduced in Font et al. (2020) and 3 additional systems in Font et al. (2021). These systems were selected from a larger, periodic box of $25 \text{ Mpc } h^{-1}$ on a side and re-simulated at higher resolution with hydrodynamics using a ‘zoom in’ technique. The selection was made solely on their total mass, with no additional constraints (e.g. on the type of merger histories). The total masses range between $8 \times 10^{11} < M_{200}/M_{\odot} < 2 \times 10^{12}$, where M_{200} is the mass enclosing a mean density of 200 times the critical density at present time. The DM particle masses are $1.17 \times 10^5 M_{\odot} h^{-1}$, the initial baryon particle masses are $2.23 \times 10^4 M_{\odot} h^{-1}$, while the force resolution (the Plummer-equivalent softening) is $125 \text{ pc } h^{-1}$.

The hydrodynamical simulations were carried out with the Gadget-3 code with an updated hydro solver and subgrid physical prescriptions that model metal-dependent radiative cooling in the presence of a photo-ionizing UV background, star formation, supernova, and active galactic nuclei feedback, stellar and chemical evolution, and formation of black holes. These are described in detail in Schaye et al. (2015) and references therein. The simulations match, by construction, very well the stellar mass – halo mass relation for galaxies in this mass range (see Font et al. 2020 for details). They also match the observed sizes and star formation rates of Milky Way-mass galaxies without an explicit calibration for these quantities. The simulations fully accommodate the range of stellar masses and magnitudes of observed Milky Way analogues in the Local Volume and beyond (Font et al., 2021) and match remarkably well the luminosity functions and radial distributions of dwarf satellite galaxies of these analogues (Font et al., 2021).

In addition to the hydrodynamical set of simulations (henceforth called ‘hydro’) we ran DM-only versions (henceforth called ‘DMO’) of the same MW-mass systems. The

global properties of the DMO Milky Way-mass host galaxies are presented in more detail in [Poole-McKenzie et al. \(2020\)](#), whereas the properties of the hosts in the hydro runs are described in [Font et al. \(2020, 2021\)](#). The halos in the DMO simulations are further matched with those in the hydro ones using the unique particle IDs of the DM particles. This cross-matched list of halos allows us to study the impact of baryons on various halo properties, using the collisionless (i.e., DMO) simulations as a reference system.

All simulations adopt a flat Λ CDM WMAP9 ([Hinshaw et al., 2013](#)) cosmology with $\Omega_m = 0.2793$, $\Omega_b = 0.0463$, $h = 0.70$, $\sigma_8 = 0.8211$ and $n_s = 0.972$.

3.2.1 Halo substructure

The properties of the substructure in the ARTEMIS simulations have been investigated before. For example, the abundance and radial distributions of satellite galaxies were studied in [Font et al. \(2021\)](#), the internal structure of subhalos in [Stafford et al. \(2020\)](#) and the imprints that DM subhalos leave in the intergalactic gas or in the distribution of the host stars were studied in [McCarthy & Font \(2020\)](#) and [Poole-McKenzie et al. \(2020\)](#), respectively. Since here we are interested to estimate the DM annihilation signal from the substructure, it is important first to evaluate how the presence of baryons affects the abundance of DM subhalos.

In [Fig. 3.1](#) we compare the number density of substructure in the hydro versus DMO runs. The median cumulative subhalo mass functions for all subhalos within the virial radii, R_{200} , of the 45 MW-mass systems at $z = 0$ are shown with full lines, blue for the hydro and red for the DMO runs, respectively. (For reference, in ARTEMIS the host R_{200} values range between 180 – 250 kpc; see [Font et al. 2020](#)). The hashed regions represent the 68% scatter around these medians. As expected, the run including baryons shows consistently lower abundances of subhalos than the DMO run. For example, around the 200 DM particle limit (i.e. a conservative limit on the ability to resolve the internal structure of the DM subhalos), which is equivalent to subhalo masses of

$\approx 4 \times 10^7 M_\odot$, the hydro simulations contain about 70% of the DM subhalos in the DMO ones (~ 114 subhalos in the hydro compared to ~ 160 in DMO).

The effects of baryons are expected to be stronger near the centres of the MW systems. To check this, we show also the mass function of the subhalos in the inner regions of their hosts, specifically those presently located $< 0.5R_{200}$ of the MW-mass hosts. These are shown with dashed lines in Fig. 3.1. In this case, the difference in the number of subhalos is even greater. This can be explained by the more efficient tidal disruption of satellites in the inner regions in the presence of stellar discs and enhanced central densities of the MW-mass hosts, as discussed in the Introduction.

Note that, in both hydro and DMO runs, the subhalo mass functions start to converge at $M_{\text{sub}} \approx 2 \times 10^7 M_\odot$ (i.e., to the left of the vertical dashed line), due to numerical resolution effects. For the remainder of this work we only include subhalos with more than 200 DM particles inside R_{200} .

The differences in the resulting abundances of DM subhalos in hydro versus DMO simulations highlights the importance of including baryonic physics in predicting the DM annihilation signal from these systems. In addition to reducing the abundance of DM subhalos, baryons can also change the inner structure of these subhalos, which in turn can modify the predicted signal. The structure of density profiles of the host halos and their subhalos in ARTEMIS has been investigated in detail by Stafford et al. (2020). These authors found that for host halos with masses of $10^{11.75} \leq M_{200,\text{crit}}/M_\odot < 10^{12.33}$, the presence of baryons leads to steeper central densities ($\lesssim 0.1 R_{200,\text{crit}}$) compared with the DMO counterparts; this being due to adiabatic contraction. This implies the potential annihilation signal from the GC is stronger in the more realistic case when baryons are taken into account.

3.3 The γ -ray luminosity of DM annihilation

Here we evaluate the γ -ray luminosity from 2-body DM annihilation for the host DM halos and the DM subhalos in our simulations. This luminosity depends on the density

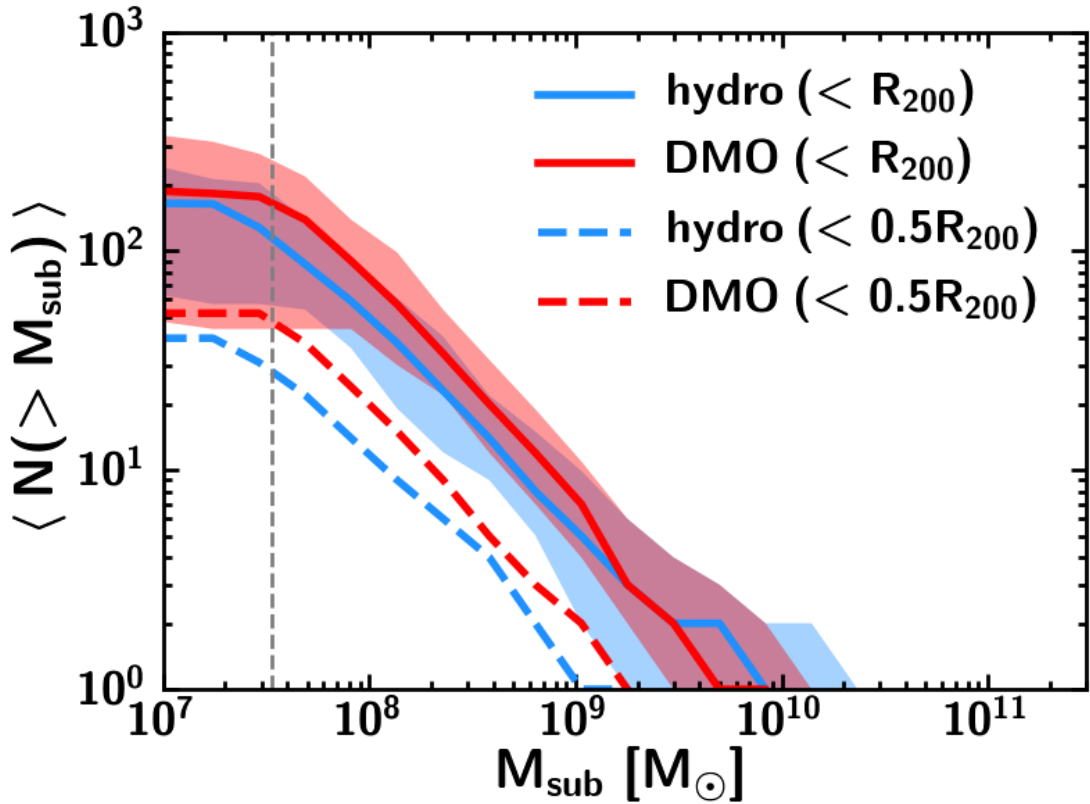


FIGURE 3.1: The median cumulative subhalo mass functions for the simulated subhalos within R_{200} (solid lines) and $0.5 R_{200}$ (dashed lines) for both DMO (red) and hydro (blue) simulations. The grey dotted line shows the convergence limit which corresponds to a subhalo with ≈ 200 DM particles.

of DM as $\propto \rho_{\chi}^2$. For the well-resolved substructure in our simulations, i.e. subhalos with more than 200 DM particles, we compute the total annihilation luminosity \tilde{L} (in units of $M_{\odot}^2 \text{ kpc}^{-3}$) as a simple sum:

$$\tilde{L} = \sum_i^N \rho_i m_i, \quad (3.1)$$

where m_i and ρ_i are the mass and density of the i^{th} DM particle, respectively, and N is the number of DM particles within the radius of the (sub)halo, R_{sub} . This radius is computed by the substructure finding code SUBFIND (Dolag et al., 2009). The DM particle density, ρ_i , is calculated using an SPH (Smoothed Particle Hydrodynamics) smoothing kernel with the volume determined by each particle's nearest 32 neighbours, as in Springel et al. (2008).

However, the unresolved substructure in our simulations is also expected to contribute to the annihilation signal, and therefore it needs to be accounted for. In ARTEMIS the DM particle masses are of the order of $10^5 M_\odot$, which is several orders of magnitude above the mass of the smallest substructure expected in a Λ CDM model. This minimum mass is set by the free streaming length of the DM particle. For example, for a supersymmetric CDM particle candidate with a mass of 100 GeV – 1 TeV, free streaming causes the matter power spectrum to be cut off at a scale of $\sim 10^{-12} - 10^{-3} M_\odot$ (Green et al., 2004; Loeb & Zaldarriaga, 2005; Bertschinger, 2006; Profumo et al., 2006; Bringmann, 2009).

The contribution of unresolved substructure to the total luminosity is incorporated into a ‘boost factor’ term, such that the total annihilation luminosity $L(M)$ of a DM halo is given by:

$$L(M) = [1 + B(M)]\tilde{L}(M), \quad (3.2)$$

where $\tilde{L}(M)$ is the total unboosted annihilation luminosity for a subhalo of mass M . For simplicity, this is usually modeled assuming a smooth spherical halo, and therefore \tilde{L} can be computed as the volume integral:

$$\tilde{L} = \int_0^{R_{\text{sub}}} \rho_\chi^2 dV, \quad (3.3)$$

assuming an appropriate form for the density profile.

Following Strigari et al. (2007), we compute the boost factor, $B(M)$, as:

$$B(M) = \frac{1}{\tilde{L}(M)} \int_{m_0}^{m_1} \frac{dN}{dm} L(m) dm \quad (3.4)$$

$$= \frac{1}{\tilde{L}(M)} \int_{m_0}^M \frac{dN}{dm} [1 + B(m)] \tilde{L}(m) dm, \quad (3.5)$$

where m is the subhalo mass, $\tilde{L}(M)$ and $\tilde{L}(m)$ are the unboosted annihilation luminosities of the smooth halo and subhalos, respectively. The latter are calculated using eq. 3.3 assuming a density profile with a concentration determined from a given concentration - mass (c–M) relation. In this study, we adopt by default the c–M relation of [Ludlow et al. 2016](#) (henceforth denoted as L16), however we also explore the impact of using different c–M relations. We also assume that the subhalo mass function is a power law of the form $dN/dm = A/M(m/M)^{-\alpha}$, where α is typically 1.9 – 2.0 ([Diemand et al., 2007](#); [Madau et al., 2008](#); [Springel et al., 2008](#)). Here we adopt a value of $\alpha = 2$.

The boost factor also depends on the cutoff mass, m_0 , which is the minimum mass to extrapolate the boost function down to (see below). It also depends on the assumed density profile, which is then used to determine the ‘smooth’ (i.e., unresolved) annihilation luminosity. Here we use two density profiles: first one is the Navarro, Frenk & White (NFW) ([Navarro et al., 1996](#)) profile,

$$\rho_{NFW}(r) = \frac{4\rho_s}{(r/r_s)(1 + r/r_s)^2}, \quad (3.6)$$

where r_s is the radius at which the logarithmic slope $\gamma(r) \equiv \frac{d \ln \rho}{d \ln r} = -2$ and $\rho(r_s) = \rho_s$. The other one is the Einasto ([Einasto, 1965](#)) profile,

$$\rho_E(r) = \rho_s \exp \left[-\frac{2}{\alpha_E} \left(\left(\frac{r}{r_s} \right)^{\alpha_E} - 1 \right) \right], \quad (3.7)$$

where α_E controls the degree of curvature of this function. Here we assume $\alpha_E = 0.16$.

The top panel of Fig. 3.2 shows the relation between $B(M)$ and M for different cutoff masses, $m_0 = 10^{-12}, 10^{-9}, 10^{-6}, 10^{-3} M_\odot$, and for the two types of density profiles. This shows that the more massive the subhalo, the larger is the expected boost factor. This is due to larger subhalos having a higher number of subhalos (and subhalos of), all of which contribute to the total annihilation luminosity. This also explains why the boost factor increases with smaller cutoff masses, as smaller subhalos (and sub-subhalos) are included in the boost factor. The $B(M)$ parameter appears to depend only very slightly

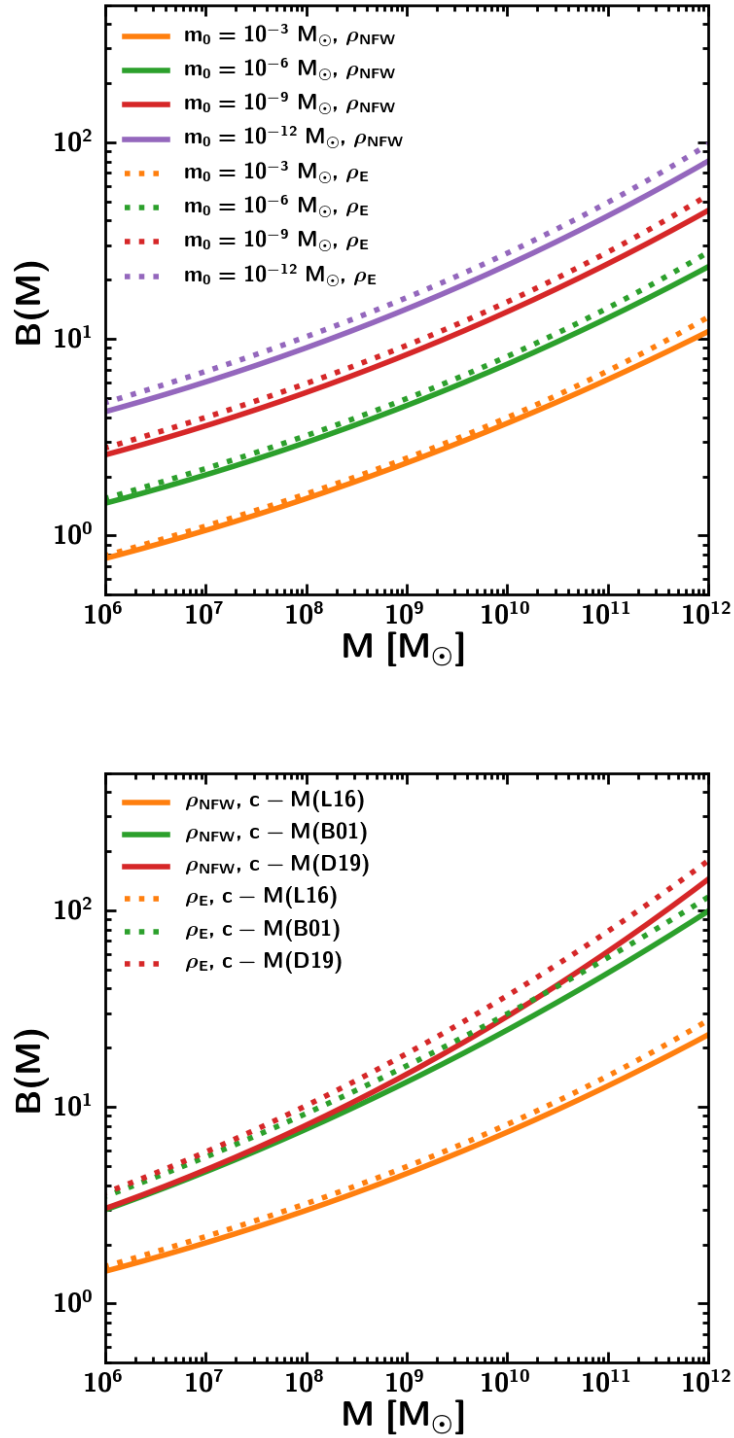


FIGURE 3.2: *Top*: The annihilation luminosity boost factor due to substructure as a function of mass with varying cutoff masses, m_0 , shown with different colours; for each cutoff mass we assume two density profiles, NFW (solid lines) and Einasto (dotted lines). The halo concentrations were inferred from the L16 c - M relation. *Bottom*: The annihilation luminosity boost factor due to substructure as a function of mass with a fixed cutoff mass and varying c - M relations and density profiles.

on the choice of the density profile, with the Einasto profile leading to a slight boost over the NFW profile, across the entire mass range.

The bottom panel of Fig. 3.2 shows the impact of adopting different c – M relations (B01; Bullock et al. 2001 and D19; Diemer & Joyce 2019), for both NFW (solid lines) and Einasto (dotted lines) density profiles. The Einasto profile again results in a higher $B(M)$, increasing slightly with mass. Using the c – M relations from both B01 and D19 produces higher boost factors than that of L16. This increase in $B(M)$ is caused by the c – M relations of B01 and D19 predicting higher concentration values than L16 across all masses.

For the purpose of comparing the results of hydro and DMO simulations, we adopt a fiducial substructure boost function with $\alpha = 2$, $m_0 = 10^{-6} M_\odot$ and an NFW density profile with the halo concentrations determined from the L16 c – M relation. This represents a conservative approach. Adopting either the B01 or D19 c – M relations would result in a factor of $\approx 2 - 5$ increase in the boost factors across all halos masses, an increase which will propagate through to the annihilation signal. The differences in the predicted signal introduced by the assumption of another c – M relation are shown in Section 3.5.

In the following, we will also refer to the smooth spherically averaged halo/subhalos as “unboosted” in comparison with their “boosted” counterparts.

The top sub-panel of Fig. 3.3 shows the median DM annihilation luminosities for unboosted and boosted subhalos, in the hydro and DMO simulations (dashed lines for boosted and full lines for unboosted; and blue lines for hydro and red lines for DMO, respectively). The corresponding luminosities of the MW-mass hosts are shown with empty symbols for boosted and filled symbols for unboosted DM halos; specifically, circles denote hydro simulations and squares the DMO ones. The colour scheme for these two types of simulations is the same as for the subhalos.

No major differences are seen in the annihilation luminosities of the subhalos between the hydro and DMO subhalos, for both unboosted and boosted cases. The annihilation luminosities at lower subhalo masses ($< 10^{10} M_\odot$) are slightly higher in the DMO case,

however at the higher mass end ($> 10^{10}M_{\odot}$) the hydro subhalos have slightly higher luminosities. This change in the annihilation luminosity between the hydro and DMO halos around this mass threshold is caused by the impact of baryonic physics. Specifically, above this mass, the hydro DM halos are more centrally concentrated (this is a consequence of adiabatic contraction, as discussed earlier). The slight difference in luminosities between the hydro and DMO simulations is more apparent, however, in the case of the host halos (namely, hydro DM halos have higher luminosities). Again, this is due to slightly higher concentrations in the hydro halos compared to those in the DMO counterparts.

For comparison, the dotted and dot-dashed lines show the unboosted luminosity-mass relation calculated from eq. 3.3 assuming NFW (purple) and Einasto (yellow) density profiles and using the L16 c - M relation. These agree well with the unboosted luminosities computed from the simulations.

The lower panel of Fig. 3.3 shows in more detail the differences in the annihilation luminosities, shown here as the ratios of luminosities in the DMO over the hydro runs, versus the subhalo masses. This shows more clearly the cross-over of ratios from below to above 1 around the mass of $\approx 10^{10}M_{\odot}$. Note that only the most massive dwarf galaxies in the Milky Way have masses above this value (e.g., SMC or LMC). This indicates that the baryonic effects are more relevant for measurements in these types of systems.

This suggests that baryonic effects impact the DM annihilation signal only at the high mass DM subhalos, although the net increase in the signal due to the addition of baryons may be small. The inclusion of the boost factor, however, is crucial in for predicting the DM annihilation signal from both host halos and their substructure, as it increases the annihilation luminosities, particularly at the higher mass end.

As expected, the high mass subhalos provide the strongest DM annihilation luminosities. However, observationally, one measures the flux rather than the luminosity, therefore the distances to these objects are also important. These are investigated below.

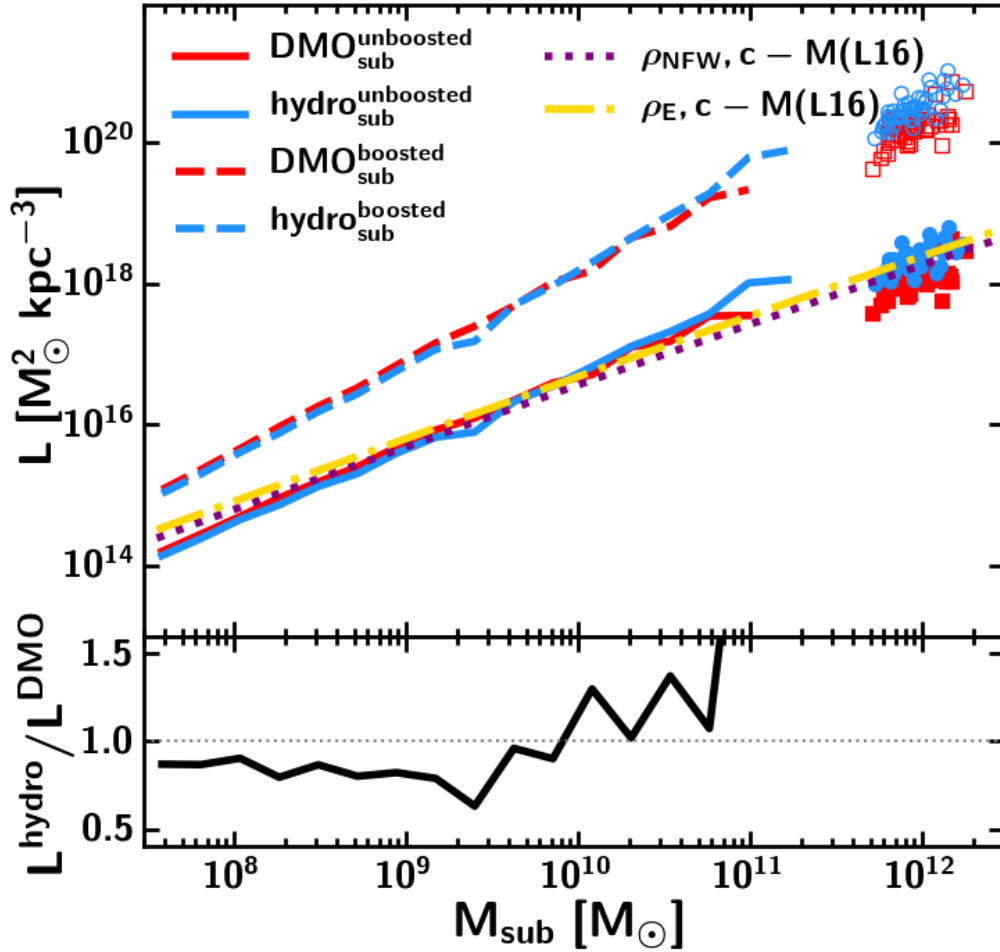


FIGURE 3.3: *Top*: Dark matter annihilation luminosity as a function of subhalo mass averaged over all (resolved) subhalos in all MW-mass systems. The solid lines represent the median smooth spherically averaged luminosity of the DMO (red) and hydro (blue) subhalos. The dashed lines represent the median luminosity of the boosted DMO (red) and hydro (blue) subhalos, using our fiducial model (see text for details). The filled circles and squares represent the smooth spherically averaged annihilation luminosity for individual DMO (red) and hydro (blue) host halos. The empty circles and squares are the same but now showing the host halos after applying the boost factor. The dotted purple and dot-dashed yellow lines show the luminosity-mass relation calculated from NFW and Einasto density profiles respectively, using the L16 c - M relation. *Bottom*: The ratio of median hydro and DMO annihilation luminosities, versus subhalo mass.

3.4 Annihilation fluxes and all-sky maps

Above we investigated the annihilation luminosity, however this is mass-dependent and does not take into consideration the distance to the subhalo or its area on the sky. For

example, if we consider two identical subhalos of equal masses (hence luminosities) placed at different distances from the observer, the closest one would produce a higher DM annihilation flux. This flux is a measurable quantity. The DM annihilation flux from any given DM particle i is:

$$F_i = L_i / 4\pi d_i^2, \quad (3.8)$$

where L_i is the DM annihilation luminosity of the particle and d_i is the distance to the particle from an observer. For the following, we assume an observer located at the ‘solar neighborhood’, approximately at 8.5 kpc from the GC. In practice, we assume a fixed distance of $0.04 \times R_{200}$, to account for the differences in R_{200} values of the simulated MW-mass hosts.

First, we create all-sky DM annihilation flux maps from the simulations. For these, we use the Healpy and HEALPix¹ package (Zonca et al., 2019; Górski et al., 2005), dividing the sky into equal-area pixels and mapping it onto a Mollweide projection. We choose NSIDE = 1024 to achieve the angular resolution of CTA ($\approx 0.05^\circ$ for a 1 TeV γ -ray) (CTA Consortium & Ong, 2019; Maier, 2019). In these maps, the annihilation fluxes are computed by summing up the fluxes of all particles in each pixel/angular bin and then divide them by the pixel area, resulting in a map of annihilation flux per solid angle, ϕ .

We note that the methods used here are similar to other all-sky flux maps generated from cosmological simulations (e.g., Diemand et al., 2006; Springel et al., 2008). In contrast, however, previous studies used DM-only simulations and fewer MW-mass systems. For example, the Via Lactea simulation of Diemand et al. (2006) was a realization of a single MW-size halo, albeit at very high resolution. Similarly, the Aquarius simulations of Springel et al. (2008) included five MW-mass halos and the associated substructure. These authors found that the most important source of γ -ray flux is the host halo of the Milky Way, while the small-scale structure has a negligible contribution. With ARTEMIS, we are able to explore the impact of baryons on the all-sky flux maps.

¹<http://healpix.sourceforge.net>

Additionally, having a much larger sample of MW-mass halos, allows us to investigate multiple such realizations and the system-to-system variations.

Fig. 3.4 shows all-sky γ -ray flux maps (per solid angle) for one of the MW-mass systems in ARTEMIS, denoted ‘G9’ in Font et al. 2020. The two maps correspond to this system in the hydro (left column) and the DMO runs (right), respectively. The rows from top to bottom correspond to the total γ -ray flux, i.e., including the emission from both host halos and subhalos, the flux from the host halo only and, lastly, from only the subhalos. As discussed before, the host halo in the hydro case has less substructure than its matched DMO counterpart, which is also seen in the flux maps. The discrepancy between the number of subhalos increases with decreasing subhalo mass (as shown quantitatively in Fig. 3.1). Additionally, the ‘shapes’ of the flux distributions in the host halos are different in the two cases, being more centrally concentrated and more spherical in the presence of baryons.

The example of the system ‘G9’ is not unique, the other systems in the sample showing similar features. For example, all DMO halos have more subhalos and when compared to their hydro counterparts. Additionally, the majority of the hydro host halos have less spherical flux distributions than their DMO counterparts. The shapes of the DM halos in ARTEMIS have been investigated in Poole-McKenzie et al. (2020), where it was found that the hydro host halos are more spherical and less triaxial than their DMO counterparts, due primarily to adiabatic contraction (see figure 7 in that study).

Fig. 3.5 shows the γ -ray fluxes from individual subhalos and host halos, versus their mass. The fluxes are calculated using eq. 3.8, summing over all DM particle fluxes, F_i , in a given (sub)halo. We compute both the unboosted annihilation flux, \tilde{F} , and the boosted one, F . The full lines in the top subpanel of Fig. 3.5 show the median unboosted fluxes of all the (sub)halos in the sample, for the hydro (blue) and DMO (red) runs. The dashed lines correspond to the median boosted fluxes. As before, we show separately the median values of host halos with filled and empty symbols, corresponding to the unboosted and boosted fluxes, respectively. As in the case of annihilation luminosities, the fluxes are generally very similar in the runs with and without baryons. Also as before, the DMO subhalos generate more flux below $M_{\text{sub}} \approx 10^{10} M_{\odot}$, after which the

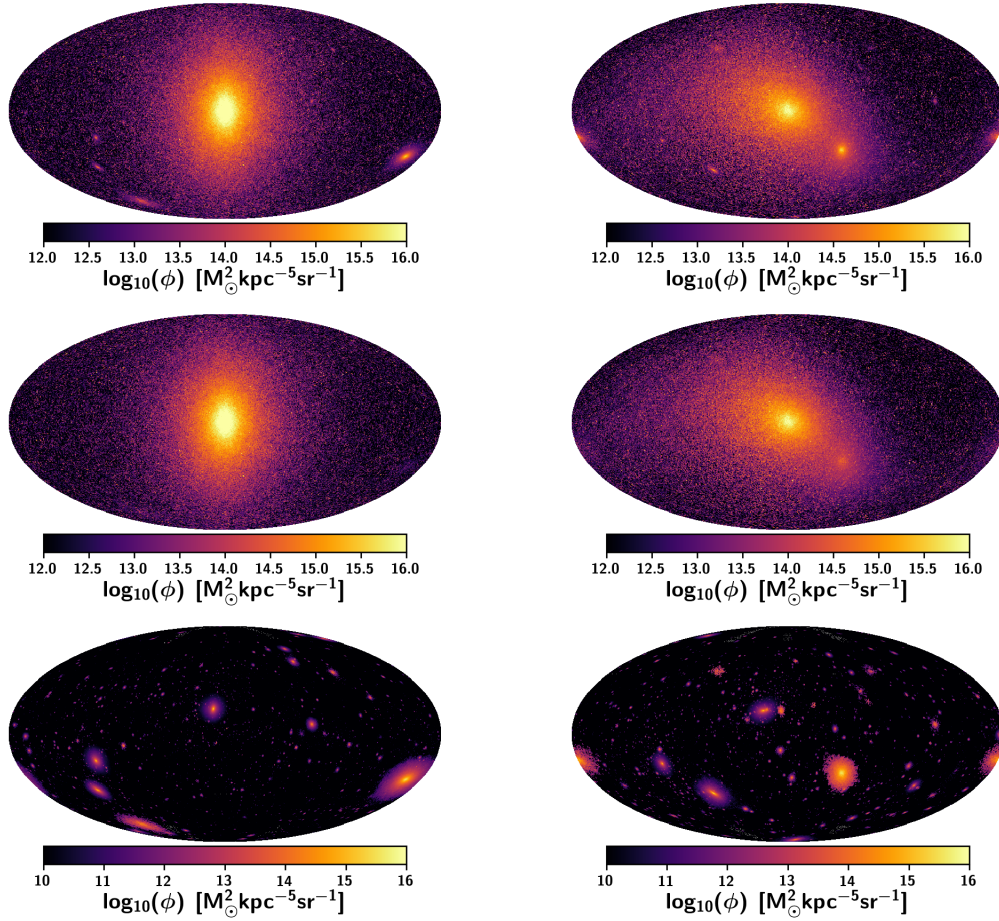


FIGURE 3.4: Example of all-sky maps for galaxy ‘G9’ of the annihilation flux per solid angle with an observer placed at the ‘solar neighborhood’, i.e., ≈ 8.5 kpc from the GC (for reference, for G9, R_{200} is $\simeq 215$ kpc). Left panels correspond to hydro and right panels to DMO simulations, respectively. The images from the top to bottom correspond to total flux emission, emission from the host halo only, and emission from substructure only, respectively. Note the change in the colourbar scale in the bottom images.

hydro subhalos start to dominate slightly. However, the annihilation fluxes of host halos are significantly higher than those of subhalos, compared with the differences seen in the case of luminosities. This can be explained by the closer location of the centres of these hosts to the observer (located in the ‘solar neighborhood’), than the typical subhalo.

The lower panel in Fig. 3.5 shows the ratio of the boosted annihilation fluxes, $F_{\text{hydro}}/F_{\text{DMO}}$. As in the case of luminosities, we see that the fluxes are higher in the case where baryons are present, for subhalo higher masses ($M_{\text{sub}} > 10^{10}M_{\odot}$). However, in this case there are significant fluctuations in this ratio at higher masses (e.g., at $M_{\text{sub}} \simeq 4 \times 10^{10}M_{\odot}$).

These are caused by the lower number of high mass subhalos combined with the large variations in their distances from the observer.

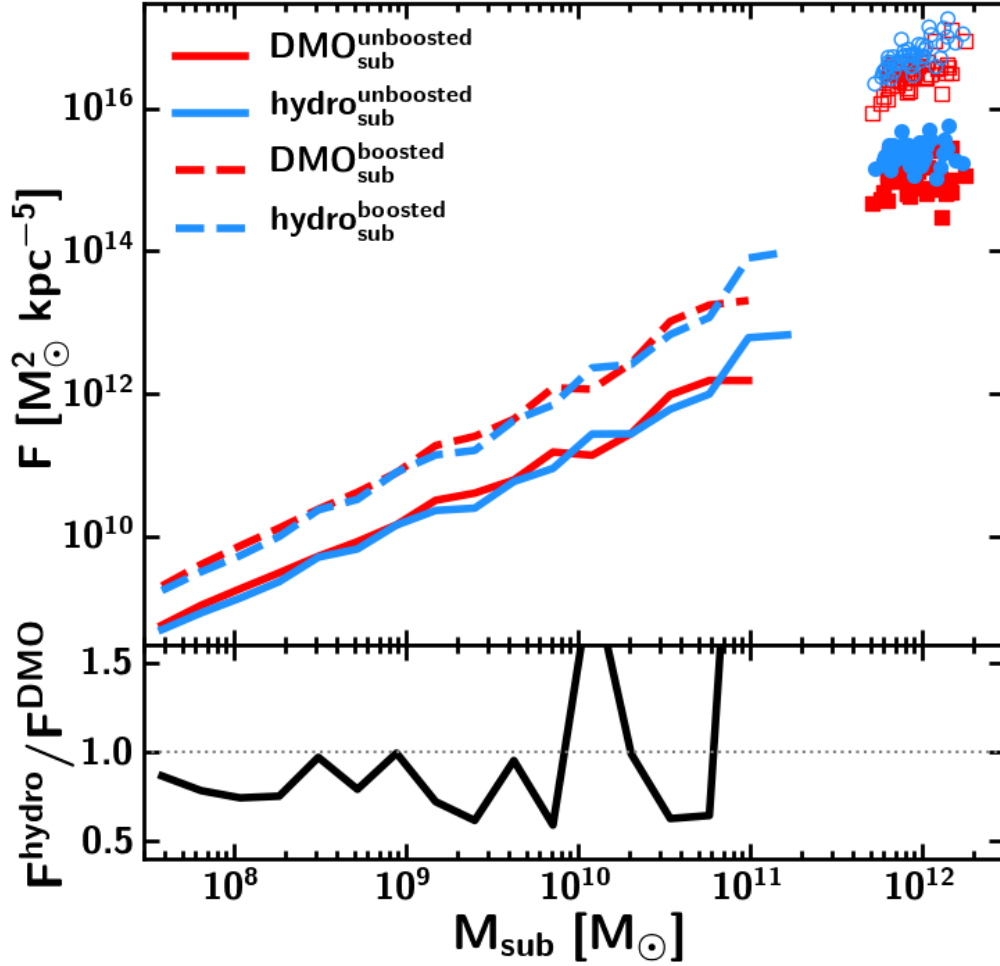


FIGURE 3.5: *Top*: Dark matter annihilation flux as a function of subhalo mass for all subhalos in the simulations. The dashed lines represent the median flux of the boosted DMO (red) and hydro (blue) subhalos, using our fiducial model (see text for details). The solid lines show the median flux of the unboosted DMO (red) and hydro (blue) subhalos. The filled and empty circles and squares represent the unboosted and boosted annihilation flux for the individual DMO (red) and hydro (blue) host halos. *Bottom*: The ratio of median hydro and DMO annihilation fluxes for the boosted subhalos.

The top panel of Fig. 3.6 shows the distribution of subhalo masses, M_{sub} and distances from the observer, d , colour-coded by the total annihilation fluxes. The boost factors are included in these fluxes. As expected, the fluxes are higher for more massive subhalos and/or those that are closer to the observer. Interestingly, we can see also in a more

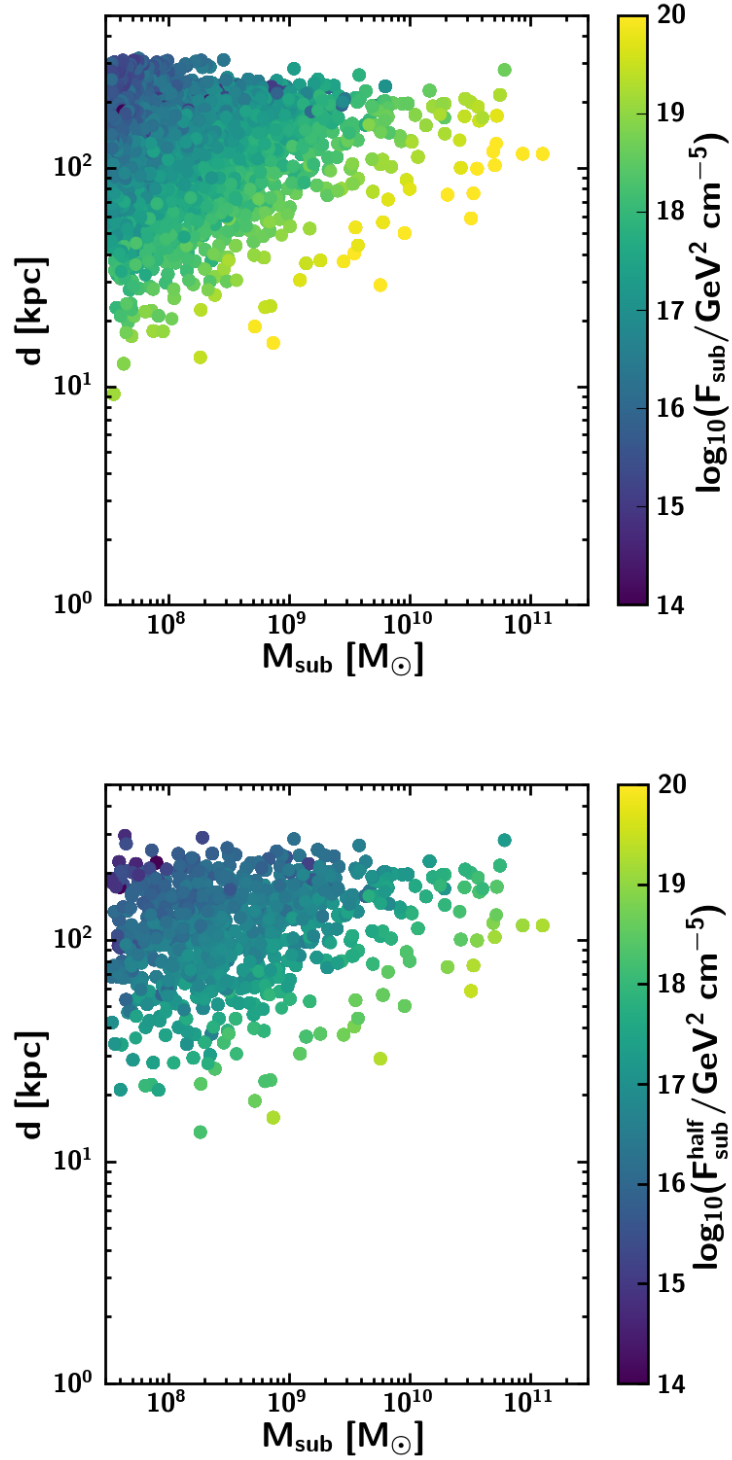


FIGURE 3.6: *Top*: Subhalo mass as a function of distance to the observer, coloured by annihilation flux calculated from all particles in the subhalo. *Bottom*: The same, but using the annihilation flux within the half-light radius (hence considering only luminous dwarf systems).

quantitative way how distance comes into play in the flux values; for example, in the range F_{sub} of $10^{18} - 10^{19} \text{ GeV}^2 \text{ cm}^{-5}$, lower mass subhalos with total masses $M_{\text{sub}} \approx 10^8 M_{\odot}$ and located nearby, $d \lesssim 30 \text{ kpc}$, generate similar DM annihilation fluxes as more massive subhalos located far-away, e.g., subhalos with $M_{\text{sub}} \approx 10^{10} M_{\odot}$ at $d > 100 \text{ kpc}$. This underscores the importance of the nearness of a DM subhalo to the observer in terms of the detectability of its signal.

The fluxes examined so far are those generated by entire (sub)halos, i.e., summed up over DM particles within R_{sub} . However, the extent of a DM subhalo is difficult to estimate from observations. For this reason, many predictions for DM annihilation signals from dwarf galaxies use the effective (or half-light) radius as a reference. We therefore compute fluxes within half-light radii (r_{h}) as well. Specifically, we take r_{h} as the projected (2D) radius that encloses half of the total V -band luminosity of a dwarf galaxy, provided that the DM subhalo harbours a stellar component. The V -band luminosities are computed from simple stellar populations models and adopting the stellar initial mass function used in the simulations (see [Font et al. 2020](#) for details).

The bottom panel of Fig. 3.6 shows again the distribution of subhalo masses and distances from the observer, this time colour-coded by the fluxes computed within r_{h} . These fluxes include the boost factors also. The trends are similar to those seen in the left panel (note that the total masses and distances have not changed, only the values of the fluxes). We also find that the fluxes computed within r_{h} are generally quite similar with those computed within R_{sub} (the latter are higher but within an order of magnitude). This implies that most of the flux emitted from subhalos originates from within r_{h} . This is not surprising, as the DM densities are higher near the centre, and the outer regions of the subhalo are expected to not contribute much to the total annihilation flux. This suggests also that the measurements of fluxes within half-light radii are appropriate. On the other hand, a comparison between the top and bottom panels of Fig. 3.6 shows, targeting only luminous dwarf galaxies has some limitations, as it misses a range of potential sources of DM annihilation, such as dark subhalos nearby (note though that these would not be detectable on their own, but they can contribute to a stacked signal).

The nearby luminous dwarf galaxies have been studied before in terms of their potential for generating DM annihilation fluxes. For example, Charbonnier et al. (2011) estimated that the fluxes within r_h for the classical dwarf galaxies (known also as the J -factors) of $\sim 10^{10} - 10^{12} M_\odot^2 \text{ kpc}^{-5}$ (or, equivalently, $\sim 10^{16} - 10^{18} \text{ GeV}^2 \text{ cm}^{-5}$), with the highest flux predicted to originate from Ursa Minor. These values are broadly in agreement with our estimated fluxes (within r_h) for the simulated ‘analogs’ of classical dwarfs (see bottom panel of Fig. 3.6).

To summarise our results from this section, we find that the MW-mass halos emit the greatest fluxes, given their high DM masses and their proximity to the observer. The higher mass subhalos ($M_{\text{sub}} > 10^7 M_\odot$) are also significant sources of annihilation flux, however there is a large region of the (M_{sub}, d) parameter space that generate similar fluxes. Additionally, with the inclusion of baryons in the simulations the annihilation fluxes are slightly higher, especially for MW-mass halos and at the high subhalo mass end. This reiterates the necessity of using hydrodynamical simulations for providing accurate γ -ray flux predictions.

3.5 Detectability of dark matter annihilation

So far we have investigated the DM annihilation luminosities and fluxes in simulations, focusing mainly on the differences between host halos and substructure, or the differences between hydrodynamical and DM-only simulations. However, real DM indirect detection experiments have their own instrumental limitations that can affect these predictions. Here we take the next step in estimating the detectability of DM annihilation signal using the expected sensitivity from the CTA.

The CTA will be the first ground-based IACT able to observe almost the entire sky, using array sites on both the northern and southern hemispheres. The CTA will consist of three differently sized telescopes, each sensitive to different energy ranges, covering the γ -ray spectrum in the 20 GeV – 300 TeV range. With the improved capabilities of CTA there is a possibility that it can be used to study the less explored faint dwarf galaxies or even dark subhalos. Using the simulated MW-mass halos and DM subhalos in ARTEMIS,

we aim to evaluate their differential γ -ray flux sensitivity and determine whether the CTA is sensitive enough to detect the signal from their potential DM annihilations.

The differential γ -ray flux is used to evaluate the sensitivity of the γ -ray experiments to DM annihilations and can be written as,

$$\frac{d\phi_\gamma}{dE} = \frac{\langle\sigma v\rangle}{8\pi m_\chi^2} \frac{dN_\gamma}{dE} F, \quad (3.9)$$

where m_χ is the mass of the DM particle, $\langle\sigma v\rangle$ is the velocity-averaged DM annihilation cross-section and dN_γ/dE is the γ -ray spectrum generated from a single annihilation. Henceforth, we assume $\langle\sigma v\rangle = 3 \times 10^{-26} \text{ cm}^3 \text{ s}^{-1}$, which is the thermally averaged annihilation cross-section of WIMP particles that correctly reproduces the DM relic abundance seen today (see, e.g., [Steigman et al., 2012](#)). The flux values, F , are computed from the simulations. For the following, we use only fluxes that already include the boost factor. By default, we use the L16 c–M relation, although we will also compare the results using the relation of D19, to show predictions in a less conservative case.

To evaluate the right-hand-side of eq. 3.9, we need an assumption for the DM particle mass (see below), and to evaluate the γ -ray spectrum, dN_γ/dE . For the latter, we use the publicly available package `DarkSUSY` ([Gondolo et al., 2004](#); [Bringmann et al., 2018](#)), designed to compute supersymmetric DM properties numerically. In particular, we make use of the ‘*wimpyields*’ function to calculate the yields of different particles from the decay/hadronization of annihilation products². To generate dN_γ/dE we assume that the DM annihilates into a γ -ray final state via either a $b\bar{b}$, $t\bar{t}$ or $\tau^+\tau^-$ annihilation channel, with a 100% branching ratio. Appendix 3.7.1 shows the γ -ray spectrum from `DarkSUSY`, dN_γ/dE , for the three annihilation channels studied here, as well as for different assumptions of WIMP masses.

The differential γ -ray fluxes (multiplied by E^2) for the simulated MW-mass host halos and their DM subhalos are shown with dashed lines in Fig. 3.7. The left and right

²See `DarkSUSY` user manual for a full description of all functions and routines; <https://darksusy.hepforge.org/pdf/Manual.pdf>

columns show the same results, but assuming different c – M relations, the L16 on the left and the D19 relation on the right. Again, we show results separately for the host halos in the hydro (blue) and DMO simulations (red), as well as for all substructure (i.e., sum over all DM subhalos) in the respective simulations (gold lines for hydro and purple for DMO). In this figure we assume that the DM particle is a WIMP with mass $m_\chi = 1$ TeV, but below we also investigate different DM particle masses. We also explore the annihilation via three different channels: $b\bar{b}$ (top rows), $t\bar{t}$ (middle) and $\tau^+\tau^-$ (bottom). In all panels, the solid black lines indicate the predicted flux sensitivities for a nominal 50 hour observation with the North³ site of the CTA (that is, any fluxes above these lines may be detectable).

We discuss first the detectability of the signal from MW-mass hosts. From Fig. 3.7 it is clear that the MW-mass halos in the simulations with baryons lead to a higher flux sensitivity than their DMO counterparts (compare blue and red dashed lines). This is true for all annihilation channels and across all energies examined here. The higher flux sensitivities of hydro main halos are just the result of their higher DM densities in these halos (caused by adiabatic contraction, as discussed before), which leads to an increase of their fluxes all the way through their flux sensitivities. The choice of the c – M relation also has an effect on the differential γ -ray fluxes, for example the D19 relation leads to an increase by a factor of ~ 10 over the L16 relation. This is because the D19 c – M relation provides a larger boost factor, as shown in Fig. 3.2.

This figure also implies a 50-hour observation with the CTA towards the centre of the Milky Way is sensitive enough to detect a DM annihilation signal, if this signal occurs at energies between ~ 20 GeV – 1 TeV, in one of three annihilation channels examined here.

The median differential γ -ray fluxes of substructure do not show significant differences between the hydro and DMO runs (compare the gold and purple lines in Fig. 3.7), in contrast with what it was found for the main halos. This suggests that baryonic effects are not important in this case. Interestingly the detectability of differential γ -ray fluxes from (the stacked) DM subhalos depends crucially on the type of annihilation channel

³We checked that the results for the South site of the CTA are similar.

and energy range surveyed, while the predictions also depend strongly on the assumed c – M relation. For example, assuming the L16 relation, the differential γ -ray fluxes via the $b\bar{b}$ and $t\bar{t}$ channels lie below the sensitivity limit of the 50-hour CTA observation (and only slightly so for the energy range $\sim 100 - 300$ GeV). On the other hand, for the $\tau^+\tau^-$ annihilation channel the differential flux lies above this CTA sensitivity limit, albeit only for a small energy range, of $\sim 200 - 700$ GeV.

In the case of substructure, adopting the D19 relation⁴ leads to an increase by a factor of ~ 5 in the (stacked) DM subhalo differential γ -ray fluxes, compared with using the L16 relation. This increase improves the detectability of the substructure signal significantly, now the signal being generally either on or slightly above the CTA North 50 hour detection limit, e.g. around the 10–20 GeV energy range in the case of $b\bar{b}$ and $t\bar{t}$ channels and over 10 GeV – 1 TeV range in the case of $\tau^+\tau^-$ (in the latter case, with increased sensitivity also). It is plausible that an increase in the observing time of the CTA could improve the detectability of these signals even more.

So far we have focused on a fixed DM particle mass of $m_\chi = 1$ TeV, to exemplify the expected variations in detectability by in different annihilation channels and by changing the assumed c – M relation. However, the range of plausible WIMP masses is rather large in theory. Below we investigate how different m_χ values affect the detectability of the annihilation signal, using the same nominal CTA North 50-hour observing time. Specifically, we use three additional values of m_χ , of 500 GeV, 10 TeV and 100 TeV. These choices are made to exemplify how predictions change with different assumed particle masses, and therefore are not unique (the predictions will change in detail, but not in terms of the general trends if other similar values are chosen). The effects on the differential γ -ray fluxes for these three different WIMP masses are shown in Fig. 3.8. As in Fig. 3.7, we examine the role of the c – M relation separately, by adopting the L16 relation in the left column and the D19 one in the right column, respectively.

First, as m_χ increases the differential flux sensitivity decreases. As in Fig. 3.7, the annihilation signal from the main MW-mass halos is above the CTA 50h sensitivity

⁴Although we focus here on the D19 c – M relation, we note that other choices of the c – M relation will give similar results, for example the B01 relation, which generates similar boost factors as D19 (see Fig. 3.2).

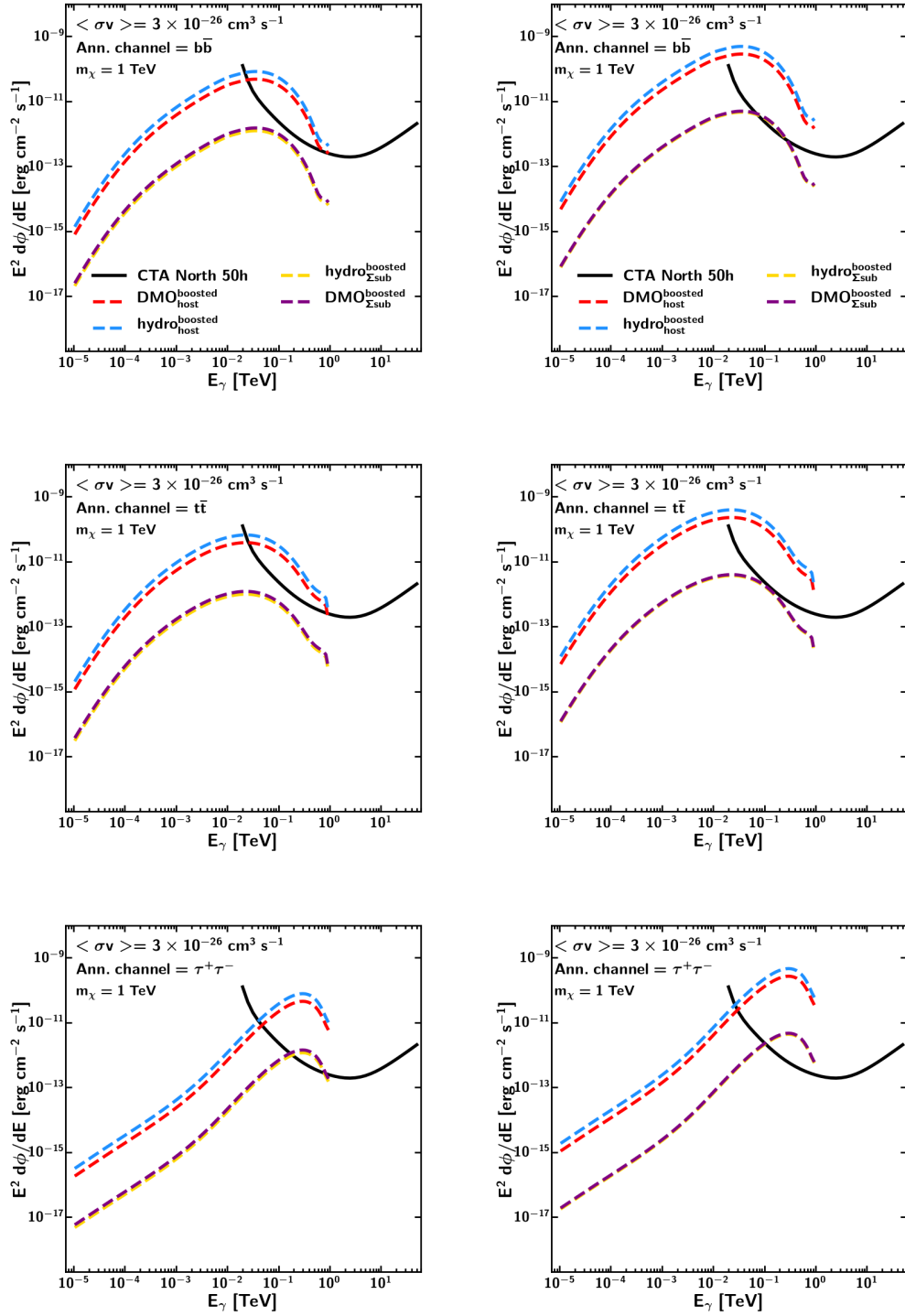


FIGURE 3.7: *Left panels:* Differential γ -ray flux sensitivity ($\times E^2$) for WIMPs of mass $m_\chi = 1$ TeV, annihilating with $\langle\sigma v\rangle = 3 \times 10^{-26}$ cm 3 s $^{-1}$ into various channels (*top* panel shows the $b\bar{b}$ channel; *middle:* $t\bar{t}$; and *bottom:* the $\tau^+\tau^-$ channel). The dashed lines represent the median differential γ -ray flux for the boosted host halos in the DMO run (red), host halos in the hydro run (blue), summed DM subhalos in the DMO run (purple) and the summed DM subhalos in the hydro run (gold). The solid black line shows the predicted flux sensitivity for a 50 hour observation with the North site of the CTA. *Right panels:* Same as on the left panels, but using the c–M (D19) relation.

limit, regardless of the particle mass and/or choice of c – M relation. The signals from the stacked DM subhalos are below the limit of CTA detection when using the L16 relation. However, using the D19 relation improves again the detectability, leading to a possible detection for $m_\chi = 500$ GeV around the 10 GeV energy range via the $b\bar{b}$ channel, and for a $m_\chi = 10$ TeV particle around the 1 TeV range via the $t\bar{t}$ channel. The $\tau^+\tau^-$ channel does not lead to a possible detection of substructure for the m_χ values studied here.

As we have shown above, the detectability of a DM annihilation signal depends sensitively on a number of factors. Besides the annihilation luminosity and flux discussed in Sections 3.3 and 3.4, the properties of the DM particle (e.g., its mass) and the specific (CTA) instrumental limitations play an important role. The unknown mass of the WIMP is a cause of uncertainty when predicting a DM annihilation signal, causing the detection energy range to vary by several orders of magnitude (see Fig. 3.8). One of the largest uncertainties in the detectability of DM indirect detection predictions comes from the assumed $c - M$ relation in computing the boost factors of the unresolved substructure. We have shown that varying the $c - M$ relation can change the differential γ -ray flux by a factor of ~ 10 in the case of the main MW halo or by a factor of ~ 5 in the case of the substructure. For some models, and specifically for subhalos, it makes the difference between being detectable or undetectable.

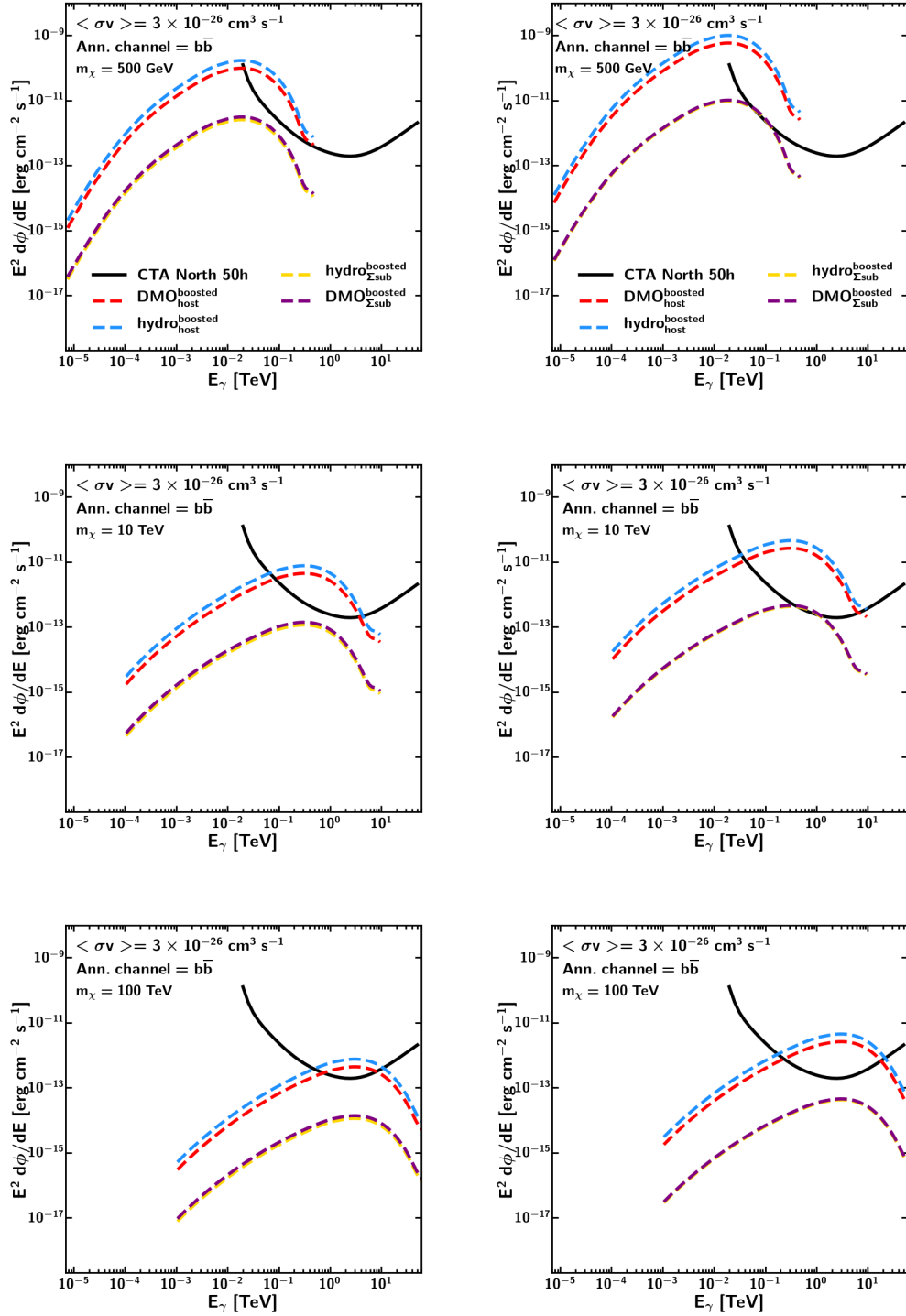


FIGURE 3.8: Left panels: The differential γ -ray flux sensitivity ($\times E^2$) for WIMPs of masses $m_\chi = 500$ GeV, 10 TeV and 100 TeV, respectively. All panels correspond to annihilations in the $b\bar{b}$ channel and assuming $\langle\sigma v\rangle = 3 \times 10^{-26} \text{ cm}^3 \text{ s}^{-1}$. All lines have the same meaning as in the left panels of Fig. 3.7. Right panels: Same as on the left, but for the c-M (D19) relation.

3.6 Conclusions

Using a large suite of cosmological simulations of the formation of MW-mass systems (ARTEMIS), we have investigated the prospects of indirect DM detection in the GCs of these DM halos and in their neighboring DM subhalos by the upcoming CTA. Having at our disposal samples of MW-mass DM halos and subhalos followed both with hydrodynamics and only with dynamics of DM, we were able to estimate the role of baryonic physics in the detectability of the DM annihilation signal, studying its effects on the annihilation luminosities and fluxes, as well as on the γ -ray flux sensitivity with CTA. We studied the limits of main MW-mass halos and substructure separately in hydro and DMO simulations, the changes induced by different assumed c - M relations in the calculations of boost factors, and the effect of different annihilation channels and of different WIMP particle masses. Our main findings are:

1. The baryonic physics matters most for the prospects of the detectability in the main MW-mass DM halos (i.e., the centre of the Milky Way). In particular, the hydro simulations obtain higher DM annihilation luminosities and fluxes for the main halos compared with the DMO simulations. This is because baryons induce adiabatic contraction of DM halos leading to higher central densities. This highlights the importance of using hydrodynamical simulations for predictions of signals at the GC. For the DM substructure, the inclusion of baryons does not change the magnitude of individual annihilation luminosities or fluxes of DM subhalos, but it has the effect of reducing the abundance of surviving subhalos, thus lowering the overall (stacked) signal.
2. We have estimated the DM annihilation fluxes inside half-light radii for the simulated DM subhalos that contain baryons and found that the results are comparable to previous predictions for local dwarf galaxies in the Milky Way that used observed values of half-light radii and analytical modeling. Specifically, obtaining DM subhalo fluxes of $\sim 10^8 - 10^{13} M_{\odot}^2 \text{ kpc}^{-5}$ ($\sim 10^{14} - 10^{19} \text{ GeV}^2 \text{ cm}^{-5}$). More massive subhalos that are nearby have the highest fluxes. There is also a wide degeneracy between the masses of DM subhalos and their distances from

the observer in the intermediate flux range. Note, however, that no individual DM subhalo has a sufficiently stronger γ -ray flux to be detected on its own, rather the strategy for substructure need to include a global approach, e.g. by stacking the signal.

3. Using the current estimates of CTA flux sensitivity for a 50-hour observing time, and assuming a WIMP mass of 1 TeV, we find that the detector would be sensitive enough to detect the DM annihilation signal from the main MW DM halo via either $b\bar{b}$, $t\bar{t}$ or $\tau^+\tau^-$ annihilation channels, in the energy range of ~ 20 GeV – 1 TeV. The predicted signal depends on the assumed c–M relation, with the D19 relation giving higher annihilation fluxes (by a factor of ~ 10) than the L16 one (although both signals are above the estimated CTA detection limit).
4. The detectability of the DM annihilation signal from the (summed) DM substructure (using a fixed WIMP mass of 1 TeV), depends strongly on the assumed c–M relation, in some cases making the difference between the substructure being detected or not. Assuming the L16 relation, the signal lies below the sensitivity limit of CTA (although it can become detectable in the energy range of $\sim 100 - 300$ GeV via the $b\bar{b}$ and $t\bar{t}$ channels if the CTA observing time were to be increased). For the $\tau^+\tau^-$ annihilation channel the differential γ -ray flux above the CTA sensitivity limit for a small energy range of $\sim 200 - 700$ GeV. If CTA were to observe for a longer period the boosted subhalo may be detectable at ~ 100 GeV for all annihilation channels. Interestingly, however, if one assumes the D19 relation (or any other similar relation that provides higher boost factors), the signal from the DM substructure has better chances of being detected by CTA. In particular, for a WIMP mass of 1 TeV, the signal may be detected around 10 GeV in the $b\bar{b}$ or $t\bar{t}$ channels.
5. We have explored also how the predicted signal changes with other WIMP masses, i.e., $m_\chi = 500$ GeV, 10 TeV and 100 TeV. In all cases, and for all annihilation channels, the signal from the main MW-mass halos remains above the CTA detectability limit. For substructure, however, the predictions depend sensitively

on m_χ , with less energetic particles (i.e., $\lesssim 10$ TeV) being (just marginally) detectable by CTA.

3.7 Appendix

3.7.1 The γ -ray spectrum using DarkSUSY

Fig. 3.9 shows the γ -ray spectrum dN_γ/dE computed with the `DarkSUSY` package, for three annihilation channels. For each channel, we also show results for different choices of the WIMP mass, specifically for $m_\chi = 500$ GeV, 1 TeV, 10 TeV and 100 TeV. For all three annihilation channels the spectrum shifts to lower WIMP yields at high energies as the value of m_χ is increased.

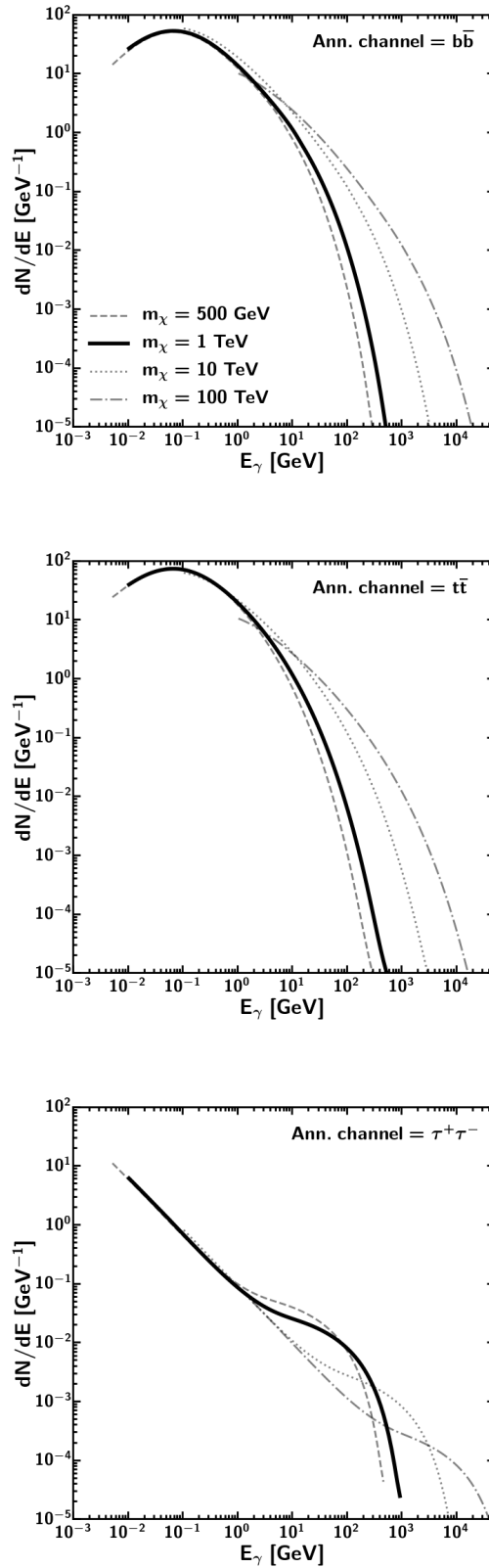


FIGURE 3.9: The γ -ray spectrum dN_γ/dE for varying WIMP masses, m_χ from 500 GeV – 100 TeV, computed with DarkSUSY. From top to bottom we show results for the different annihilation channels: the $b\bar{b}$, $t\bar{t}$ and $\tau^+\tau^-$ channels, respectively.

Chapter 4

Conclusions and future directions

4.1 Summary

The aim of this thesis has been to make a meaningful contribution towards the understanding of the impact of baryons and uncertainties involved with direct and indirect DM detection experiments. The necessity to understand and model the uncertainties associated with both direct and indirect DM detection is essential to increase our chances of detecting DM. Additionally, understanding the role the baryons physics plays in cosmological simulations allows for more precise predictions of a DM annihilation signal. The positive detection of DM will lead to a new era in physics and astrophysics, advancing our understanding of the Universe on all scales.

In Chapter 1, the context of the work in this thesis was introduced. Initially, the current standard model of cosmology, Λ CDM, is explained. This was followed by an introduction to DM, briefly describing the observations supporting its existence. The constraints that a DM particle candidate had to satisfy were discussed and several contenders examined, including WIMPs. Both direct and indirect DM detection techniques were then explored. Finally, a brief discussion of cosmological simulations allowed the introduction of the ARTEMIS simulations, which are used in this thesis.

4.1.1 Direct detection

In Chapter 2, the uncertainties associated with DM direct detection experiments were investigated. DM direct detection experiments aim to place constraints on the DM–nucleon scattering cross-section and the DM particle mass. These constraints depend sensitively on the assumed local DM density and velocity distribution function. While astrophysical observations can inform the former (in a model-dependent way), the latter is not directly accessible with observations. Using the high-resolution ARTEMIS cosmological hydrodynamical simulation suite of 42 Milky Way-mass halos to explore the spatial and kinematical distributions of the DM in the solar neighbourhood, how these quantities are influenced by substructures, baryons, the presence of dark discs, as well as general halo-to-halo scatter (cosmic variance) were investigated. Using these results, estimations of the uncertainties in the WIMP cross-section limits for the LZ and XENON1T direct detection experiments, under the assumption of a WIMP-nucleon spin-independent elastic scattering were made. The main results are described below:

- The range in local parameters, ρ_0 , v_0 , v_{esc} , in the ARTEMIS simulations were studied to inform how the SHM should be implemented in direct detection techniques. These values were found to be generally in good agreement with observations, within the observational uncertainties. The most influential local parameter, ρ_0 (typically assumed to be $0.3 - 0.4 \text{ GeV cm}^{-5}$), ranges between $0.15 - 0.48 \text{ GeV cm}^{-5}$ and $0.10 - 0.38 \text{ GeV cm}^{-5}$ in the hydro and DMO simulations respectively (see Fig. 2.2). The increased values of ρ_0 in the hydro simulations relative to the DMO simulations are likely to be caused by adiabatic contraction due to the presence of baryons.
- Generally, the local DM velocity distribution is assumed to be a simple Maxwellian distribution and is adopted in the SHM. The median local DM velocity distribution determined from the ARTEMIS simulations is relatively well described by a Maxwellian for the hydro halos, but less so for the DMO halos (see Fig. 2.3). The adiabatic contraction in the presence of baryons causes an increase in the peak velocities, v_0 , with the hydro halos v_0 typically 30 kms^{-1} higher than their DMO counterparts.

- Substructures, such as subhalos and streams, can pass inside the solar neighbourhood (Fig. 2.6) influencing the DM detectability rates. However, this does not often occur in the cosmological context for relatively high-mass substructures and therefore are unlikely to significantly affect direct detection rates. Dark discs, however, are found in a relatively large proportion of the ARTEMIS hydro halos. A conservative estimate is, $\approx 15\%$ of our sample has dark discs, but the fraction can be as high as $\approx 36\%$ (Fig. 2.11) depending on how one defines a dark disc. The presence of dark discs increases the local DM density, ρ_0 , and can also lead to significant deviations from Maxwellian velocity distribution.
- The enhanced DM densities and peak velocities in hydro simulations relative to DMO simulations lead to higher differential scattering rates in the former when adopting the SHM. Therefore, the hydro simulations have lower exclusion limits on the WIMP-nucleon cross-section (Fig. 2.14). In addition, the halo-to-halo scatter in the implied exclusion limits (due to scatter in the density and velocity distributions) is relatively large; typically by a factor ≈ 1.5 and increasing towards lower WIMP masses. The halo-to-halo scatter in the exclusion limits is only slightly smaller than the experimental uncertainties on the published XENON1T and LZ (projected) direct detection limits. In fact, at low WIMP masses ($< 20 \text{ GeV } c^{-2}$) the simulation-based scatter typically exceeds the experimental uncertainty. Using these results we can conclude that the astrophysical systematic uncertainties should be included as part of the overall error budget for DM direct detection experiments. This is very important both for deriving a conservative estimate on the cross-section limits and for when comparisons are made to constraints on DM properties derived from indirect and collider searches.
- Rather than adopting a Maxwellian velocity distribution from the SHM, we found that an empirical form for $f(\vec{v})$ slightly lowers the exclusion limits. The most significant difference is seen at WIMP mass $< 100 \text{ GeV } c^{-2}$ (Fig. 2.15). This suggests that the use of a Maxwellian form in the SHM generally puts a conservative limit on the exclusion limits compared with a more realistic model for the velocity distribution at masses of $< 100 \text{ GeV}$ (at higher masses, the opposite is true). This

shows that any slight deviation from a Maxwellian affects the predicted exclusion limits, increasing uncertainly in DM direct detection models.

4.1.2 Indirect detection

After investigating DM direct detection, DM indirect detection was explored in Chapter 3. Here, the effect baryons have on the detection of DM via self-annihilation using Milky Way-like galaxies from the ARTEMIS simulations, as well as their respective subhalos (dwarf galaxies) was studied. The focus was on the annihilation luminosities and fluxes from host and subhalos for DMO and hydro cases, and whether the resulting annihilation signature would be detectable by the CTA, a next-generation IACT. The importance of unresolved substructure for the smooth (unboosted) annihilation luminosities and fluxes by employing a ‘boost’ factor was also investigated, as well as the associated uncertainties. The main results are described below:

- The baryonic physics matters most for the prospects of the detectability in the main MW-mass DM halos (i.e., the centre of the Milky Way). In particular, we find that the hydro simulations obtain higher DM annihilation luminosities and fluxes for the main halos compared with the DMO counterparts. This is caused by the baryons inducing adiabatic contraction of DM halos, which leads to higher densities in the centre of the halos. This highlights the importance of using hydrodynamical simulations for predictions of signals at the GC. For the DM substructure, the inclusion of baryons does not change the magnitude of individual annihilation luminosities or fluxes of DM subhalos, but it does have the effect of reducing the abundance of surviving subhalos, thus lowering the overall (stacked) DM annihilation signal.
- We have estimated the DM annihilation fluxes within the half-light radii for the simulated DM subhalos that contain baryons and found that the results are comparable to previous predictions for local dwarf galaxies in the Milky Way that used observed values of half-light radii and analytical modeling. Specifically, we find that the DM subhalo fluxes are in the range of $\sim 10^8 - 10^{13} M_{\odot}^2 \text{ kpc}^{-5}$

($\sim 10^{14} - 10^{19} \text{ GeV}^2 \text{ cm}^{-5}$). The more massive a subhalo is and the closer it is to an observer/detector, the higher the fluxes. There is also a wide degeneracy between the masses of DM subhalos and their distances from the observer in the intermediate flux range. However, we find that no individual DM subhalo has a sufficiently stronger γ -ray flux to be detected on its own, rather we advocate that the strategy for detecting a DM annihilation signal from substructure requires a global approach, e.g. by stacking the signal.

- Using the current estimates of CTA flux sensitivity for a 50-hour observing time, and assuming a WIMP mass of 1 TeV, we find that the detector would be sensitive enough to detect the DM annihilation signal from the main MW DM halo via either $b\bar{b}$, $t\bar{t}$ or $\tau^+\tau^-$ annihilation channels, in the energy range of $\sim 20 \text{ GeV} - 1 \text{ TeV}$. The predicted signal depends on the assumed c–M relation, with the D19 relation giving higher annihilation fluxes (by a factor of ~ 10) than the L16 one, this is due to D19 prediction of higher concentrations (although both signals are above the estimated CTA detection limit).
- The detectability of the DM annihilation signal from the (summed) DM substructure (using a fixed WIMP mass of 1 TeV), depends strongly on the assumed c–M relation, in some cases making the difference between the signal originating from the substructure being detected or not. Assuming the L16 relation, the signal lies below the sensitivity limit of CTA (although it can become detectable in the energy range of $\sim 100 - 300 \text{ GeV}$ via the $b\bar{b}$ and $t\bar{t}$ channels if the CTA observing time were to be increased). For the $\tau^+\tau^-$ annihilation channel the differential γ -ray flux above the CTA sensitivity limit for a small energy range of $\sim 200 - 700 \text{ GeV}$. If CTA were to observe for a longer period the boosted subhalo may be detectable at $\sim 100 \text{ GeV}$ for all annihilation channels. Interestingly, however, if one assumes the D19 relation (or any other similar relation that provides higher boost factors), the signal from the DM substructure has better chances of being detected by CTA. In particular, for a WIMP mass of 1 TeV, the signal may be detected around 10 GeV in the $b\bar{b}$ or $t\bar{t}$ channels.

- We have also explored how changes in the mass of the WIMP affects the annihilation signal, i.e., $m_\chi = 500 \text{ GeV}$, 10 TeV and 100 TeV . For all WIMP masses investigated, and for all annihilation channels, the signal from the main MW-mass halos remains above the CTA detectability limit. For substructure, the predictions depend sensitively on m_χ , with less energetic particles (i.e., $\lesssim 10 \text{ TeV}$) being (just marginally) detectable by CTA.

4.2 Future directions and implications

The results of this thesis play a very important role in our effort to understand DM and its detection, both directly and indirectly.

Since the completion of the work presented in Chapter 2, three Milky Way-like halos have been added to the ARTEMIS suite of simulations. As mentioned in Section 2.2.1, the stellar masses of the ARTEMIS Milky Way-like galaxies are on the lower end of its observed mass range, including these three newly generated halos would populate the higher stellar masses, possibly improving our predictions.

As discussed in Section 2.3.2, the impact of substructure on the direct detection of DM in the solar neighbourhood is of great importance. The increased DM density that may be provided by a DM clump or stream is likely to increase the DM detection signal. With observations of the Milky Way becoming more precise, new structures are being discovered, such as the Sagittarius stream, the *Gaia* sausage, Nyx stream, and the S1 and S2 streams, all of which may increase DM detection probabilities. Future observations from *Gaia* and others are likely to detect more of these features in the Milky Way and solar neighbourhood. Ever-advancing direct detection experiments with their increased sensitivity, in particular those directional experiments, are forever improving the chances of a positive DM detection.

When completed, the CTA will play an extremely important role in exploring the currently inaccessible energies for detecting some of the best-motivated WIMP models. Searches for a DM annihilation signal in the form of γ -rays from both the Galactic

Centre and satellite galaxies are a key target for the project. Based on the work in this thesis, their current γ -ray sensitivity predictions are on the borderline of being able to positively detect a DM annihilation signal from Milky Way satellite galaxies. Going forward, if CTA wishes to improve its chances of positive detection of DM in either the Galactic Centre or the Milky Way satellites, one possibility would be for it to increase its planned 50 hours of observation time.

With the advancement of direct and indirect detection experiments and the ever-improving constraints placed on the physical properties of DM, in particular the WIMP, the way in which the experimental and astrophysical uncertainties are handled is of great importance. As shown in this thesis, a key point that must be emphasised is that the predictions made by these experiments are based on models with a significant degree of uncertainty and several assumptions about the nature of DM, all of which must be taken into account. If not handled correctly, these uncertainties may cause direct detection experiments to insufficiently probe the WIMP parameter space.

Within the next 10 years we should have a definitive answer to the question; is DM a WIMP-like particle? Both direct and indirect detection experiments will be hitting the limits on the WIMP parameter space having explored all realistic particle masses and energies. For example, the planned forthcoming XENONnT ([Aprile et al., 2020](#)) and DARWIN ([Aalbers et al., 2016](#)) direct detection experiments will explore WIMP cross-section limits beyond the neutrino discovery limit, at which point any DM signal would be indistinguishable from the signal produced by coherent neutrino scattering. With the possibility of a high mass DM particle candidate looking less likely, the low mass end of the parameter space is being tested. In particular, the recent interest in axion DM is gathering pace, with the Axion Dark Matter eXperiment (ADMX) ([Du et al., 2018](#)) searching for microwave photons emitted from the local galactic DM halo.

To this day, the nature of DM remains the biggest unsolved mystery in astrophysics. The work in this thesis has added to our understanding of how to model and predict the wide range of uncertainties in our attempt to detect the elusive DM particle.

Bibliography

- Aalbers J., et al., 2016, *J. Cosmology Astropart. Phys.*, 2016, 017
- Aalseth C. E., et al., 2008, *Phys. Rev. Lett.*, 101, 251301
- Aaronson M., 1983, *ApJ*, 266, L11
- Aarseth S. J., 1963, *Monthly Notices of the Royal Astronomical Society*, 126, 223
- Abazajian K. N., et al., 2012, arXiv e-prints, p. arXiv:1204.5379
- Acharyya A., et al., 2021, *J. Cosmology Astropart. Phys.*, 2021, 057
- Ackermann M., et al., 2011, *Phys. Rev. Lett.*, 107, 241302
- Ackermann M., et al., 2014, *Phys. Rev. D*, 89, 042001
- Ackermann M., et al., 2017, *The Astrophysical Journal*, 840, 43
- Ahmed Z., et al., 2009, *Phys. Rev. Lett.*, 102, 011301
- Akerib D. S., et al., 2003, *Phys. Rev. D*, 68, 082002
- Akerib D. S., et al., 2013, *Nucl. Instrum. Methods Phys. Res.*, 704, 111
- Akerib D. S., et al., 2017, *Physical Review Letters*, 118, 21303
- Akerib D. S., et al., 2020, *Phys. Rev. D*, 101, 052002
- Alcock C., et al., 1992, in Filippenko A. V., ed., *Astronomical Society of the Pacific Conference Series Vol. 103, Robotic Telescopes in the 1990s*. pp 193–202
- Alcock C., et al., 2000, *The Astrophysical Journal*, 542, 281

- Anderhalden D., Schneider A., Macciò A. V., Diemand J., Bertone G., 2013, *J. Cosmology Astropart. Phys.*, 2013, 014
- Angle J., et al., 2008, *Phys. Rev. Lett.*, 100, 021303
- Aprile E., et al., 2017a, *The European Physical Journal C*, 77, 881
- Aprile E., et al., 2017b, *Physical Review Letters*, 119, 181301
- Aprile E., et al., 2018, *Physical Review Letters*, 121, 111302
- Aprile E., et al., 2020, *J. Cosmology Astropart. Phys.*, 2020, 031
- Arcadi G., Dutra M., Ghosh P., Lindner M., Mambrini Y., Pierre M., Profumo S., Queiroz F. S., 2018, *EPJ C*, 78, 203
- Arraki K. S., Klypin A., More S., Trujillo-Gomez S., 2014, *Monthly Notices of the Royal Astronomical Society*, 438, 1466
- Babcock H. W., 1939, *Lick Observatory Bulletin*, 498, 41
- Baer H., Choi K.-Y., Kim J. E., Roszkowski L., 2015, *Phys. Rep.*, 555, 1
- Baltz E. A., Wai L., 2004, *Phys. Rev. D*, 70, 023512
- Behnke E., et al., 2008, *Science*, 319, 933
- Behroozi P. S., Wechsler R. H., Conroy C., 2013, *The Astrophysical Journal*, 770, 57
- Bélangier G., Drieu La Rochelle G., Dumont B., Godbole R. M., Kraml S., Kulkarni S., 2013, *Physics Letters B*, 726, 773
- Benitez-Llambay A., 2015, *Py-Sphviewer: Py-Sphviewer V1.0.0*, doi:10.5281/zenodo.21703
- Benítez-Llambay A., Frenk C. S., Ludlow A. D., Navarro J. F., 2019, *Monthly Notices of the Royal Astronomical Society*, 488, 2387
- Berezinsky V., Dokuchaev V., Eroshenko Y., 2006, *Phys. Rev. D*, 73, 063504
- Bernabei R., et al., 2003, *Riv. del Nuovo Cim.*, 026, 1

- Bernabei R., et al., 2008, *European Physical Journal C*, 56, 333
- Bernabei R., et al., 2013, *European Physical Journal C*, 73, 1
- Bertone G., Hooper D., Silk J., 2005, *Phys. Rep.*, 405, 279
- Bertschinger E., 2001, *The Astrophysical Journal Supplement Series*, 137, 1
- Bertschinger E., 2006, *Phys. Rev. D*, 74, 063509
- Bienaymé O., et al., 2014, *Astronomy & Astrophysics*, 571, A92
- Billard J., Riffard Q., Mayet F., Santos D., 2013, *Physics Letters, Section B: Nuclear, Elementary Particle and High-Energy Physics*, 718, 1171
- Bland-Hawthorn J., Gerhard O., 2016, *ARA&A*, 54, 529
- Blumenthal G. R., Faber S. M., Flores R., Primack J. R., 1986, *The Astrophysical Journal*, 301, 27
- Bode P., Ostriker J. P., Turok N., 2001, *The Astrophysical Journal*, 556, 93
- Bond J. R., Kofman L., Pogosyan D., 1996, *Nature*, 380, 603
- Borgani S., Masiero A., Yamaguchi M., 1996, *Physics Letters B*, 386, 189
- Bose S., et al., 2017, *Monthly Notices of the Royal Astronomical Society*, 464, 4520
- Bovy J., Rix H. W., 2013, *The Astrophysical Journal*, 779, 115
- Bovy J., Tremaine S., 2012, *The Astrophysical Journal*, 756, 89
- Boylan-Kolchin M., Bullock J. S., Kaplinghat M., 2011, *Monthly Notices of the Royal Astronomical Society*, 415, L40
- Boylan-Kolchin M., Bullock J. S., Kaplinghat M., 2012, *Monthly Notices of the Royal Astronomical Society*, 422, 1203
- Bozek B., Boylan-Kolchin M., Horiuchi S., Garrison-Kimmel S., Abazajian K., Bullock J. S., 2016, *Monthly Notices of the Royal Astronomical Society*, 459, 1489

- Bozorgnia N., Bertone G., 2017, *International Journal of Modern Physics A*, 32, 1730016
- Bozorgnia N., et al., 2016, *J. Cosmology Astropart. Phys.*, 2016, 24
- Bozorgnia N., Fattahi A., Frenk C. S., Cheek A., Cerdeño D. G., Gómez F. A., Grand R. J. J., Marinacci F., 2020, *J. Cosmology Astropart. Phys.*, 2020, 036
- Bringmann T., 2009, *New Journal of Physics*, 11, 105027
- Bringmann T., Edsjö J., Gondolo P., Ullio P., Bergström L., 2018, *J. Cosmology Astropart. Phys.*, 2018, 033
- Brook C. B., Di Cintio A., 2015, *Monthly Notices of the Royal Astronomical Society*, 450, 3920
- Brooks A. M., Zolotov A., 2014, *The Astrophysical Journal*, 786, 87
- Bruch T., Read J., Baudis L., Lake G., 2009, *The Astrophysical Journal*, 696, 920
- Buck T., Obreja A., Macciò A. V., Minchev I., Dutton A. A., Ostriker J. P., 2020, *Monthly Notices of the Royal Astronomical Society*, 491, 3461
- Bullock J. S., Boylan-Kolchin M., 2017, *ARA&A*, 55, 343
- Bullock J. S., Kolatt T. S., Sigad Y., Somerville R. S., Kravtsov A. V., Klypin A. A., Primack J. R., Dekel A., 2001, *Monthly Notices of the Royal Astronomical Society*, 321, 559
- CDMS Collaboration et al., 2013, *Physical Review Letters*, 111, 251301
- CRESST collaboration et al., 2017, arXiv e-prints, p. arXiv:1711.07692
- CTA Consortium Ong R. A., 2019, in *European Physical Journal Web of Conferences*. p. 01038 (arXiv:1904.12196), doi:10.1051/epjconf/201920901038
- Calcáneo-Roldán C., Moore B., 2000, *Phys. Rev. D*, 62, 123005
- Callingham T. M., et al., 2019, *Monthly Notices of the Royal Astronomical Society*, 484, 5453

- Calore F., et al., 2015, *J. Cosmology Astropart. Phys.*, 2015, 053
- Charbonnier A., et al., 2011, *Monthly Notices of the Royal Astronomical Society*, 418, 1526
- Charles E., et al., 2016, *Phys. Rep.*, 636, 1
- Chun E. J., Kim H. B., Kim J. E., 1994, *Phys. Rev. Lett.*, 72, 1956
- Clowe D., Bradač M., Gonzalez A. H., Markevitch M., Randall S. W., Jones C., Zaritsky D., 2006, *ApJ*, 648, L109
- Cole S., et al., 2005, *Monthly Notices of the Royal Astronomical Society*, 362, 505
- Colín P., Avila-Reese V., Valenzuela O., 2000, *The Astrophysical Journal*, 542, 622
- Colín P., Avila-Reese V., Valenzuela O., Firmani C., 2002, *The Astrophysical Journal*, 581, 777
- Crain R. A., et al., 2015, *Monthly Notices of the Royal Astronomical Society*, 450, 1937
- Cui M.-Y., Yuan Q., Tsai Y.-L. S., Fan Y.-Z., 2017, *Phys. Rev. Lett.*, 118, 191101
- D’Onghia E., Springel V., Hernquist L., Keres D., 2010, *The Astrophysical Journal*, 709, 1138
- Davé R., Spergel D. N., Steinhardt P. J., Wandelt B. D., 2001, *The Astrophysical Journal*, 547, 574
- De Bernardis P., et al., 2000, *Nature*, 404, 955
- De Sainte Agathe V., et al., 2019, *Astronomy & Astrophysics*, 629, A85
- Deason A. J., et al., 2011, *Monthly Notices of the Royal Astronomical Society*, 415, 2607
- Deason A. J., et al., 2012, *Monthly Notices of the Royal Astronomical Society*, 425, 2840

- Deason A. J., Fattahi A., Belokurov V., Evans N. W., Grand R. J. J., Marinacci F., Pakmor R., 2019, *Monthly Notices of the Royal Astronomical Society*, 485, 3514
- Debattista V. P., Moore B., Quinn T., Kazantzidis S., Maas R., Mayer L., Read J., Stadel J., 2007, *The Astrophysical Journal*, 681, 1076
- Di Cintio A., Brook C. B., Macciò A. V., Stinson G. S., Knebe A., Dutton A. A., Wadsley J., 2014, *Monthly Notices of the Royal Astronomical Society*, 437, 415
- Diemand J., Kuhlen M., Madau P., 2006, *The Astrophysical Journal*, 649, 1
- Diemand J., Kuhlen M., Madau P., 2007, *The Astrophysical Journal*, 657, 262
- Diemer B., Joyce M., 2019, *The Astrophysical Journal*, 871, 168
- Diemer B., Kravtsov A. V., 2014, *The Astrophysical Journal*, 789, 1
- Dodelson S., Hooper D., Serpico P. D., 2008, *Phys. Rev. D*, 77, 063512
- Dolag K., Borgani S., Murante G., Springel V., 2009, *Monthly Notices of the Royal Astronomical Society*, 399, 497
- Drlica-Wagner A., et al., 2015, *The Astrophysical Journal*, 813, 109
- Drukier A. K., Freese K., Spergel D. N., 1986a, *Phys. Rev. D*, 33, 3495
- Drukier A. K., Freese K., Spergel D. N., 1986b, *Phys. Rev. D*, 33, 3495
- Du N., et al., 2018, *Phys. Rev. Lett.*, 120, 151301
- Dubinski J., 2002, *The Astrophysical Journal*, 431, 617
- Duffy A. R., Schaye J., Kay S. T., Dalla Vecchia C., Battye R. A., Booth C. M., 2010, *Monthly Notices of the Royal Astronomical Society*, 405, 2161
- Dutton A. A., Macciò A. V., Frings J., Wang L., Stinson G. S., Penzo C., Kang X., 2016, *Monthly Notices of the Royal Astronomical Society*, 457, L74
- Einasto J., 1965, *Trudy Astrofizicheskogo Instituta Alma-Ata*, 5, 87
- Eisenstein D. J., et al., 2005, *The Astrophysical Journal*, 633, 560

- Elbert O. D., Bullock J. S., Garrison-Kimmel S., Rocha M., Oñorbe J., Peter A. H. G., 2015, *Monthly Notices of the Royal Astronomical Society*, 453, 29
- Ellis J., Hagelin J. S., Nanopoulos D. V., Olive K., Srednicki M., 1984, *Nuclear Physics B*, 238, 453
- Engel J., 1991, *Physics Letters B*, 264, 114
- Evans N. W., Ferrer F., Sarkar S., 2004, *Phys. Rev. D*, 69, 123501
- Evans N. W., O'Hare C. A. J., McCabe C., 2019, *Phys. Rev. D*, 99, 023012
- Falk T., Olive K. A., Srednicki M., 1994, *Physics Letters B*, 339, 248
- Feng J. L., 2010, *ARA&A*, 48, 495
- Ferrière K., 2012, *Astronomy & Astrophysics*, 540, A50
- Font A. S., et al., 2020, *Monthly Notices of the Royal Astronomical Society*, 498, 1765
- Font A. S., McCarthy I. G., Belokurov V., 2021, *Monthly Notices of the Royal Astronomical Society*, 505, 783
- Freese K., Frieman J., Gould A., 1988, *Phys. Rev. D*, 37, 3388
- Freese K., Gondolo P., Newberg H. J., 2005, *Phys. Rev. D*, 71, 43516
- GLAST Facility Science Team Gehrels N., Michelson P., 1999, *Astroparticle Physics*, 11, 277
- Gaia Collaboration et al., 2016, *Astronomy & Astrophysics*, 595, A2
- Gaia Collaboration et al., 2018, *Astronomy & Astrophysics*, 616, A1
- Garbari S., Read J. I., Lake G., 2011, *Monthly Notices of the Royal Astronomical Society*, 416, 2318
- Garbari S., Liu C., Read J. I., Lake G., 2012, *Monthly Notices of the Royal Astronomical Society*, 425, 1445

- Garrison-Kimmel S., Horiuchi S., Abazajian K. N., Bullock J. S., Kaplinghat M., 2014, *Monthly Notices of the Royal Astronomical Society*, 444, 961
- Garrison-Kimmel S., et al., 2017, *Monthly Notices of the Royal Astronomical Society*, 471, 1709
- Garrison-Kimmel S., et al., 2018, *Monthly Notices of the Royal Astronomical Society*, 481, 4133
- Geringer-Sameth A., Koushiappas S. M., 2011, *Phys. Rev. Lett.*, 107, 241303
- Gilmore G., 1997, *The Astrophysical Journal*, 100, 161
- Gilmore G., Wilkinson M. I., Wyse R. F. G., Kleyna J. T., Koch A., Evans N. W., Grebel E. K., 2007, *The Astrophysical Journal*, 663, 948
- Gnedin O. Y., Kravtsov A. V., Klypin A. A., Nagai D., 2004, *The Astrophysical Journal*, 616, 16
- Goldberg H., 1983, *Phys. Rev. Lett.*, 50, 1419
- Gondolo P., Edsjö J., Ullio P., Bergström L., Schelke M., Baltz E. A., 2004, *J. Cosmology Astropart. Phys.*, 2004, 008
- Goodman M. W., Witten E., 1985, *Phys. Rev. D*, 31, 3059
- Górski K. M., Hivon E., Banday A. J., Wandelt B. D., Hansen F. K., Reinecke M., Bartelmann M., 2005, *The Astrophysical Journal*, 622, 759
- Grand R., 2016, in *Discs in galaxies (Discs 2016)*. p. 34, doi:10.5281/zenodo.61555
- Grand R. J. J., et al., 2017, *Monthly Notices of the Royal Astronomical Society*, 467, 179
- Green A. M., 2001, *Phys. Rev. D*, 63, 6
- Green A. M., 2017, *Journal of Physics G: Nuclear and Particle Physics*, 44, 84001
- Green A. M., Hofmann S., Schwarz D. J., 2004, *Monthly Notices of the Royal Astronomical Society*, 353, L23

- Gunn J. E., Katz N., 1991, *The Astrophysical Journal*
- Guo Q., White S., Li C., Boylan-Kolchin M., 2010, *Monthly Notices of the Royal Astronomical Society*, 404, 1111
- Hagen J. H. J., Helmi A., 2018, *Astronomy & Astrophysics*, 615, A99
- Hahn O., Abel T., 2011, *Monthly Notices of the Royal Astronomical Society*, 415, 2101
- Hall L. J., Moroi T., Murayama H., 1998, *Physics Letters B*, 424, 305
- Hanany S., et al., 2000, *ApJ*, 545, L5
- Helmi A., Babusiaux C., Koppelman H. H., Massari D., Veljanoski J., Brown A. G. A., 2018, *Nature*, 563, 85
- Hinshaw G., et al., 2013, *The Astrophysical Journal Supplement Series*, 208, 19
- Hinton J. A., HESS Collaboration 2004, *New Astron. Rev.*, 48, 331
- Holmberg E., 1941, *The Astrophysical Journal*, 94, 385
- Holmberg J., Flynn C., 2004, *Monthly Notices of the Royal Astronomical Society*, 352, 440
- Horiuchi S., Bozek B., Abazajian K. N., Boylan-Kolchin M., Bullock J. S., Garrison-Kimmel S., Onorbe J., 2016, *Monthly Notices of the Royal Astronomical Society*, 456, 4346
- Iocco F., Pato M., Bertone G., 2015, *Nature Physics*, 11, 245
- Jungman G., Kamionkowski M., Griest K., 1996, *Phys. Rep.*, 267, 195
- Kaplinghat M., Tulin S., Yu H.-B., 2016, *Phys. Rev. Lett.*, 116, 041302
- Kauffmann G., White S. D. M., Guiderdoni B., 1993, *Monthly Notices of the Royal Astronomical Society*, 264, 201
- Kazantzidis S., Kravtsov A. V., Zentner A. R., Allgood B., Nagai D., Moore B., 2004, *The Astrophysical Journal*

- Kazantzidis S., Abadi M. G., Navarro J. F., 2010, *ApJ*
- Kelso C., Savage C., Valluri M., Freese K., Stinson G. S., Bailin J., 2016, *J. Cosmology Astropart. Phys.*, 2016, 71
- Klypin A., Kravtsov A. V., Valenzuela O., Prada F., 1999, *The Astrophysical Journal*, 522, 82
- Kuhlen M., Diemand J., Madau P., 2008, *The Astrophysical Journal*, 686, 262
- Kuhlen M., Weiner N., Diemand J., Madau P., Moore B., Potter D., Stadel J., Zemp M., 2010, *J. Cosmology Astropart. Phys.*, 2010, 30
- Kuzio de Naray R., McGaugh S. S., de Blok W. J. G., 2008, *The Astrophysical Journal*, 676, 920
- Lewin J. D., Smith P. F., 1996, *Astroparticle Physics*, 6, 87
- Lewis A., Challinor A., Lasenby A., 2000, *The Astrophysical Journal*, 538, 473
- Ling F. S., Nezri E., Athanassoula E., Teyssier R., 2010, *J. Cosmology Astropart. Phys.*, 2010, 12
- Lisanti M., Strigari L. E., Wacker J. G., Wechsler R. H., 2011, *Phys. Rev. D*, 83, 023519
- Loeb A., Zaldarriaga M., 2005, *Phys. Rev. D*, 71, 103520
- Lorenz E., MAGIC Collaboration 2004, *New Astron. Rev.*, 48, 339
- Lovell M. R., et al., 2012, *Monthly Notices of the Royal Astronomical Society*, 420, 2318
- Lovell M. R., Gonzalez-Perez V., Bose S., Boyarsky A., Cole S., Frenk C. S., Ruchayskiy O., 2017, *Monthly Notices of the Royal Astronomical Society*, 468, 2836
- Ludlow A. D., Bose S., Angulo R. E., Wang L., Hellwing W. A., Navarro J. F., Cole S., Frenk C. S., 2016, *Monthly Notices of the Royal Astronomical Society*, 460, 1214
- Macciò A. V., Paduroiu S., Anderhalden D., Schneider A., Moore B., 2012, *Monthly Notices of the Royal Astronomical Society*, 424, 1105

- Madau P., Diemand J., Kuhlen M., 2008, *The Astrophysical Journal*, 679, 1260
- Madau P., Shen S., Governato F., 2014, *ApJ*, 789, L17
- Maier G., 2019, in 36th International Cosmic Ray Conference (ICRC2019). p. 733
(arXiv:1907.08171)
- Mao Y. Y., Strigari L. E., Wechsler R. H., Wu H. Y., Hahn O., 2013, *The Astrophysical Journal*, 764, 35
- Marsh D. J. E., 2016, *Phys. Rep.*, 643, 1
- Mashchenko S., Wadsley J., Couchman H. M. P., 2008, *Science*, 319, 174
- Mazziotta M. N., Loparco F., de Palma F., Giglietto N., 2012, *Astroparticle Physics*, 37, 26
- McCarthy I. G., Font A. S., 2020, *Monthly Notices of the Royal Astronomical Society*, 499, 3255
- McCarthy I. G., Schaye J., Bird S., Le Brun A. M. C., 2017, *Monthly Notices of the Royal Astronomical Society*, 465, 2936
- McDermott S. D., Yu H.-B., Zurek K. M., 2011, *Phys. Rev. D*, 83, 063509
- McGaugh S. S., Rubin V. C., de Blok W. J. G., 2001, *AJ*, 122, 2381
- McMillan P. J., 2017, *Monthly Notices of the Royal Astronomical Society*, 465, 76
- Monari G., et al., 2018, *Astronomy & Astrophysics*, 616, L9
- Moni Bidin C., Carraro G., Méndez R. A., Smith R., 2012, *The Astrophysical Journal*, 751, 30
- Moore B., Ghigna S., Governato F., Lake G., Quinn T., Stadel J., Tozzi P., 1999, *ApJ*, 524, L19
- Myeong G. C., Evans N. W., Belokurov V., Amorisco N. C., Koposov S. E., 2018, *Monthly Notices of the Royal Astronomical Society*, 475, 1537
- Navarro J. F., Frenk C. S., White S. D. M., 1996, *The Astrophysical Journal*, 462, 563

- Navarro J. F., Frenk C. S., White S. D. M., 1997, *The Astrophysical Journal*, 490, 493
- Necib L., et al., 2020a, *Nature Astronomy*, 4, 1078
- Necib L., Ostdiek B., Lisanti M., Cohen T., Freytsis M., Garrison-Kimmel S., 2020b, *The Astrophysical Journal*, 903, 25
- Nihei T., Roszkowski L., Ruiz de Austri R., 2001, *Journal of High Energy Physics*, 2001, 063
- Oñorbe J., Boylan-Kolchin M., Bullock J. S., Hopkins P. F., Kereš D., Faucher-Giguère C.-A., Quataert E., Murray N., 2015, *Monthly Notices of the Royal Astronomical Society*, 454, 2092
- O'Hare C. A., McCabe C., Evans N. W., Myeong G., Belokurov V., 2018, *Phys. Rev. D*, 98
- O'Hare C. A. J., Evans N. W., McCabe C., Myeong G., Belokurov V., 2020, *Phys. Rev. D*, 101, 023006
- Padmanabhan N., et al., 2007, *Monthly Notices of the Royal Astronomical Society*, 378, 852
- Pato M., Iocco F., 2015, *ApJ*, 803, L3
- Pato M., Agertz O., Bertone G., Moore B., Teyssier R., 2010, *Phys. Rev. D*, 82, 023531
- Patrignani C., et al., 2016, *Chinese Physics C*, 40, 100001
- Peebles P. J. E., Yu J. T., 1970, *The Astrophysical Journal*, 162, 815
- Penzias A. A., Wilson R. W., 1965, *The Astrophysical Journal*, 142, 419
- Percival W. J., Cole S., Eisenstein D. J., Nichol R. C., Peacock J. A., Pope A. C., Szalay A. S., 2007, *Monthly Notices of the Royal Astronomical Society*, 381, 1053
- Perlmutter S., et al., 2002, *The Astrophysical Journal*, 517, 565
- Persic M., Salucci P., Stel F., 1996, *Monthly Notices of the Royal Astronomical Society*, 281, 27

- Piffi T., et al., 2013, *Astronomy & Astrophysics*, 562, A91
- Piffi T., et al., 2014, *Monthly Notices of the Royal Astronomical Society*, 445, 3133
- Pillepich A., et al., 2018, *Monthly Notices of the Royal Astronomical Society*, 475, 648
- Planck Collaboration et al., 2020, *Astronomy & Astrophysics*, 641, A6
- Polisensky E., Ricotti M., 2011, *Phys. Rev. D*, 83, 043506
- Pontzen A., Governato F., 2012, *Monthly Notices of the Royal Astronomical Society*, 421, 3464
- Poole-McKenzie R., Font A. S., Boxer B., McCarthy I. G., Burdin S., Stafford S. G., Brown S. T., 2020, *J. Cosmology Astropart. Phys.*, 2020, 016
- Posti L., Helmi A., 2019, *Astronomy & Astrophysics*, 621, A56
- Power C., Navarro J. F., Jenkins A., Frenk C. S., White S. D. M., Springel V., Stadel J., Quinn T., 2003, *Monthly Notices of the Royal Astronomical Society*, 338, 14
- Press W. H., Schechter P., 1974, *The Astrophysical Journal*, 187, 425
- Profumo S., Sigurdson K., Kamionkowski M., 2006, *Phys. Rev. Lett.*, 97, 031301
- Purcell C. W., Bullock J. S., Kaplinghat M., 2009, *The Astrophysical Journal*, 703, 2275
- Purcell C. W., Zentner A. R., Wang M. Y., 2012, *J. Cosmology Astropart. Phys.*, 2012, 27
- Read J. I., 2014, *Journal of Physics G Nuclear Physics*, 41
- Read J. I., Lake G., Agertz O., Debattista V. P., 2008, *Monthly Notices of the Royal Astronomical Society*, 389, 1041
- Read J. I., Mayer L., Brooks A. M., Governato F., Lake G., 2009, *Monthly Notices of the Royal Astronomical Society*, 397, 44
- Read J. I., Agertz O., Collins M. L. M., 2016, *Monthly Notices of the Royal Astronomical Society*, 459, 2573

- Regis M., Ullio P., 2008, *Phys. Rev. D*, 78, 043505
- Riess A. G., et al., 1998, *The Astrophysical Journal*, 116, 1009
- Roberts M. S., Whitehurst R. N., 1975, *The Astrophysical Journal*, 201, 327
- Rocha M., Peter A. H. G., Bullock J. S., Kaplinghat M., Garrison-Kimmel S., Oñorbe J., Moustakas L. A., 2013, *Monthly Notices of the Royal Astronomical Society*, 430, 81
- Rosenberg L. J., van Bibber K. A., 2000, *Phys. Rep.*, 325, 1
- Ross A. J., Samushia L., Howlett C., Percival W. J., Burden A., Manera M., 2015, *Monthly Notices of the Royal Astronomical Society*, 449, 835
- Roszkowski L., 2004, *Pramana*, 62, 389
- Roszkowski L., Sessolo E. M., Trojanowski S., 2018, *Reports on Progress in Physics*, 81, 066201
- Rubin V. C., Ford W. Kent J., 1970, *The Astrophysical Journal*, 159, 379
- Rubin V. C., Ford W. K. J., Thonnard N., 1980, *The Astrophysical Journal*, 238, 471
- Ryden B. S., Gunn J. E., 1987, *The Astrophysical Journal*, 318, 15
- Sánchez-Salcedo F. J., Martínez-Gómez E., Magaña J., 2010, *J. Cosmology Astropart. Phys.*, 2010, 031
- Sawala T., et al., 2014, arXiv e-prints, p. arXiv:1412.2748
- Sawala T., et al., 2016, *Monthly Notices of the Royal Astronomical Society*, 457, 1931
- Schaller M., et al., 2015, *Monthly Notices of the Royal Astronomical Society*, 451, 1247
- Schaller M., et al., 2016a, *Monthly Notices of the Royal Astronomical Society*, 455, 4442
- Schaller M., Frenk C. S., Fattahi A., Navarro J. F., Oman K. A., Sawala T., 2016b, *Monthly Notices of the Royal Astronomical Society*, 461, L56

- Schaye J., et al., 2015, *Monthly Notices of the Royal Astronomical Society*, 446, 521
- Schödel R., Merritt D., Eckart A., 2009, *Astronomy & Astrophysics*, 502, 91
- Shao S., Gao L., Theuns T., Frenk C. S., 2013, *Monthly Notices of the Royal Astronomical Society*, 430, 2346
- Sikivie P., 1983, *Phys. Rev. Lett.*, 51, 1415
- Silverwood H., Weniger C., Scott P., Bertone G., 2015, *J. Cosmology Astropart. Phys.*, 2015, 055
- Sivertsson S., Silverwood H., Read J. I., Bertone G., Steger P., 2018, *Monthly Notices of the Royal Astronomical Society*, 478, 1677
- Sloane J. D., Buckley M. R., Brooks A. M., Governato F., 2016, *The Astrophysical Journal*, 831, 93
- Smith M. C., Whiteoak S. H., Evans N. W., 2012, *The Astrophysical Journal*, 746, 181
- Smoot G. F., et al., 1992, *ApJ*, 396, L1
- Soubiran C., Bienaymé O., Mishenina T. V., Kovtyukh V. V., 2008, *Astronomy & Astrophysics*, 480, 91
- Spergel D. N., Steinhardt P. J., 2000, *Phys. Rev. Lett.*, 84, 3760
- Springel V., 2005, *Monthly Notices of the Royal Astronomical Society*, 364, 1105
- Springel V., et al., 2005, *Nature*, 435, 629
- Springel V., et al., 2008, *Monthly Notices of the Royal Astronomical Society*, 391, 1685
- Stafford S. G., Brown S. T., McCarthy I. G., Font A. S., Robertson A., Poole-Mckenzie R., 2020, arXiv e-prints, p. arXiv:2004.03872
- Steigman G., Turner M. S., 1985, *Nuclear Physics, Section B*, 253, 375
- Steigman G., Dasgupta B., Beacom J. F., 2012, *Phys. Rev. D*, 86, 23506
- Stiff D., Widrow L. M., 2003, *Physical Review Letters*, 90, 4

- Stinson G. S., Brook C., Macciò A. V., Wadsley J., Quinn T. R., Couchman H. M. P., 2013, *Monthly Notices of the Royal Astronomical Society*, 428, 129
- Stoehr F., White S. D. M., Springel V., Tormen G., Yoshida N., 2003, *Monthly Notices of the Royal Astronomical Society*, 345, 1313
- Strigari L. E., 2013, *Phys. Rep.*, 531, 1
- Strigari L. E., Koushiappas S. M., Bullock J. S., Kaplinghat M., 2007, *Phys. Rev. D*, 75, 083526
- Sunyaev R. A., Zeldovich Y. B., 1970, *Ap&SS*, 7, 20
- TEXONO Collaboration: S. T. Lin 2007, arXiv e-prints, p. arXiv:0712.1645
- The DarkSide Collaboration et al., 2018, arXiv e-prints, p. arXiv:1802.06994
- Tinker J., Kravtsov A. V., Klypin A., Abazajian K., Warren M., Yepes G., Gottlöber S., Holz D. E., 2008, *The Astrophysical Journal*, 688, 709
- Tissera P. B., White S. D. M., Pedrosa S., Scannapieco C., 2010, *Monthly Notices of the Royal Astronomical Society*
- Tisserand P., et al., 2007, *Astronomy & Astrophysics*, 469, 387
- Tomozeiu M., Mayer L., Quinn T., 2016, *ApJ*, 827, L15
- Torrey P., Vogelsberger M., Genel S., Sijacki D., Springel V., Hernquist L., 2014, *Monthly Notices of the Royal Astronomical Society*, 438, 1985
- Tsallis C., 1988, *Journal of Statistical Physics*, 52, 479
- Van de Weygaert R., Bond J. R., 2008, *Clusters and the Theory of the Cosmic Web*. In: Plionis M., Hughes D., López-Cruz O.. Springer, Dordrecht, p. 335, doi:10.1007/978-1-4020-6941-3_10
- Vasiliev E., 2019, *Monthly Notices of the Royal Astronomical Society*, 484, 2832
- Villaescusa-Navarro F., Dalal N., 2011, *J. Cosmology Astropart. Phys.*, 2011, 024

- Vogelsberger M., et al., 2009, *Monthly Notices of the Royal Astronomical Society*, 395, 797
- Vogelsberger M., Zavala J., Loeb A., 2012, *Monthly Notices of the Royal Astronomical Society*, 423, 3740
- Vogelsberger M., Genel S., Sijacki D., Torrey P., Springel V., Hernquist L., 2013, *Monthly Notices of the Royal Astronomical Society*, 436, 3031
- Von Hoerner S., 1960, *Z. Astrophys.*, 50, 184
- Von Hoerner S., 1963, *Z. Astrophys.*, 57, 47
- Walker M. G., Mateo M., Olszewski E. W., Peñarrubia J., Evans N. W., Gilmore G., 2009, *The Astrophysical Journal*, 704, 1274
- Wang Q. D., Gotthelf E. V., Lang C. C., 2002, *Nature*, 415, 148
- Watkins L. L., van der Marel R. P., Sohn S. T., Evans N. W., 2019, *The Astrophysical Journal*, 873, 118
- Weekes T. C., et al., 2002, *Astroparticle Physics*, 17, 221
- Wegg C., Gerhard O., Bieth M., 2019, *Monthly Notices of the Royal Astronomical Society*, 485, 3296
- Weinberg D. H., Mortonson M. J., Eisenstein D. J., Hirata C., Riess A. G., Rozo E., 2013, *Phys. Rep.*, 530, 87
- Wetzell A. R., Hopkins P. F., Kim J.-h., Faucher-Giguère C.-A., Kereš D., Quataert E., 2016, *ApJ*, 827, L23
- Wharton R. S., Chatterjee S., Cordes J. M., Deneva J. S., Lazio T. J. W., 2012, *The Astrophysical Journal*, 753, 108
- Yoshida N., Springel V., White S. D. M., Tormen G., 2000, *ApJ*, 544, L87
- Yusef-Zadeh F., Goss W. M., Roberts D. A., Robinson B., Frail D. A., 1999, *The Astrophysical Journal*, 527, 172

-
- Zavala J., Vogelsberger M., Walker M. G., 2013, *Monthly Notices of the Royal Astronomical Society*, 431, L20
- Zhang L., Rix H. W., Van De Ven G., Bovy J., Liu C., Zhao G., 2013, *The Astrophysical Journal*, 772, 108
- Zhou X., et al., 2020, arXiv e-prints, p. arXiv:2008.06485
- Zolotov A., et al., 2012, *The Astrophysical Journal*, 761, 71
- Zonca A., Singer L., Lenz D., Reinecke M., Rosset C., Hivon E., Gorski K., 2019, *Journal of Open Source Software*, 4, 1298
- Zwicky F., 1933, *Helvetica Physica Acta*, 6, 110